Calibration of Phase I of the
GERDA Double Beta Decay Experiment

Dissertation

zur
Erlangung der naturwissenschaftlichen Doktorwürde
(Dr. sc. nat.)

vorgelegt der
Mathematisch-naturwissenschaftlichen Fakultät
der
Universität Zürich

von
Francis Froborg
aus
Deutschland

Promotionskomitee

Prof. Dr. Laura Baudis (Vorsitz)
Dr. Alfredo Davide Ferella
Dr. Marc Schumann

Zürich 2012

Abstract

The GERmanium Detector Array, GERDA, is looking for the neutrinoless double beta decay in ^{76}Ge. It uses high purity germanium detectors submerged nakedly in liquid argon, which acts simultaneously as cooling liquid and shielding material. Further shielding and background reduction is reached by a water Cherenkov veto surrounding the cryostat and the underground location chosen for the experiment, the Laboratori Nazionali del Gran Sasso. The experiment is planned in two phases. The first one started in November 2011 and uses reprocessed detectors from the Heidelberg-Moscow and IGEX experiment. For the second phase, newly developed broad-energy germanium detectors enriched in ^{76}Ge will be added to the current detectors.

In this thesis, the calibration system for the commissioning phase as well as GERDA's phase I was developed. Monte Carlo Simulations were used to determine the relevant parameters of calibration system, such as type and activity of the used sources, the required number of sources as well as their optimum position. To determine the background contribution from the calibration sources, gamma as well as neutron induced background was considered. The required shielding for the gamma radiation was determined. The hardware for the lowering system to move the calibration sources over several meters from their parking position on top of the cryostat down to the detectors was designed, built, tested and installed at the experiment. The energy resolution of the detectors measured during calibration runs was significantly higher than expected from previous measurements outside GERDA. Thus, an optimization of the offline data analysis was performed.

Zusammenfassung

Das GERDA Experiment sucht nach dem neutrinolosen Doppel-Beta Zerfall in ^{76}Ge. Die verwendeten Germanium-Detektoren werden hierbei nackt in flüssigem Argon betrieben, das gleichzeitig als Kühlmittel wie auch als Abschirmung fungiert. Die Untergrundstrahlung wird durch ein Wasser-Cerenkov-Veto weiter reduziert, das den Kryostaten umgibt. Darüber hinaus befindet sich das Experiment im Laboratori Nazionali del Gran Sasso 1400 m unter der Erde. GERDA ist in zwei Phasen geplant. Phase I startete im November 2011 und verwendet aufbereitete Detektoren der HdM und IGEX Experimente. In Phase II werden neu entwickelte Punkt-Kontakt Germanium Detektoren (BEGe's) hinzugefügt.

Diese Dissertation beschreibt die Entwicklung eines Kalibrierungssystems für GERDAs Installationsphase sowie Phase I. Mithilfe von Monte-Carlo Simulationen wurden sämtliche relevanten Parameter des Systems bestimmt und verifiziert. Dazu gehören der Typ und die Aktivität der verwendeten, radioaktiven Quellen, die nötige Anzahl sowie ihre optimale Positionierung. Darüber hinaus wurde der Untergrund bestimmt, der durch die Strahlung der Kalibrierungsquellen in den Detektoren verursacht wird. Hierbei wurde sowohl die Gamma-Strahlung als auch durch Neutronen verursachter Untergrund berücksichtigt. Die während der Kalibrierungen gemessene Energieauflösung der Detektoren war deutlich höher, als die bei früheren Testmessungen bestimmte. Aus diesem Grund wurde eine Optimierung der digitalen Datenanalyse durchgeführt.

Für eine große kleine Frau.

Acknowledgments

Contents

Introduction 1

Although the neutrino was discovered over 50 years, our knowledge is still very limited. It is the only Standard Model fermion without an electric charge, thus might be its own antiparticle, a Majorana particle. This special property gives also the most general explanation for the neutrino masses, which were discovered about 15 years ago by oscillation experiments and proof physics beyond the Standard Model. The Majorana nature of neutrinos might also explain the baryon asymmetry of the Universe, the basis of our own existence.

The only currently known way to experimentally proof the Majorana nature of neutrinos is the neutrinoless double beta decay. Double beta decay is a very rare process, where two neutrons of a nuclei decay simultaneously into two protons, two electrons and two neutrinos. About a dozen isotopes are known to decay in this way, with both neutrinos escaping. In case the neutrino is its own antiparticle, it is possible that the two neutrinos are exchanged as virtual particles in this process, with just the two protons and two electrons as end products. Several experiments using different isotopes and techniques tried to find the neutrinoless double beta decay. So far, just a subgroup of the Heidelberg-Moscow experiment claimed a discovery, using high-purity germanium detectors enriched in the double beta decaying istope ^{76}Ge. So far, this result could not be verified. Details about the theory of neutrinos, double beta decay as well as relevant experiments can be found in chapter 2.

The GERmanium Detector Array, GERDA, will probe the results of the Heidelberg-Moscow experiment. It uses as well high-purity germanium detectors enriched in ^{76}Ge and is located at the Laboratori Nazionali del Gran Sasso (LNGS). To reach a higher experimental sensitivity, a larger ^{76}Ge mass is used and the background reduced. The latter is reached by submerging the detectors nakedly into the needed cryogenic liquid. This reduces the amount of material close to the detectors and thus possible natural radioactivity. The used cryo liquid is argon which also acts as shielding material. The argon cryostat is surrounded by a water tank equipped with photomultipliers, which further shields the detectors and can be used to identify background radiation.

The experiment is planned in two phases. The first one, which started in November 2011, uses reprocessed detectors from the Heidelberg-Moscow and the IGEX experiment enriched in ^{76}Ge together with natural germanium detectors from the Genius Test Facility. The Heidelberg-Moscow claim can be tested in about a year of data taking. Afterwards, the experiment will be upgraded for phase II, where newly developed broad-energy germanium detectors enriched in ^{76}Ge will be added to the current detectors. Details about the used detectors and their detection technique can be found in chapter 3; GERDA is described in chapter 4.

The aim of this work was the development of the calibration system for the commissioning as well as the first phase of the experiment. Radioactive sources will be used for an energy as well as a pulse shape calibration with a calibration run once a week. During physics runs, the sources are parked at the top of the cryostat.

In the first step, Monte Carlo Simulations were used to determine the relevant parameters of the calibration system, such as type and activity of the used sources, the required number of sources as well as their optimum position. Since the experiment aims for the lowest possible background in the region of interest, the contribution from the calibration sources is important to determine together with the necessary shielding. This is described in chapter 5.

In the next step, the hardware necessary to lower the calibration sources from their parking position over several meters down to the detector had to be designed, built, tested and installed at the experiment. This process is described in chapter 6.

The energy resolution of the detectors measured during calibration runs was significantly worse than expected from previous measurements outside GERDA. Thus an optimization of the offline data analysis was required. The necessary theory as well as the performed analysis is described together with the results in chapter 7.

The thesis concludes with a summary in chapter 8. In the appendix, technical drawings (appendix A) as well as specifications (appendix B) of the hardware of the calibration system can be found.

Neutrino Physics 2

The neutrino is one of the fundamental particles included in the Standard Model of particle physics. It is by far the lightest of the fermions and carrying no electric charge or color, it nearly exclusively interacts via the weak interaction. This feature makes their detection extremely difficult and explains our limited knowledge about them.

Neutrinos play a crucial role in our understanding of the fundamental laws of physics, structure formation in the Universe, cosmic ray physics as well as supernova dynamics and might help to explain the baryon asymmetry in the universe. The following chapter gives an overview of our current knowledge and explains with the neutrinoless double beta decay one of the most promising experimental methods to answer open fundamental questions. The interested reader is referred to [1, 2, 3, 4, 5] where most of the material is taken from.

2.1 Standard Model Neutrinos

The neutrino was postulated in 1930 by Wolfgang Pauli to explain the missing energy in the β-decay [6] and was first detected by Cowan and Reines in 1956 in a reactor experiment [7]. The width of the Z resonances shows that there are three neutrino flavors active in the weak interaction [8], while the Goldhaber experiment reveals that there are just left-handed neutrinos [9]. The latter is the reason why neutrinos are introduced as massless particle in the Standard Model: Mass is necessary for the helicity flip converting a left-handed into a right-handed neutrino. The Standard Model then introduces electroweak doublets combining the charged (massive) leptons with the corresponding neutrino flavor eigenstates. The right-handed charged leptons form electroweak singlets due to the absence of right-handed neutrinos:

$$\begin{pmatrix} e \\ \nu_e \end{pmatrix}_L \quad \begin{pmatrix} \mu \\ \nu_\mu \end{pmatrix}_L \quad \begin{pmatrix} \tau \\ \nu_\tau \end{pmatrix}_L$$

$$(e)_R \quad (\mu)_R \quad (\tau)_R$$

2.2 Neutrino Oscillation

Results from solar, atmospheric and reactor neutrino experiments can be explained by an oscillation of the neutrino flavors eigenstates, which was first discussed by Pontecorvo [10, 11] and by Maki, Nakagawa and Sakata [12]. Such an oscillation implies that neutrinos have a non-zero mass. The large number of experiments using different neutrino sources and detection techniques all showing consistent results lead to the fact that neutrino oscillation is well established nowadays. The corresponding formalism, in analogy to the quark sector,
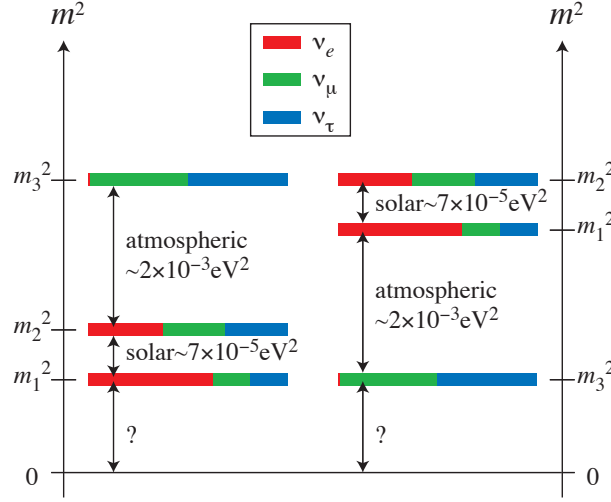
Figure 2.1: The two possible neutrino mass hierarchies. Indicated are the two mass differences between Δm_{12} known from solar data as well as Δm_{23} known from atmospheric data. Color coded the probability to find one of the three neutrino flavor eigenstates in a particular mass eigenstate. [2]

presumes that neutrino flavor eigenstates $|\nu_l\rangle = |\nu_e\rangle, |\nu_\mu\rangle, |\nu_\tau\rangle$ are coherent superpositions of mass eigenstates $|\nu_i\rangle$:

$$|\nu_l\rangle = \sum_i U_{li} |\nu_i\rangle \tag{2.1}$$

where U_{li} are the matrix elements of the unitary mixing matrix U_{PMNS} given by

$$U_{\text{PMNS}} = \begin{pmatrix} c_{13}c_{12} & c_{13}s_{12} & s_{13}e^{-i\delta} \\ -c_{23}s_{12} - s_{23}c_{12}s_{13}e^{i\delta} & c_{23}c_{12} - s_{23}s_{12}s_{13}e^{i\delta} & c_{13}s_{23} \\ s_{23}s_{12} - c_{23}c_{12}s_{13}e^{i\delta} & -s_{23}c_{12} - c_{23}s_{12}s_{13}e^{i\delta} & c_{13}c_{23} \end{pmatrix} \begin{pmatrix} e^{i\alpha_1} \\ e^{i\alpha_2} \\ 1 \end{pmatrix} \tag{2.2}$$

with $c_{ij} = \cos\theta_{ij}$ and $s_{ij} = \sin\theta_{ij}$, δ is known as the CP violating Dirac phase and α_i as the Majorana phases. The second term in equation (2.2) is just relevant in case neutrinos are Majorana particles, which means that they are their own antiparticle and total lepton number is violated. The difference compared to Standard Model Dirac particles is explained in section 2.3. The matrix elements of U give the quantum amplitude that a flavor eigenstate contains an admixture of mass eigenstates. The probability of flavor change is given by

$$P(\nu_l \to \nu_{l'}) = \left| \sum_{i=1}^{3} U_{li} \exp\left\{ -i\frac{m_i^2 L}{2E} \right\} U_{li}^\star \right|^2 \tag{2.3}$$

with L the distance between neutrino source and detector. This shows that oscillation experiments are only sensitive to mass squared differences, not the absolute mass scale. Given the current results shown below, there are two possible arrangements of the neutrino masses: The normal hierarchy with $m_1 < m_2 \ll m_3$ and the inverted hierarchy with $m_3 \ll m_1 < m_2$. A visualization can be found in figure 2.1. Furthermore, oscillation experiments cannot distinguish between the Dirac or Majorana nature of neutrinos.

The current best values for the parameters Δm_{12}^2 and $\tan^2\theta_{12}$ are coming from the analysis of the KamLAND reactor experiment as well as solar neutrino experiments, leading to [13]

$$\Delta m_{12}^2 = (7.59 \pm 0.21)\, 10^{-5} \text{ eV}^2, \qquad \tan^2\theta_{12} = 0.47^{+0.06}_{-0.05}. \tag{2.4}$$

The parameters Δm_{23}^2 and $\sin^2 2\theta_{23}$ were first measured by Super-Kamiokande [14] and the results confirmed by K2K [15] and MINOS [16], leading to the best current values of

$$\Delta m_{23}^2 = (2.43 \pm 0.13) \, 10^{-3} \, \text{eV}^2, \qquad \sin^2 2\theta_{23} > 0.90 \, (90\% \, \text{CL.}). \tag{2.5}$$

Due to its smallness, the parameter $\sin^2 2\theta_{13}$ is difficult to measure. On the other hand it is connected to the CP violating phase δ_{CP} which can e.g. shed light on the possible origin of the baryon asymmetry of the Universe. Therefore several experiments try to measure both values with high accuracy. Combining current results from T2K [17], MINOS [18] and DoubleCHOOZ [19] lead to the following values for normal (inverted) hierarchy with 95% CL. [20]

$$0.023 \, (0.027) < \sin^2 2\theta_{13} < 0.16 \, (0.17) \tag{2.6}$$
$$\delta_{CP} = -0.86\pi \, (-0.24\pi). \tag{2.7}$$

2.3 Neutrino Masses

Particles in the Standard Model gain their masses due to the Higgs mechanism: While interacting with the Higgs field they constantly switch handedness. Therefore, mass can be understood as an interaction between the left-handed particle and its right-handed partner. The corresponding mass term $m_{LR}\overline{p_L}p_R$ is known as the Dirac mass, where p can be any massive particle.

To acquaint neutrino masses in an analog way, the Standard Model has to be extended by the existence of right-handed neutrinos. These are not allowed to interact via the weak force because otherwise they would contradict the results from the Goldhaber experiment. Due to the latter, they are called sterile neutrinos. The presence of a right-handed neutrino leads to a Dirac mass as described above. However, this also results in masses on a scale comparable to the other fermions like quarks or electrons. This contradicts results from cosmology which limits the sum of all three neutrino masses to $\sum m_\nu < 0.17$ eV at 95 % C.L. [21], thus orders of magnitudes smaller than the mass of the other fermions.

Since the neutrino is the only fermion in the Standard Model without an electric charge, it is possible that they are Majorana particles and therefore their own antiparticles [22]. In this case the left-handed neutrino ν_L can interact with its own charge and parity conjugated state, the right-handed antineutrino ν_L^C, leading to the Majorana mass term $m_{LL}^\nu \overline{\nu_L}\nu_L^C$. However, this is just possible by extending the Higgs field of the Standard Model, using a Higgs triplet instead of a doublet, since otherwise the Higgs field H^0 is incapable to flip the ν_L into a ν_L^C. On the other hand, the right-handed neutrino can acquaint its own Majorana mass. Since the right-handed neutrino does not take part in known weak interactions, its mass M_{RR} can be arbitrary large. Due to the Heisenberg Uncertainty Principle, the left-handed neutrino can convert via Higgs interaction into a right-handed neutrino for a very short time before converting back. In case of very large M_{RR}, this effectively results in a very small effective Majorana mass for the left-handed neutrino. This is known as the seesaw mechanism [23, 24, 25, 26, 27]. Mathematically, one starts with the seesaw mass matrix

$$M^{\text{seesaw}} = \begin{pmatrix} 0 & m_{LR} \\ m_{LR}^T & M_{RR,} \end{pmatrix} \tag{2.8}$$

with m_{LR} the Dirac masses. Here, $M_{LL} = 0$ since it is not feasible to generate Majorana masses for the left-handed neutrinos without another extension of the Standard Model.

Diagonalizing this matrix leads than to the effective Majorana mass for the left-handed neutrino

$$m_{LL} = m_{LR} M_{RR}^{-1} m_{LR}^T \qquad (2.9)$$

Various variations of this mechanism exist together with other possible extensions of the Standard Model to explain the small neutrino masses. Further details can be found e.g. in [28, 2, 4].

2.4 Neutrino Mass Measurements

There are basically three different approaches to measure the masses of neutrinos. The first one is the measurement of the endpoint energy of the electrons emitted from the β-decay of tritium. Such a direct measurement of the electron neutrino mass has the advantage that it is basically free of theoretical assumptions. The most stringent limit from this method of $m(\nu_e) < 2$ eV (95 %C.L.) [29, 30] bases on the results of the latest generation of experiments performed at the University of Mainz [31] and at the Institute of Nuclear Research at Troitzk [32]. The most promising future experiment in this field is KATRIN [33, 34], built to reach a sensitivity of 0.2 eV.

The second approach is to use cosmological data like temperature fluctuations in the CMB, matter fluctuations at large scales by high statistics galaxy redshift surveys, Lyman-α forest and weak lensing to determine the sum of the neutrino masses. Current best limits are of the order 0.17 eV [21]. However, they suffer from a strong model dependency. The third method looks for the neutrinoless double beta decay described in the following in detail.

2.5 Theory of (Neutrinoless) Double Beta Decay

The neutrinoless double beta decay ($0\nu\beta\beta$) is the only method which can not only measure the neutrino mass but might also answer the question about the nature of neutrinos. In a double beta decay, an (A, Z) nucleus is transformed into an $(A, Z-2)$ nucleus while emitting two electrons and two electron anti-neutrinos:

$$(2\nu\beta\beta) \qquad\qquad (A, Z) \rightarrow (A, Z-2) + 2e^- + 2\overline{\nu_e} \qquad (2.10)$$

This process can only take place if the cascade of two single beta decays is forbidden by energy conservation which means that mother and daughter nuclei have to be more bound than the intermediate state. This condition is fulfilled by a number of even-even nuclei due to the pairing term. It is a Standard Model process which conserves lepton number, the corresponding Feynman diagram can be found in figure 2.2(a). $2\nu\beta\beta$ was first proposed by Maria Goeppert-Mayer in 1935 [35].

As first considered by Furry in 1939 [36], neutrinoless double beta decay ($0\nu\beta\beta$) can take place if neutrinos are Majorana particles

$$(0\nu\beta\beta) \qquad\qquad (A, Z) \rightarrow (A, Z-2) + 2e^-. \qquad (2.11)$$

Although the occurrence of $0\nu\beta\beta$ proofs the Majorana nature of neutrinos [37], there are several possibilities for the vertex shown in the Feynman diagram in figure 2.2(b): light or heavy Majorana particles, right-handed weak interactions mediated by the W_R boson, SUSY particles or other virtual particles [3]. All of them have in common that they violate lepton number conservation and are therefore beyond the Standard Model. Assuming the exchange
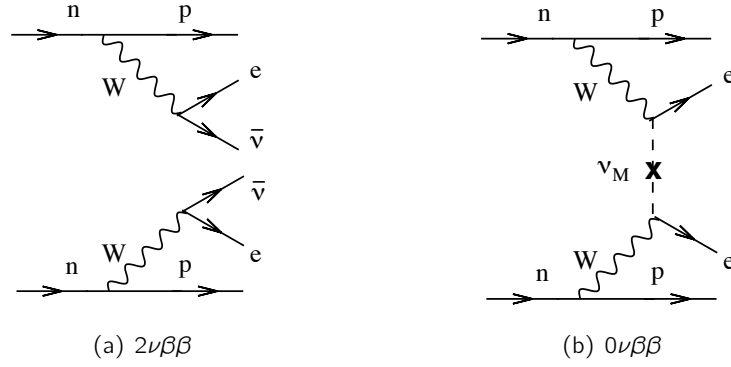
Figure 2.2: Feynman diagrams for the double beta decay with (left) and without (right) accompanied neutrinos. Taken from [4].

of light Majorana neutrinos interacting through the left-handed $V - A$ weak current, the decay rate is given by [38]

$$\left[T^{0\nu}_{1/2}(0^+ \to 0^+) \right]^{-1} = G^{0\nu}(Q, Z) \left| M^{0\nu} \right|^2 \langle m_{\beta\beta} \rangle^2 \tag{2.12}$$

with $M^{0\nu}$ the nuclear matrix element and $\langle m_{\beta\beta} \rangle = \left| \sum_i |U_{ei}|^2 m_{\nu_i} e^{i\alpha_i} \right|$ the effective Majorana mass and $G^{0\nu}$ the precisely calculable phase space integral given by

$$G^{0\nu}(Q, Z) = \frac{1}{2(2\pi)^5} G_F^4 \frac{1}{R^2} g_A^4 \int_0^Q dT_1 \int_0^\pi \sin\theta \, d\theta \, (E_1 E_2 - p_1 p_2 \cos\theta) \, p_1 p_2$$

$$\times F(E_1, (Z+2)) F(E_2, (Z+2)). \tag{2.13}$$

where G_F is the Fermi constant, $R \simeq A^{1/3} \cdot 10^{-13}$ cm the radius of the nucleus, g_A the axial form factor, $T_1 = E_1 - m_e$ the kinetic energy, $E_{1,2}$ and $p_{1,2}$ the energy and momentum of the two electrons, θ the angle between p_1 and p_2 and F the Fermi function. $Q = M_I - M_f - 2m_e$ is the total released energy which can be written in this form since the nuclear recoil energy is negligible due to $M_{i,f} \gg Q$. The process is very rare since it is a second order perturbation theory process including a helicity flip as well as due to the smallness of the neutrino masses.

One has to be careful when translating a measured decay rate into a neutrino mass since there are several possible exchange particles and the exchange of Majorana neutrinos do not have to be the only nor the dominant contribution. Therefore, measurements into several final states in the same nucleus, transitions to the ground state in several nuclei or other lepton flavor violating processes like $\mu \to e$ conversion are necessary to understand the underlying process. In the following, the exchange of a light Majorana particle is always assumed.

Another critical problem is the determination of the nuclear matrix elements which is a complicated nuclear many body problem and cannot be done exactly. Reliability has significantly approved over the last years using the following techniques:

Quasi Random Phase Approximation (QRPA) [39, 40] uses three parameters accounting for pairing, particle-particle and particle-hole interactions. While many single-particle level outside a small inner cone can be taken into account, just very few correlations can be included. Two groups perform QRPA calculations, the Tübingen
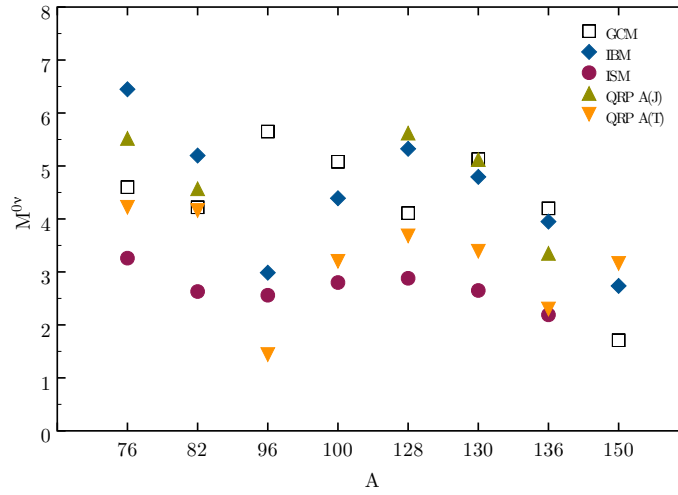
Figure 2.3: Recent NME calculations from different techniques: GCM [44], IBM [43], ISM [42, 47], QRPA(J) [48] and QRPA(T) [49, 50, 51]. Details on the plot can be found in [46], where it was taken from.

group and the Jyvaskyla group. They uses different approaches to determine the constant describing particle-partile interactions.

Interacting Shell Model (ISM) [41, 42] uses the Pauli exclusion principle to describe the structure of the nucleus in terms of energy levels and includes residual two-body interactions among nucleons. Many arbitrarily complicated correlations are included but only a few single-particle states outside the inner cone.

Interacting Boson Model (IBM) In the IBM [43] bosons can interact through 1- and 2-body interactions which give rise to bosonic wave functions.

Generating Coordinate Method (GCM) The last method bases on energy density functional methods using the Gogny D1S functional where beyond mean-field effects are included within the generating coordinate method (GCM) with particle number and angular momentum projection for both initial and final ground states [44, 45].

For details on the calculations as well as their comparison see [46, 39, 4]. Despite the improvements over the last years, there is still no agreement on the actual values for the different isotopes with variations up to a factor of four. Therefore, measurements of $0\nu\beta\beta$ in several isotopes are necessary to reduce the uncertainty in the matrix elements and consequently the effective Majorana mass.

2.6 Neutrinoless Double Beta Decay Experiments

Measurements can be divided into indirect or inclusive and direct or counter methods. Indirect measurements basically count the daughter nuclei and are therefore insensitive to the actual decay mode if not combined with other measurements. Direct measurements can be subdivided into inhomogeneous and homogeneous methods. In inhomogeneous measurements is the source outside the detector which usually allows to measure both electrons separately. The event topology as well as angular correlation of the electrons can be used to identify the signal and reduce the background. Furthermore, the usage of several different

Figure 2.4: Calculated spectrum of the summed energy of both electrons from double beta decay in ^{76}Ge. In the $2\nu\beta\beta$ case, the spectrum is continuous because the neutrinos carry away some energy whereas the $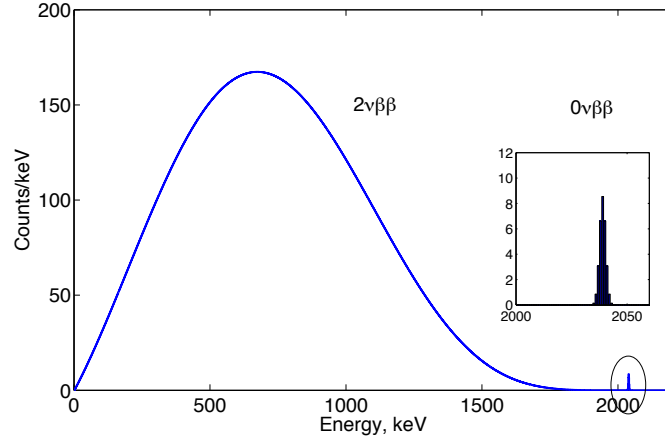0\nu\beta\beta$ decay creates a peak at the Q-value of 2039 keV just smeared with a typical energy resolution of 3 keV FWHM at 2 MeV. Used half lives are $T_{1/2}^{2\nu} = 1.7 \cdot 10^{21}$ y and $T_{1/2}^{0\nu} = 1.2 \cdot 10^{25}$ y. Taken from [52].

isotopes is possible. Disadvantages of this method are usually small masses, low efficiencies and a worse energy resolution. In homogeneous experiments the source also serves as detector which allows high masses as well as a very good detection efficiency. They usually also have a good energy resolution. A drawback is the measurement of both electrons together which does not allow the usage of angular correlations for background reduction. Thus, other methods to identify background signals have to be found.

The summed energy of both electrons can be used to differentiate neutrino accompanied and neutrinoless double beta decay. As shown in figure 2.4, in the neutrino accompanied decay the electron spectrum is a continuum because the neutrinos carry away some energy whereas the neutrinoless decay creates a peak at the Q-value smeared by the detector resolution.

Experiments are limited in their sensitivity due to their total mass M, measuring time t, background in the region of interest B, energy resolution ΔE as well as event detection and identification efficiency ϵ, as expressed by [53]:

$$T_{1/2}^{0\nu} = \frac{4.16 \times 10^{26} \text{ y}}{n_\sigma} \left(\frac{\epsilon a}{W} \right) \sqrt{\frac{M \times t}{\Delta E \times B}} \qquad (2.14)$$

with a the isotopic abundance, W the molecular weight of the source material and n_σ the number of standard deviations corresponding to a given confidence level. Figure 2.5 shows the expected 90 % probability lower limit on the half-life versus the exposure $M \times t$ under different background conditions. It demonstrates the importance of an increase in mass and a reduction in background to improve the sensitivity of an experiment. Experimentally available information is the sum of the electron energies, single electron energy and angular distributions as well as identification and counting of the daughter nucleus. Usually, more detailed information leads to a better background discrimination but has to be bought with less detection efficiency or detector mass. Thus, different experiment try different approaches to balance the different parameters.

The $2\nu\beta\beta$ decay was first detected in ^{130}Te by Inghram and Reynolds in 1950 with a
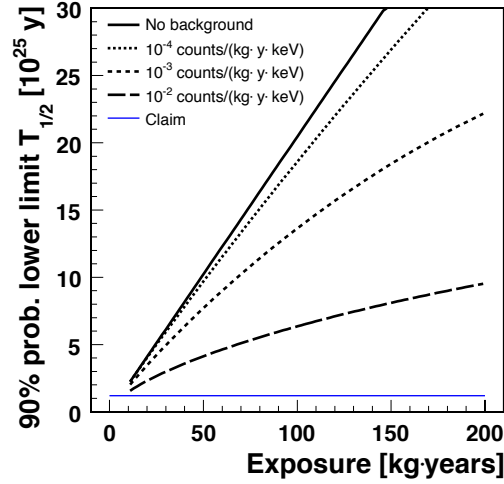
Figure 2.5: The expected 90 % probability lower limit on the half-life for the $0\nu\beta\beta$ decay in germanium detectors is plotted versus the exposure under different background conditions. The half-life for the claimed observation for the $0\nu\beta\beta$ decay of ^{76}Ge [54] is also shown. Taken from [55].

half live of $T_{1/2}^{2\nu} = 1.4 \times 10^{21}$ y [56]. Measurements in several other isotopes followed and today, around ten double beta decaying isotopes are known. The currently best results on $T_{1/2^{2\nu}}$ for the most important isotopes used in future experiments can be found in table 2.1.

The $0\nu\beta\beta$ decay on the other hand, with its several orders of magnitude longer half live, is much more difficult to detect. So far, there exist a claim of a measurement by a subgroup of the Heidelberg-Moscow experiment (Klapdor-claim) [57, 58]. The experiment used high-purity germanium detectors and collected 71.1 kg y of data. With a background level of 0.11counts/(keV·kg·y) a half live of $T_{1/2}^{0\nu} = (2.23^{+0.44}_{-0.31})10^{25}$ y and an effective Majorana mass of $\langle m_{\beta\beta} \rangle = 0.32 \pm 0.03$ eV with a 6.4σ evidence were found. The spectrum in the region of interest from their first publication can be found in figure 2.6 together with the fit for the peak at the Q-value of the $0\nu\beta\beta$ in germanium, which is at 2039.006(50) [59]. The results are controversially discussed in the community [60] and need to be verified by future experiments. Other experiments have measured only upper limits for the half live of the $0\nu\beta\beta$ so far.

Table 2.1 gives an overview about the half life limits of the most relevant isotopes indicating also current and future experiments using them in their $0\nu\beta\beta$ search.
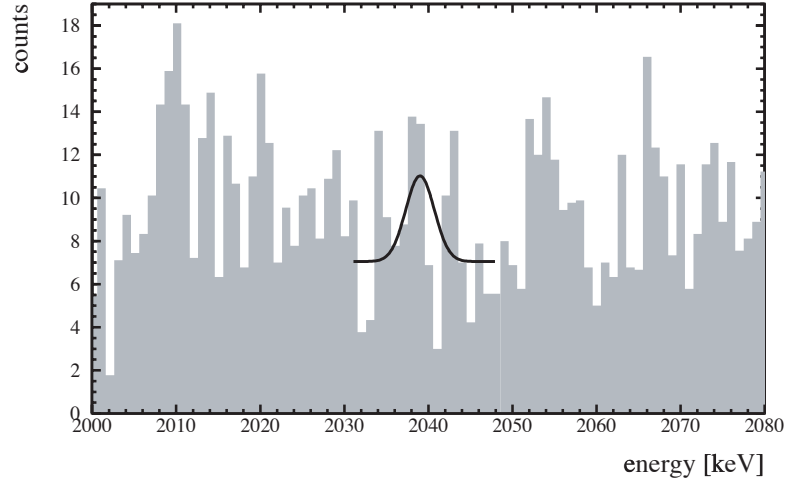
Figure 2.6: Energy spectrum of the Heidelberg-Moscow experiment. The sum spectrum of 5 detectors is shown over the period August 1990 to May 2000, (54.9813 kg y) in the energy interval 2000-2080 keV, around the Q-value of double beta decay summed to 1 keV bins. The black curve shows the claimed $0\nu\beta\beta$ signal. [57]

Isotope	Q-value [keV]	$T^{2\nu}_{1/2}$ [10^{19} y]	$T^{0\nu}_{1/2}$ [y]	Experiments
^{48}Ca	4272	$4.4^{+0.6}_{-0.5}$	$> 5.8 \times 10^{22}$ [61]	CANDLES
^{76}Ge	2039	150 ± 10	$> 1.9 \times 10^{25}$ [62]	GERDA, Majorana
^{82}Se	2996	9.2 ± 0.7	$> 3.2 \times 10^{23}$ [63]	SuperNEMO
^{100}Mo	3034	0.71 ± 0.04	$> 1.0 \times 10^{24}$ [63]	MOON
^{130}Te	2528	68 ± 12	$> 2.8 \times 10^{24}$ [64]	CUORE
^{136}Xe	2459	> 81 [65]	$> 4.5 \times 10^{23}$ [66]	EXO, KamLAND
^{150}Nd	3367	0.82 ± 0.09	$> 1.8 \times 10^{22}$ [67]	SNO+

Table 2.1: Measured half life limits for the most important isotopes used in current and future experiment. All bounds are given with 90% CL. Data for $T^{2\nu}_{1/2}$ taken from [5], rest from [68].

Signal Formation and Detection 3

The following chapter is a quick review on the interaction of different types of radiation with matter and their detection in semiconductor detectors. The latter focuses on germanium detectors as they are used in GERDA. It is based on [69] and [70], which can be consulted for further information or references.

3.1 Interaction of Particles with Matter

Charged particles continuously interact with matter via the Coulomb force while uncharged, massive particles undergo major encounters, e.g. scattering events, usually involving the nucleus of the material. The photon on the other hand can interact with both, the electrons as well as the nucleus of the material. Thus, for a description of the different processes and their probabilities it is helpful to distinguish individual type of particles as well as their energy.

Heavy Charged Particles

Heavy charged particles as α particles interact primarily via the Coulomb force with the orbital electrons, exciting or ionizing the absorber atom. The energy loss in each interaction is small, resulting in almost no angular deflection. Since several of them occur simultaneously, the resulting particle track is nearly a straight line. The linear stopping power for charged particles in an absorber is described by the Bethe-Bloch formula [70, 71], depending mainly on the energy of the particle as well as the number density and the atomic number of the absorber atoms:

$$-\frac{dE}{dx} = 2\pi N_A \, r_e^2 \, m_e^2 \, c^2 \, \rho \, \frac{Z}{A} \frac{z^2}{\beta^2} \left[\ln \left(\frac{2m_e \gamma^2 v^2 W_{\mathrm{max}}}{I^2} \right) - 2\beta^2 \right] \tag{3.1}$$

where N_A is the Avogadro's number, r_e and m_e the electron's radius and mass, z the charge of the incident particle in units of e, ρ, Z and A density, atomic number and atomic weight of the absorbing material, $\beta = v/c$ of the incident particle, $\gamma = 1/\sqrt{1-\beta^2}$, W_{max} the maximum energy transfer in a single collision and I the mean excitation potential. It results in stopping ranges between a few mm up to a few cm.

Fast Electrons

Due to their smaller mass, electrons can loose significantly more energy in a single interaction compared to heavy charged particles. This results in less encounters and more tortuous

tracks. Sometimes even electron-nucleus scattering occur which abruptly change the elec-
tron's energy. The energy loss is again described by the Bethe-Bloch formula. Furthermore,
fast electrons can loose energy in form of radiative processes, bremsstrahlung. However,
radiation losses are just a small fraction of the energy lost due to ionization or excitations
and are only significant in absorber materials of high atomic number. For equivalent energy,
the specific energy loss of electrons is much lower compared to heavy charged particles and
thus their mean free path hundreds of times longer. Positrons differ from electrons in the
fact that they annihilate at their end point, resulting in two 511 keV photons. The double
beta decay signal is due to fast electrons.

Gamma Rays

There are three major interaction mechanisms for photons with matter: Photoelectric ab-
sorption, Compton scattering and pair production. All three result in a transfer of photon
to electron energy and in a sudden change in the photon history which either disappears or
scatters over a large angle. Gamma rays are used in GERDA for calibration and produce a
significant part of the measured background in the region of interest.

Photoelectric Absorption

In a photoelectric absorption process, the incoming photon is absorbed by a shell electron
of the absorber. Depending on the energy of the photon, the electron is either excited to
a higher state or escapes with an energy $E_{e^-} = h\nu - E_b$ where E_b represents the binding
energy of typically a few hundred eV. The following de-excitation of the atom might result
in the generation of X-ray photons which are usually quickly reabsorbed. In some cases,
the excitation energy of the atom is carried away by Auger electrons. This process is
predominant for low energetic photons and enhanced for absorber materials of high atomic
number. Owing to the shell structure of the electron cloud, the cross section μ_{ph} shows
jumps in the low energy region until the escape energy is reached:

$$\mu_{ph} \propto \frac{Z^n}{(h\nu)^{3.5}} \tag{3.2}$$

with n varying between 4 and 5 over the photon energy region of interest [69, 72].

Compton Scattering

In Compton scattering the incoming gamma ray is deflected through an angle θ by an
electron in the absorber. The energy transfer to the electron can be written as

$$h\nu\prime = \frac{h\nu}{1 + \frac{h\nu}{m_0 c^2}(1 - \cos\theta)} \tag{3.3}$$

where $h\nu$ is the initial energy of the photon and $m_0 c^2 = 511$ keV the electron rest mass.
The differential cross section can be described by the Klein-Nishina formula [73] showing
an increasing tendency of forward scattering with increasing photon energies. Usually all
scattering angles occur in a detector resulting in a continuous energy spectrum for the
recoil electron (Compton continuum) up to the maximum energy of the head-on collision
(Compton edge) as shown in figure 3.1. The shape of the continuum is predicted by
the Klein-Nishina formula. The fact that the electron is initially bound in the detector
material leads to a rounding-off of the rise in the continuum near its upper extreme and the
introduction of a finite slope to the abrupt drop of the Compton edge. This effect might be
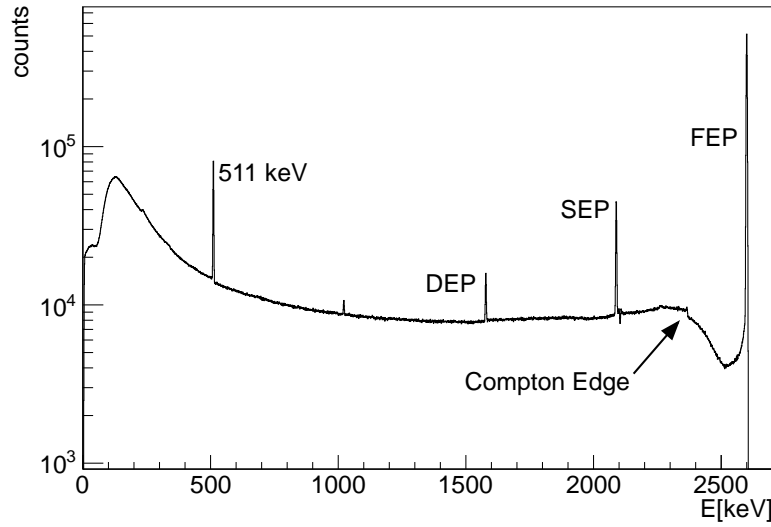
Figure 3.1: Monte Carlo simulated energy spectrum of 2.6 MeV gammas in a germanium detector showing the different features of Compton scattering with the Compton continuum and the Compton edge together with effects from pair production with both, the single and the double escape peak, along with the 511 keV line due to annihilation radiation from interactions in surrounding materials.

masked by the energy resolution of the detector. The cross section μ_C is nearly independent of Z:

$$\mu_C \propto \frac{1}{h\nu} \tag{3.4}$$

Pair Production

If the photon exceeds twice the electron rest mass, pair production in the Coulomb field of a nucleus is energetically possible although its probability stays low until the photon reaches several MeV. All energy of the disappearing photon above twice the electron rest mass goes into the kinetic energy of the created electron and positron which will then loose it according to the above description. The positron will annihilate into two secondary photons with an energy of 511 keV each, which then can either deposit their energy in the detector or escape. This results in two more peaks besides the full absorption peak: The single and the double escape peak with one or both annihilation photons escaping the detector, as shown in figure 3.1. There is no simple expression for the cross section of pair production per nucleus but its magnitude varies approximately as the square of Z:

$$\mu_{\text{pair}} \propto Z^2 \ln \left(2 \frac{h\nu}{m_0 c^2} \right) \tag{3.5}$$

Gamma Ray Attenuation

Photons traveling through an absorbing material on their way to a detector are either absorbed or scattered away by the processes described above. The decrease of the photon beam intensity is described by a simple exponential law characterized by a fixed probability of occurrence per unit path length in the absorber:

$$I = I_0 \cdot e^{-\mu x} \qquad \text{linear attenuation} \tag{3.6}$$

$$\text{with } \mu = \mu_{\text{ph}} + \mu_C + \mu_{\text{pair}} \tag{3.7}$$
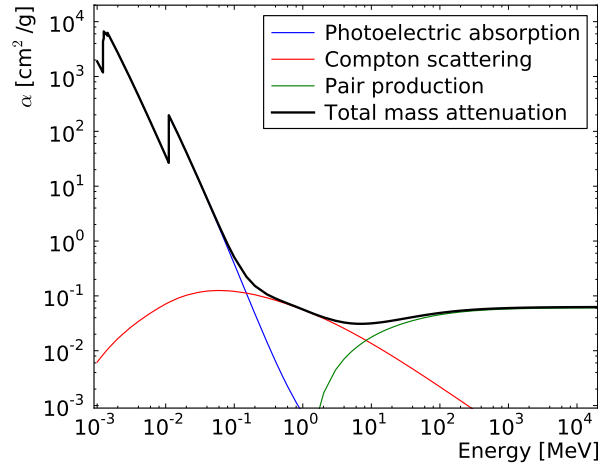
Figure 3.2: Mass attenuation coefficient for germanium as a function of energy. Besides the total attenuation, the different contributions from photoelectric effect, Compton scattering as well as pair production is shown. Data taken from [74].

where x is the thickness of the absorber. The photons can also be characterized by their mean free path $\lambda = 1/\mu$ which is the average distance the photon travels before an interaction. Since the linear attenuation coefficient varies with the density ρ of the absorber, the mass attenuation coefficient is usually used:

$$\alpha = \frac{\mu}{\rho} \tag{3.8}$$

$$\Rightarrow \quad \lambda = \frac{1}{\alpha \rho} \tag{3.9}$$

$$\Rightarrow \quad I = I_0 e^{-\alpha \rho x} = I_0 e^{-\frac{x}{\lambda}} \tag{3.10}$$

The quantity ρx is known as the mass thickness and often used to describe the thickness of absorbers used in radiation measurements. The total mass attenuation coefficient of germanium is shown as a function of energy together with the contributions from the different processes of gamma interaction are shown in figure 3.2.

Neutrons

Since neutrons interact primarily with the nucleus of the absorbing material, they are either absorbed, followed by some secondary radiation, or their energy and direction is changed significantly. Secondaries are almost always heavy charged particles. Since neutrons interact with the nucleus, their mean free path is usually many centimeters. The relative probability of the different types of neutron interactions changes significantly with their energy. For simplification, the following description divides them into slow ($E < 0.5$ eV) and fast ($E > 0.5$ eV) neutrons.

Slow Neutrons

One significant interaction for slow neutrons is elastic scattering. Since very little energy is transferred to the absorber per event, it is typically not a detection interaction. In most materials, the radiative capture reaction (n,γ) is very likely for slow neutrons and therefore plays an important role for attenuation or shielding. For detectors though, reactions such

as (n,α), (n,p) and (n,fission) are much more attractive because their secondaries are easier to detect due to their charge.

Fast Neutrons

With increasing energies, scattering events become more important since an increasing amount of energy can be transferred to the participating nucleus (recoil nucleus). If the energy is sufficiently high, inelastic scattering can take place where the recoil nucleus is elevated to one of its excited states, emitting photons for de-excitation.

In case of neutrons, the linear attenuation coefficient from equation (3.6) is replaced by the total macroscopic cross section

$$\Sigma_{tot} = N \cdot (\sigma_{scatter} + \sigma_{(n,\gamma)} + \dots) \tag{3.11}$$

$$\Rightarrow \quad I = I_0 \cdot e^{-\Sigma_{tot}x} \tag{3.12}$$

where N is the number of nuclei per unit volume and σ_i the cross sections for the different processes involved. The mean free path is defined via $\lambda_n = 1/\Sigma_{tot}$ accordingly.

3.2 Germanium Detectors

Semiconductor detectors provide the best energy resolution compared to any other common detector because they produce the largest number of charge carriers for a given event. Improvements in purification techniques, especially for germanium, allows their usage not only for charged particle spectroscopy but also gamma-ray measurements. This and the fact that ^{76}Ge is a double beta decayer makes germanium detectors extremely interesting for double beta decay experiments.

General Principle

Insulators, semiconductors and conductors can be distinguished due to their band gap between valence band and conduction band. Semiconductors, elements from the fourth group in the periodic system, are characterized by a small gap between these bands (around 1 eV at room temperature), making them insulators at absolute zero. With increasing temperature thermal excitation lifts up electrons from the valence into the conduction band. The band gap in insulators is too large for such an excitation while the two bands overlap in case of conductors.

Doping a semiconductor with either trivalent or pentavalent impurities provides additional charge carriers which are either positive (holes) or negative (electrons). In the first case these impurities are called acceptors, in the later donors. Typical doping concentrations are of the order of 1 particle per million but can vary between mildly doped materials (π- or ν-type) with concentrations as low as 1 particle per trillion and highly doped materials (p^+ or n^+) with much higher concentrations.

A p-n junction creates a discontinuity in the conduction electron density resulting in a diffusion of electrons (holes) in the p- (n-) type material where they can recombine and leave immobile ions behind. The result is the build-up of an electric field which diminishes the tendency for further diffusion until an equilibrium is reached. The region over which the charge imbalance exists is called depletion zone. Its thickness d depends on the doping
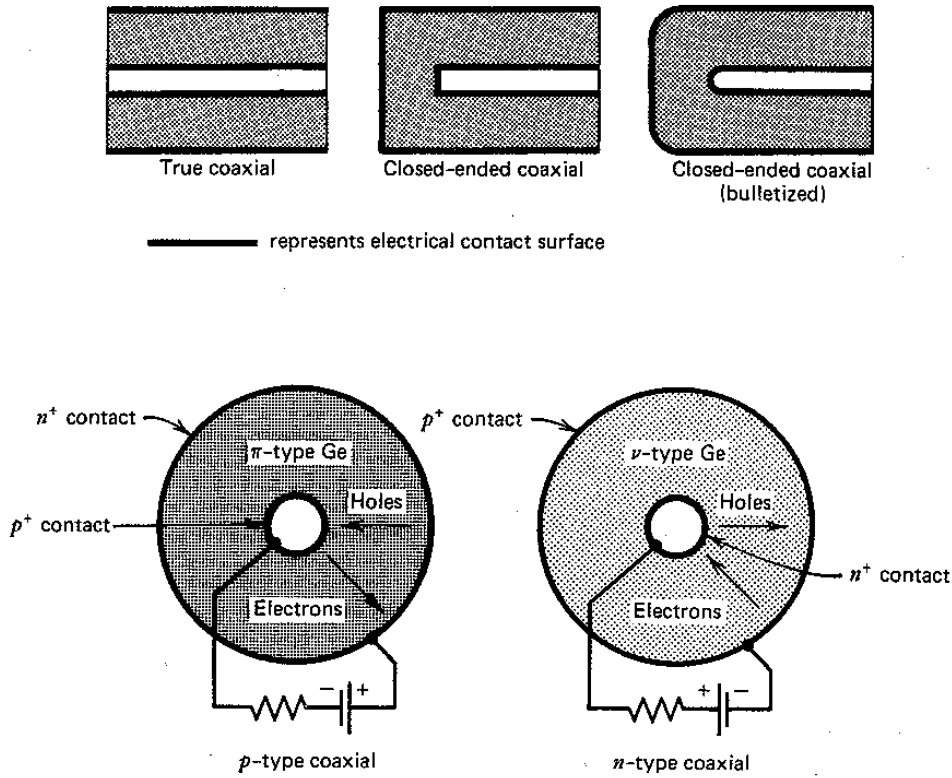
Figure 3.3: Schematics of p-type and n-type coaxial detectors commonly used. The top row shows the cross-sectional view through the axis of a cylindrical crystal. The bottom row shows a cross-sectional view perpendicular to the cylindrical axis. The trajectories of electrons and holes in the different types are indicated together with the polarity of the biased voltage used to deplete the detector. Taken from [69].

level N and can be varied with an applied bias voltage V:

$$d \cong \left(\frac{2\epsilon V}{eN} \right)^2 , \qquad (3.13)$$

where ϵ is the dielectric constant and e the electron charge. For the usage as detector, revers bias is used, which extends the depletion zone typically until it captures the full detector. A further increase in the bias voltage leads to a simultaneous increase of the electrical field everywhere in the detector and therefore a more homogeneous field. Impurities in the material lower the possible depletion thickness for a given bias voltage and are therefore unwanted. Different doping levels lead to an asymmetric depletion zone extended into the side with the lower doping concentration. Figure 3.3 shows schematics of different types of detectors indicating also the trajectory of electrons and holes together with the polarity of the biased voltage used to deplete the detector.

Particle interactions with the detector create electron-hole pairs. The necessary ionization energy is around 3 eV with very small dependencies on the type of the particle as well as the temperature but independent of the particle's energy. Due to the electric field present in the detector both charge carriers separate immediately and travel to each side of the detector. Their drift velocity is proportional to the field strength until reaching a plateau at typically around 10^3 V/cm. Saturation velocities are of the order of 10^7 cm/s [75].

Detector Production and Characteristics

A possible technique to lower the level of impurities in the detector material is called zone refinement: The material is locally heated and the melting zone slowly moved from one side of the sample to the other, sweeping out the impurities. Several iterations lead to impurity levels as low as 10^9 atoms/cm^3 (0.02 ppt). Due to the lower melting point of germanium of 937 °C compared to e.g. silicon with 1415 °C, higher purification levels can be reached. The resulting material is so called High-Purity Germanium (HPGe). Higher purification levels lead to larger possible depletion thicknesses (see equation 3.13, replacing the dopant concentration with the impurity level) and therefore larger active masses of the detector, what is highly desirable in case of $0\nu\beta\beta$ experiments.

The resulting material is used to grow the crystal from which the detector is cut (wafer), and it is either π- or ν-type. For simplicity, just the π-type is assumed in the following. A junction with the π-type bulk is created by lithium evaporating and diffusion or by direct implementation of n$^+$ dopants (e.g. phosphorus) on one side of the wafer. This is called the rectifying contact which typically has a thickness of a couple of hundred micrometers. Owing to the large difference in doping levels, the depletion zone primarily extend into the bulk. Even with bias voltage a thin layer of nearly the thickness of the contact remains outside the depletion zone; it is called dead layer. The necessary blocking contact on the other side of the wafer is created by evaporating p$^+$ dopants (e.g. boron). This contact can typically be manufactured much thinner, with thicknesses of a few tenth of a micrometer, and is also a dead layer.

The small band gap makes operation of semiconductor detectors at room temperature impossible because of the large number of thermally excited electrons resulting in a large constant current even in the absence of any ionizing radiation. This current is called leakage current and can be reduced to a tolerable level by cooling the detector with the help of liquid nitrogen or argon to temperatures around 80 K.

The crystals from which the detectors are produced have a diameter of a few centimeters. In combination with the maximum depletion depth this limits the maximum active volume. Three configurations are typically used: Planar disk-like detectors, coaxial cylindrical detectors and point contact detectors. Planar detectors have one electrode on each side. Coaxial detectors have their inner core removed in order to place there one of the electrodes while the other is on the outer surface. This allows much larger active volumes since they can be extended in height. Figure 3.3 shows the different types of commonly used coaxial detectors.

Most commercially available HPGe detectors come in closed-ended coaxial configuration where only a part of the core is removed, leading to a horseshoe cross section. This avoids leakage currents at the front surface. Rounding edges eliminate low-field regions in the edges. Typically, the rectifying contact is on the outer surface leading to a lower depletion voltage and higher electric field strength in a bigger volume of the detector than placing the rectifying contact on the inner surface.

Point contact detectors have similar shapes than planar detectors but the size of their signal read-out electrode is significantly reduced. This results in an inhomogeneous electric field and thus a strong position dependency of the pulse shapes. This can be for example be used for a discrimination of single-side and multi-side events. The Broad Energy Ger-

(a) Side view of a BEGe

(b) 2D view of a BEGe with electron and hole trajectories
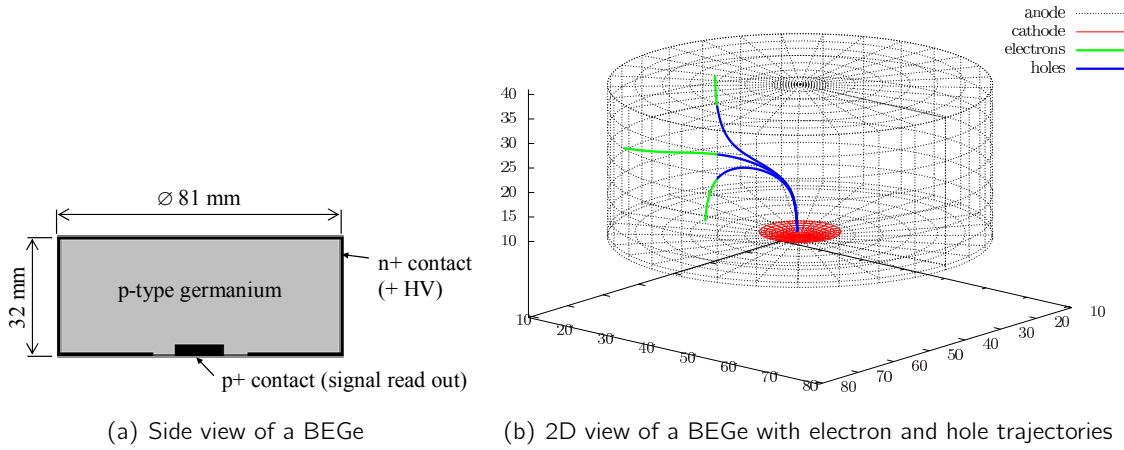
Figure 3.4: Broad energy germanium detectors as used in GERDA's phase II. Figure (a) shows a side view of the detectors with its dimensions indicating the electrodes. Taken from [77]. Figure (b) shows a 3D view of the detectors with the computed trajectories of electrons and holes for three different interactions points. Taken from [78].

manium detectors (BEGe) [76], which will be used in GERDA, uses a similar approach. It is shown in figure 3.4.

Three factors have an influence on the energy resolution, which is usually defined by the full width at half maximum (FWHM) of a reference peak: The inherent statistical fluctuation in the number of charge carriers, variations in the charge collection efficiency and electronic noise. The variance in the number of charge carriers is a combination of Poisson statistics, assuming that all ionization processes are independent from each other, and the so called Fano-factor describing the observed deviations from this assumption; it depends on the energy of the ionizing particle. The influence of the two other effects can be measured. Typical energy resolutions in large coaxial detectors range from 0.8-1.2 keV at 122 keV to 1.7-2.3 keV at 1333 keV.

To reach the shortest possible charge collection time, detectors should be operated with a field strength high enough to reach saturation velocity for both, electrons and holes. They nonetheless need about 100 ns to travel a distance of 1 cm, limiting the timing properties of the detector. Furthermore, the pulse shapes collected by the electrodes vary with the position of the interaction as can be seen in figure 3.5. The Shockley-Ramo theorem [79, 80, 81] can be used to calculate currents or charges induced at the electrodes.
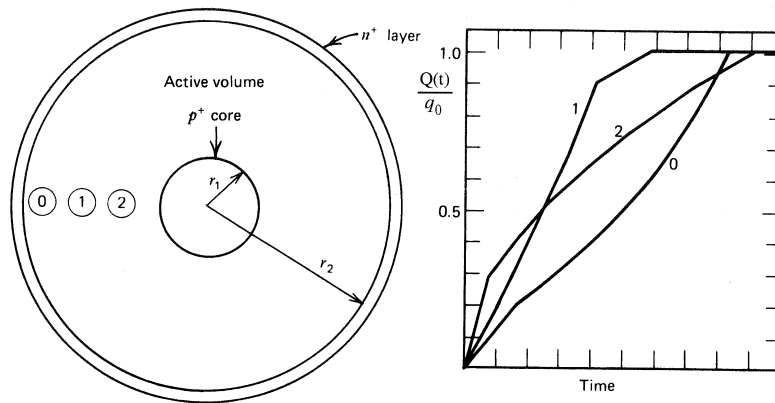
Figure 3.5: Leading edge of the output pulse of a coaxial detector from three different interaction points. From [69, 82].

The GERDA Experiment 4

4.1 Design of the Experiment

The GERmanium Detector Array GERDA [83] is an experiment searching for the neutrino-less double beta decay ($0\nu\beta\beta$). As shown in section 2.6, high mass, good energy resolution as well as a low background are essential for the success of such an experiment. Semi-conductor diodes provide a very good energy resolution; ^{76}Ge is a double beta decayer and since germanium diodes allow large masses together with high purity, they are a natural choice for $0\nu\beta\beta$ searches. The still unverified Klapdor-claim (see section 2.6), obtained by measurements with high-purity germanium (HPGe) detectors, makes their usage even more attractive. The Heidelberg-Moscow (HdM) results also showed, that a further background reduction is necessary to improve the signal to noise ratio. This was the main goal in the design of the GERDA experiment.

GERDA is located at Laboratori Nazionali del Gran Sasso (LNGS), an underground lab in Italy, where 3200 mwe [84] (equivalent vertical depth relative to a flat overburden) of rock shield the experiment from cosmic radiation. The detector array consists of natural HPGe detectors (7.44% of ^{76}Ge) and enriched HPGe detectors (86% of ^{76}Ge). To reduce the amount of material close to the detectors, they are submerged nakedly into the liquid argon (LAr) which acts simultaneously as cooling liquid as well as shielding material. If equipped with photomultipliers, it can be used as an active veto [85]. The cryostat, made from stainless steel with an inner copper lining, has an inner diameter of 4 m and an overall height of 8.9 m, containing about 64 m^3 of LAr. It is surrounded by a stainless steel water tank with a diameter of 10 m and a height of 8.5 m containing about 580 m^3 of ultra pure water. The water tank is equipped with 66 photomultipliers for the Cherenkov muon veto, which is completed with a total of 32 plastic panels. On top of cryostat and water tank is the clean room with the lock and the lowering systems for detectors and calibration sources. All materials, especially those close to the detectors, are carefully screened for radioactive contamination, and just those with the lowest backgound contribution in the region around the Q-value were chosen. Figure 4.1 shows an artist view of the GERDA experiment labeling the different parts.

The experiment is planned in two phases. Phase I uses a total of eight reprocessed HdM [62] and IGEX [86] closed-ended, coaxial detectors enriched in ^{76}Ge, together with natural germanium detectors from the Genius Test Facility [87]. A total of 17.7 kg of germanium is reached. The goal is to improve current limits on the $0\nu\beta\beta$ sensitivity in only a year of data taking with an exposure of 15 kg·y and a background of 10^{-2} counts/(keV·kg·y). In case no events will be observed above background, a half life limit of $T_{1/2} > 2.2 \times 10^{25}$ y can be es-

Figure 4.1: Artist view of the GERDA experiment (not scaled) labeling the different parts of the experiment.

tablished, resulting in an upper limit for the effective neutrino mass of $m_{ee} < 0.23 - 0.39$ eV [88].

Phase II will use in addition newly developed broad-energy germanium detectors [89] enriched in ^{76}Ge, leading to a total mass of about 40 kg. Their inhomogeneous electrical field allows a better discrimination between single-site (signal) and multi-site (background) events using pulse shape analysis compared to coaxial detectors [77]. A further improvement of the background by one order of magnitude compared to phase I is planned, which leads with an aimed exposure of 100 kg·y to a half life sensitivity of $T_{1/2} > 15 \times 10^{25}$ y and a corresponding effective neutrino mass of $m_{ee} < 0.09 - 0.15$ eV [88].

4.2   History and Status of the Experiment

The GERDA experiment was proposed in March 2004. Exactly four years later, the on-site construction phase started with the arrival of the cryostat, followed by the water tank end of April 2008. In summer it became obvious that the final lock system including the lowering systems for detectors and calibration system will not be ready for the start of phase I. Instead, all efforts went into the extension and modification of the lock system which was planned to be used for the commissioning above ground. The influence on the calibration system and therefore this work will be discussed later in detail. In February 2009 the construction of the clean room started, in summer the muon veto, and end of the year, first water the tank and then the cryostat were filled. The first calibration system was installed in January 2010 followed by the lowering system for the first detector string. On 02 June 2010, the first string with three natural germanium detectors was deployed and GERDA started its commissioning phase. Pictures can be found in figure 4.2.

During the commissioning phase, the detector performance as well as the background were studied. An energy resolution between $3.6 - 5$ keV FWHM at 2.6 MeV was found. One way

(a) Arrival of the cryostat in March 2008.

(b) After the construction of the wavelength shifting foil and the PMTs for the Cherenkov muon veto in August 2009.

(c) The clean room
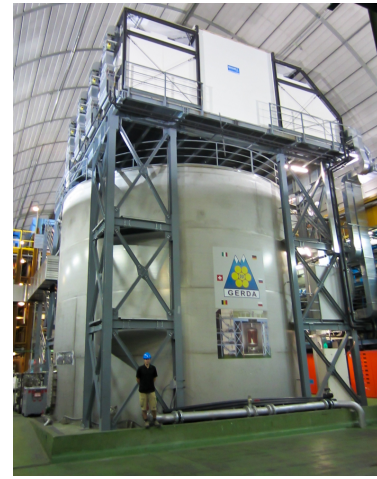
(d) The fully constructed GERDA experiment.

Figure 4.2: Pictures from the GERDA construction phase.

to improve this is an optimization of the offline pulse processing as will be shown in chapter 7. As an encouraging first result, the background in the $2\nu\beta\beta$ region fits well with a $2\nu\beta\beta$ decay with a half life of $1.74 \cdot 10^{21}$ y spectrum produced by Monte Carlo simulations [90].

The surprise of this phase was that the background was around 18 times higher than expected. An unexpectedly large peak at 1525 keV leads to the conclusion that at least a significant part of it comes from ^{42}Ar decaying via ^{42}K into ^{42}Ca. Further investigations lead to the assumption that the contamination of ^{42}Ar in the LAr might be larger than expected and that the ^{42}K ions are collected on the outer surface of the detectors. A thin copper cylinder around the detectors, which can be biased with high voltage if necessary, improved the background in the region around the Q-value by a factor of three and is used in the current setting. Possible other sources are Compton continuum events from thorium and uranium decays, degraded α particles and background from cosmogenically produces isotopes in the detectors. Although the background during the commissioning phase with 0.055 counts/(keV·kg·y) is higher than expected, it is worth pointing out that it is nonetheless already a factor of two lower than the background reached by the Heidelberg-Moscow

collaboration, which was found to be 0.11 ± 0.01counts/(keV·kg·y), and further improvements e.g. by using pulse shape discrimination are expected.

In June 2011, the first enriched detectors were deployed, showing similar results as the natural ones. After a few more tests on detector performance and background, GERDA's phase I officially started in November 2011.

4.3   The Calibration System

The purpose of the calibration system is the energy as well as pulse shape calibration of the HPGe detectors as well as a monitoring of the relevant parameters, such as energy resolution and long term stability. The detectors are arranged in strings of three detectors each. Originally, phase I was planned with five strings including all available detectors (eight enriched as well as five natural detectors). This changed with the commissioning lock, primary due to one reason: The lowering systems for the detectors. For the commissioning phase, it was planned to lower just one detector string and the system was built accordingly. After some investigations, an extensions up to three stings was possible, but not more, leading to the necessity of a second, separate lowering system for the detectors. Another limitation came from the neck of the cryostat which is closed by a CF 630 flange limiting the available space. A sketch including the relevant dimensions can be found in figure 5.1. As a results, one lowering system with three detector strings and one with one detector string were built.

Since the CF 630 flange (cluster flange) was newly designed, position and number of the calibration sources were somewhat flexible, just limited by the available space. Besides this, the type of calibration source as well as the necessary activity had to be determined. The process is described in chapter 5. To avoid contamination of the LAr, the calibration sources should not be removed but stay on top of the cryostat above the cluster flange. Therefore the resulting background contamination had to be determined together with the required shielding which is shown in section 5.6.

Owing to the change of the lock system, it was necessary to design a separate lowering system for the calibration sources. For the first version, this was primarily done by the group at LNGS with assistance of the UZH group. This system was installed in January 2010. Unfortunately, there was an accident in September 2010 resulting in one calibration source falling into the cryostat. The reason could never be fully discovered but it became obvious that the lowering system needs additional error handling and safety functions to prevent this from happening again. Details can be found in section 6.4. For the design, construction and testing of the new system, the UZH group was fully responsible and it is described together with the previous systems in chapter 6. After the installation of a preliminary system in November 2010, the final system was installed in June 2011 and is operating smoothly since then.

Monte Carlo Simulations 5

To determine the relevant parameters and characteristics of the calibration system, such as type and activity of the sources used, the required number of sources as well as their optimum position, Monte Carlo simulations (MCS) were used. MCS were also used to determine the background in the region of interest around the Q-value produced by the calibration sources. A detailed description follows in the next sections. This work focuses on phase I of the experiment, although most of the results can be transferred to phase II as well.

A calibration run, including the movement of the sources from their parking position down to the detector array, taking the actual data and moving them up again, should not take longer than about half a day. This gives some restrictions on the actual source strength as well as on the number and positions of the sources, since all detectors need to reach enough statistics for energy as well as pulse shape calibration within this time. Pulse shapes can be used to distinguish signal from background events. On the other hand, the sources stay at the top of the cryostat during a physics run, and their radiation might contribute to the background in the detectors. Therefore, the activity of the calibration sources should not be too high, such as to enable sufficient shielding while in parking position, to ensure a low background contribution. Both restrictions have to be balanced carefully. Furthermore, the physically available space for parking the sources as well as the lowering systems have to be taken into account.

5.1 Geometry and Simulations

The MCS were performed with MaGe [91], a package based on Geant4 [92], which simulates the geometry of the entire GERDA experiment as well as all relevant physics processes. All parts of the experiments were included in the simulation as realistic as possible. For this work, just the cryostat and its interior are of interest. For simplicity, figure 5.1 shows a scaled view of the relevant parts of the simulation, although much more details are actually included in the geometry.

During a physics run, the calibration sources stay in their parking position on top of the cryostat and about 3 m of LAr and 2 m of argon gas shield the detectors from their radiation. During a calibration run, the sources are lowered over about 5 m down to the detector array in the middle of the cryostat. Data is taken at the relevant positions to be determined before the sources are lifted up again to the parking position.

The detector array consists of four detector strings with three detectors each. Their hor-
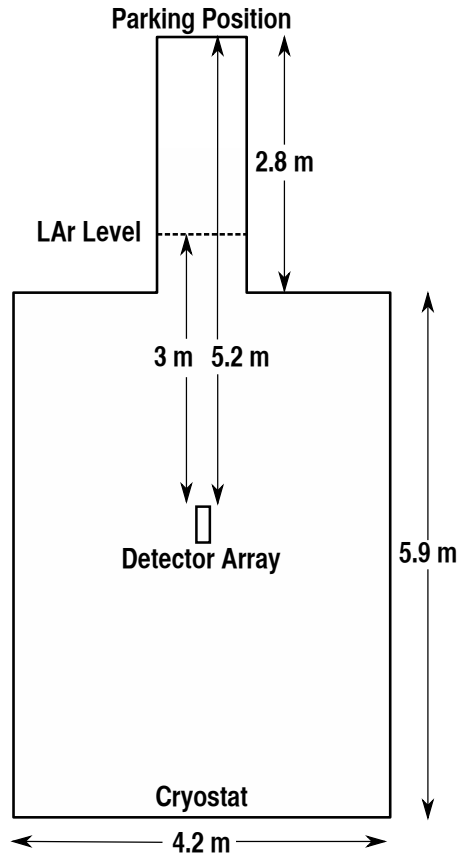
Figure 5.1: Scaled sketch of the GERDA cryostat. Indicated are the positions of the detector array as well as the parking position for the calibration sources.
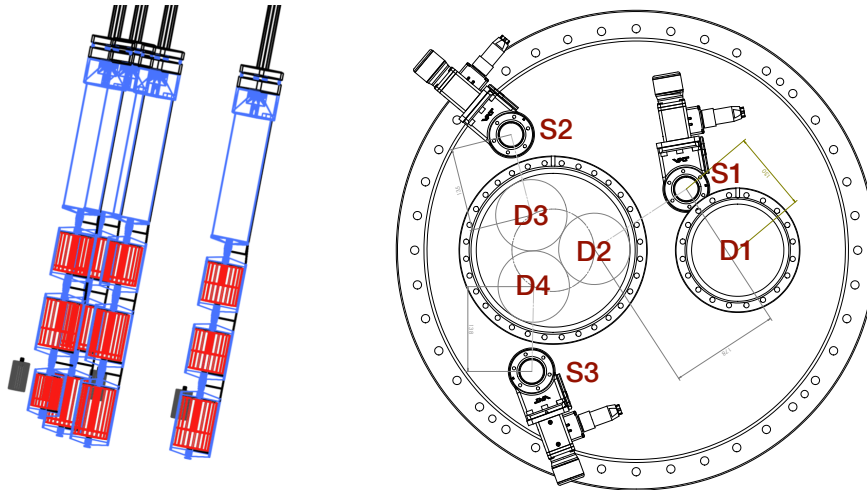
(a) Side view of the detector array. Shown in red are the detectors with their different heights, shown in grey are the three calibration sources with their absorbers.

(b) Technical drawing of the cluster flange which defines the horizontal (xy) positions of the four detector strings D1-4 and three calibration sources S1-3.

Figure 5.2: Configuration of detectors and calibration sources used to simulated GERDA's phase I.

	String 1	String 2	String 3	String 4
Name	GTF 42	RG 1	RG 2	RG 3
Height [mm]	82.5	84	84	81
Mass [g]	2467	2110	2166	2087
Name	GTF 44	ANG 4	ANG 3	GTF 112
Height [mm]	84	100	93	100
Mass [g]	2465	2372	2391	2965
Name	GTF 110	ANG 2	ANG 5	ANG 1
Height [mm]	105	107	105	68
Mass [g]	3046	2833	2746	958

Table 5.1: Configuration of the simulated detector array. The string numbering is explained in the text and shown in figure 5.2(b). The distance between each detector in one string is 6 cm. The detectors are named according to the following convention: ANG: former Heidelberg-Moscow detectors, enriched in ^{76}Ge; RG: former IGEX detectors, enriched in ^{76}Ge; GTF: Genius Test Facility detectors, natural Ge. Given also the height and mass of the detectors [93].

izontal (xy) position is defined by the cluster flange shown in figure 5.2(b). The cluster flanges closes the cryostat on its top and has several openings for the detector strings and the calibration sources. The implementation of the positions of detector strings and calibration sources with the change to the commissioning lock (see section 4.2) was part of this work. Since the dimensions of the detectors, especially their height, are not the same, their position in the detector array is significant. Owing that the final positioning was not decided at the start of this work, a somewhat arbitrary array was chosen where detectors with similar heights are placed at the same position within the strings (layer). The exact configuration including all relevant parameters of the detectors are listed in table 5.1. The space between the detectors in one string is 6 cm. The strings in the three string arm are spaced on a equilateral triangle with a side length of 108 mm. The detectors are aligned to the top edge of the top detector in each string. A side view of the detector array as it is implemented in the MCS is shown in figure 5.2(a); the different dimensions of the detectors are clearly visible.

Since the calibration system was under investigation, its geometry changes a lot in the different simulations. Details will be given in the different sections. In general, the whole decay chain of the used radioactive source was simulated. The different isotopes in the decay chain have half-lives up to 3.7 days. This was not realistically included in the MCS but an arbitrary value of 100 μs was chosen to avoid summation of photons from different isotopes which would not exist in reality. If not mentioned differently, a total of 10^8 photons were simulated in all sources included in the simulation together. The source encapsulation and intended composition was included.

Considering that the energy spectra obtained by MCS show infinitely good resolution, they have to be smeared with realistic values. For this purpose, test data taken in May 2009 with a ^{60}Co and a ^{232}Th source were used [94]. Table 5.2 shows the obtained energy resolution at different energies for one detector. A linear function was fitted to these values as shown in figure 5.3 and folded into the MCS spectra. Owing to the different physics origin compared to full energy peaks (FEP), the single-escape peak (SEP) is broader than the other peaks: As explained in section 3.1, the SEP is the result of pair production with

Energy [keV]	511	586	911	969	1173	1333	2104	2615
σ [keV]	1.73	1.35	1.42	1.50	1.47	1.51	2.18	1.78

Table 5.2: Energy resolution for different energies taken with a ^{60}Co and a ^{228}Th source and one of the GERDA phase I detectors before the commisioning phase by the MPI-Hd group [94].

the produced positron annihilating and one of the resulting photons escaping. Due to the small but finite momentum of the positron-electron pair immediately before annihilation, the two photons have slightly different energies. This leads to a broadening of the resulting peak. No broadening of the DEP is observed, because in the case, both photons escape, thus always taking the full 1.022 MeV with them [69]. Therefore, the actual fit result was used in the 1σ region around the SEP to smear the MCS.

5.2 Comparison of Different Source Types

The Q-value of ^{76}Ge is at 2039.006(50) keV [59], and the 5 keV region around this value was chosen as the region of interest (ROI). Therefore, several lines in the energy range up to 2.5 MeV are necessary for the energy calibration and there should be at least one line close to the Q-value. A sample of single-site events (SSE), which is necessary for pulse shape calibration, can be achieved from a clear double escape peak (DEP). This requires a strong full energy peak (FEP) well above 2 MeV, such that the probability of pair production with both annihilation photons escaping is sufficiently high. A peak to background ratio of at least 2:1 was considered sufficient in this case. A full energy peak close to the DEP would be an asset because it would allow the comparison of a sample of SSE and a sample of multi-site events (MSE) without the influence of the energy dependent energy resolution of the detectors. Since the source will stay in the cryostat, a half life of at least several months is required.

Possible emission of α particles by the source is an important issue because they might produce neutrons in (α,n) reactions. The probability of (α,n) reactions depends on the energy of the α particles and the threshold energy of the material close to the source. Neu-
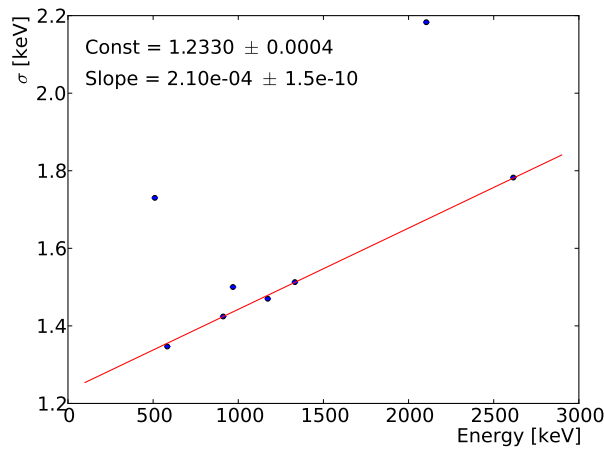
Figure 5.3: Linear fit to the energy resolution for different energies taken with a ^{60}Co and a ^{228}Th source and one of the GERDA phase I detectors.

(a) ^{56}Co.

(b) ^{228}Th.

(c) ^{238}U.
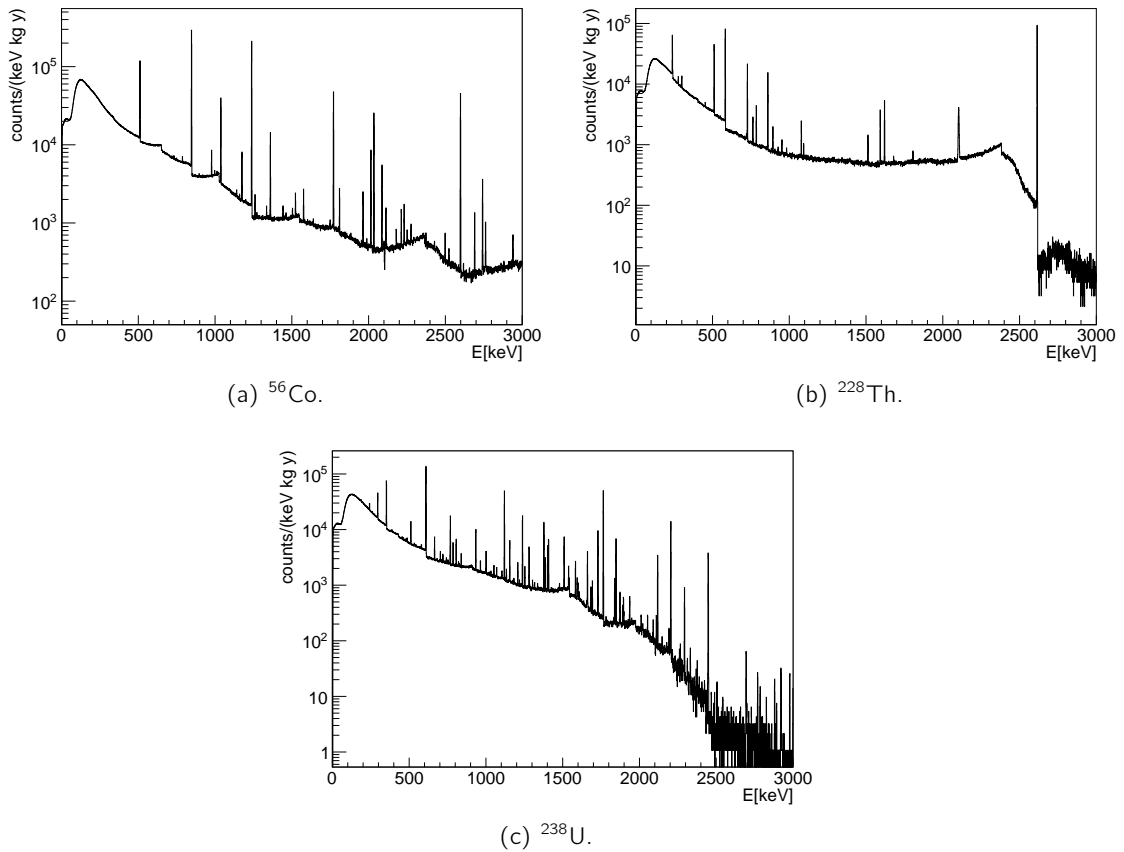
Figure 5.4: Comparison of different possible calibration sources. Shown is the simulated sum of all entries in all detectors normalized to a source activity of 3×20 kBq and the total detector mass. All spectra are folded with the expected energy resolution.

trons can contribute to the background in the ROI due to scattering or neutron capture, the latter resulting in radioactive isotopes which might emit photons with an energy close to the ROI.

Taking these requirements into account, three possible calibration sources are considered: ^{56}Co, ^{228}Th and ^{238}U; table 5.3 summarizes their relevant characteristics. These sources were studied in Monte Carlo simulations, positioned as explained in section 5.4. The simulations were necessary to investigate the background level at each peak which is the sum of Compton background as well as energy deposition of photons which already scattered in the liquid argon. This might have an impact on the resulting peak to background ratio which is especially important for the DEP. Figure 5.4 shows the sum of the energy spectra of all detectors for the different sources normalized to the same activity, time and detector mass.

All three sources have several well pronounced lines in the relevant energy region. The advantage of ^{56}Co is that it is not emitting any α particles. Furthermore, with $E_\gamma = 2.035$ MeV ^{56}Co has a FEP very close but still distinguishable from the Q-value. The disadvantages of ^{56}Co is its short half life of $T_{1/2} = 77$ d and no DEP with sufficient statistics for a pulse shape calibration.

The next source considered is ^{238}U with a half life of $T_{1/2} = 4 \times 10^9$ y and a FEP close to

the Q-value at $E_\gamma = 2.204$ MeV. Unfortunately, it also does not show a DEP with sufficient statistics. Moreover, it is emitting α particles with energies up to $E_\alpha = 8.8$ MeV and will therefore most likely also emit neutrons.

The last source considered is ^{228}Th with a half life of $T_{1/2} = 1.9$ y and a FEP at $E_\gamma = 2.104$ MeV close to the Q-value. Furthermore, it shows a reasonable DEP at $E_{\mathrm{DEP}} = 1.593$ MeV with a peak to background ratio of 2:1 coming from the ^{208}Tl line at $E_{\mathrm{Tl}} = 2.615$ MeV. With the ^{212}Bi line at $E_{\mathrm{Bi}} = 1.621$ MeV there is a FEP very close to the DEP which makes it ideal for pulse shape calibration. The disadvantage of the source is that it emits α particles which can produce neutrons in the surrounding material. The implications will be discussed in section 5.6. Nonetheless, it is the best option for the experiment and will therefore be used for the actual calibration measurements.

5.3   Number of Sources

One major restriction for the calibration system is the physically available space on top of the cryostat. Figure 5.5 shows the situation in the clean room above the cryostat. As mentioned in section 4.3, one limitation is the cluster flange, a DN630 CF, with the two flanges for the detectors: One DN250 CF housing three detector strings and one DN160 CF housing one detector string (see figure 5.2(b)). Both have a shutter right above the cluster flange. One big flange for the detectors is not possible because of limitations from the detector lowering system. See section 4.2 for details. Between both detector flanges, the space was minimized in order to keep the detector array as compact as possible.

The smallest usable flange for the calibration sources is a DN40 CF giving first limits for the smallest possible distance between source and detector. Above those flanges are the pipes housing the detectors and calibration sources, which have to be accessible. In figure 5.5, just the one string arm is in use. Since the space in the glove box is needed for the detector handling, only the space between glove box and cluster flange is available for the calibration system. This leads to a maximum height of 27.4 cm. Furthermore, the width is limited, since the systems should not interfere with the detector handling in the glove box, and because of the space needed for the shutter of the detector strings as well as those included for the calibration system. The latter are also right above the cluster flange. Consequently, fewer number of sources are preferred.

To determine the minimum number of sources needed for a successful calibration, MCS with one, two and three sources were performed with the sources positioned according to figure 5.6. Note that in case of one calibration source the detectors in the 3-string arm are rotated to achieve the most uniform irradiation possible. Figure 5.7 shows the horizontal

	^{56}Co	^{228}Th	^{238}U
$T_{1/2}$	77 d	1.9 y	4×10^9 y
$E_{\gamma,\mathrm{max}}$ [MeV]	3.5	2.6	2.4
E_γ closest to Q value [MeV]	2.035	2.104	2.204
$E_{\alpha,\mathrm{max}}$ [MeV]	-	7.7	8.8

Table 5.3: Relevant characteristics for the three possible calibration sources. E_{max} gives the maximum energy photons are emitted with. It is also indicated if the sources emits any α particles.
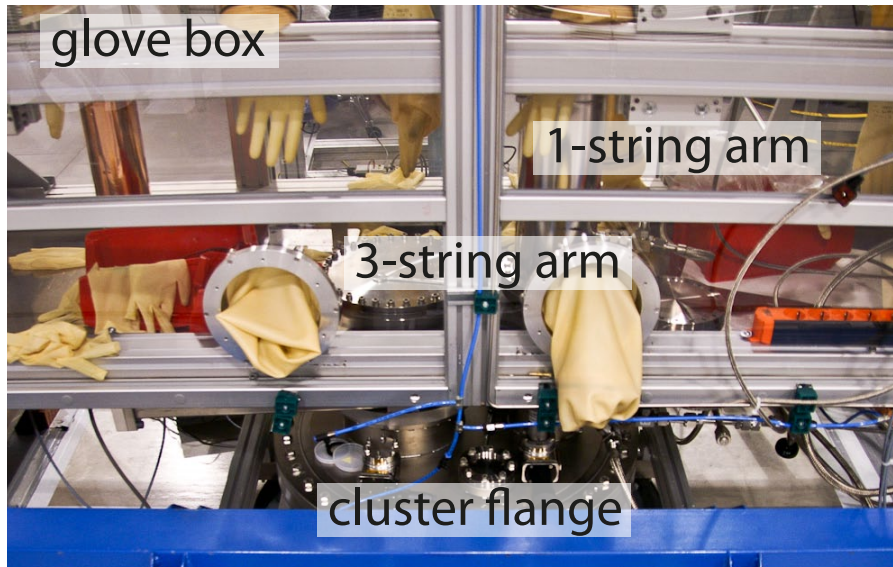
Figure 5.5: Situation in the clean room above the cryostat. Since the space in the glove box is needed for the detector handling, only the space between glove box and cluster flange was available for the calibration system.

(a) 1 Source   (b) 2 Sources   (c) 3 Sources
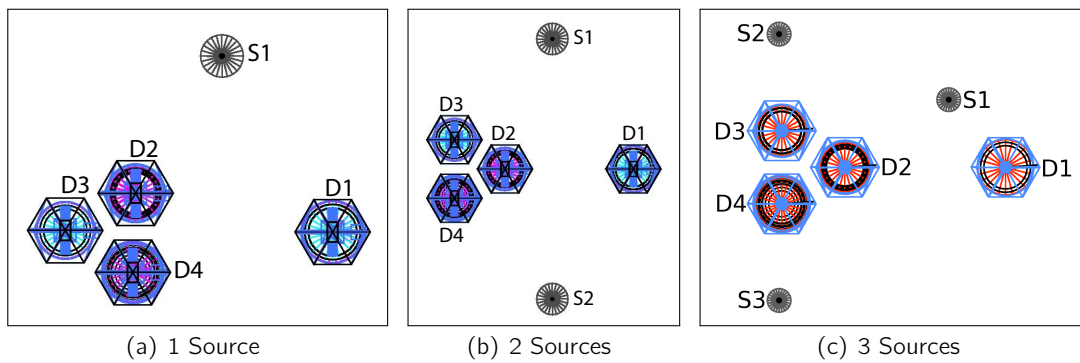
Figure 5.6: Different geometries with one, two and three calibration sources to determine the minimum number needed for a successful calibration. Note that in case of one calibration source the detectors in the 3-string arm are rotated to achieve the most uniform irradiation possible.

(a) 1 source   (b) 2 sources   (c) 3 sources
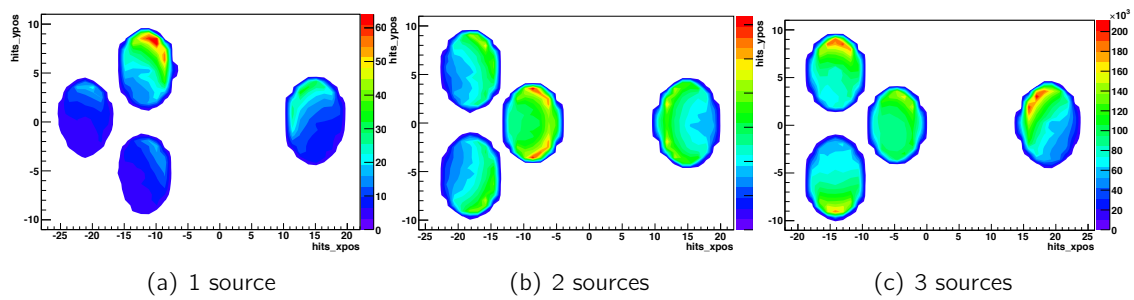
Figure 5.7: Horizontal (xy) distribution of energy depositions in the detector array for 1, 2 and 3 calibration sources showing the shielding effect of the detectors themselves and the LAr.

(xy) distribution of energy depositions (hits) in the detector array for the three different cases. The results show two effects: The first one is the self-shielding effect of the detectors which is most prominent in case of one calibration source (see figure 5.7(a)). The second one is the gamma attenuation of the LAr which becomes already obvious in the differences between detector strings D1 and D2 in case of two calibration sources (see figure 5.7(b)). Because of the slightly smaller distance from the sources to string D2 it shows more hits than D1. In case of three calibration sources the hits distribution is smoothest.

The only available space for a fourth calibration system is close to D1 and next to S3. Since the expected improvements are minimal, it was not considered necessary. Therefore, the configuration shown in figure 5.7(c) with three calibration sources was realized in the experiment.

5.4   Positioning

With the number of sources set to be three, there was very little flexibility in the xy positioning due to the space constrains described in section 5.3. The sources were positioned as close as possible to the detector strings under consideration of the required space by flanges, shutters and lowering systems for the detectors as well as the calibration sources. The result is an average distance of 16 cm between source and detector and the exact geometry can be found in figure 5.2(b).

The determination of the best (vertical) z positions for the sources is non-trivial because of the different heights of the detectors (see table 5.1), the self-shielding of the detectors and an absorber. The latter is necessary to shield the sources in their parking position as will be explained in section 5.6. Since it might effect the optimum positions of the sources, it was implemented in the Monte Carlo simulations used to determine them.

Each source was simulated separately to be able to determine its contribution in each detector at each position. The complete ^{228}Th chain was simulated with 3×10^7 decays per source and position. The sources were positioned from -20 mm down to -410 mm in steps of 10 mm. The zero position is the top edge of the top detector which is the same in each string. The complete string has a length of about 400 mm.

To determine the optimum position for each source, only the relevant detector strings were taken into account: For source S1 string D1 was considered, for S2 the strings D2 and D3 and for source S3 the strings D2 and D4 (for the labels see figure 5.2). The contribution of the other sources to a particular string was found to be insignificant. The single escape peak (SEP) of ^{208}Tl was chosen as reference peak because with an energy of $E = 2.104$ MeV it is closest to the Q-value. Figure 5.8 shows the number of counts in the SEP in each detector for the different z position.

It was expected that the calibration sources have to be positioned at either two or three different z positions to get sufficient statistics in each detector. In case of two z positions, the sources would be roughly between the detectors in each string; in case of three z positions, they would be roughly in the middle of each detector. Thus, it was first investigated, if one of theses cases leads to sufficient statistics in all detectors and where the corresponding ideal source position would be.

S1	S2	S2	D1	D2	D3	D4	S1	S2	S3
50	50	50	0-83	0-84	0-84	0-84			
							135	130	130
210	215	215	143-227	144-244	144-237	144-244			
							280	290	320
360	380	365	287-392	304-411	297-402	304-372			
3 Positions			Detector positions				2 Positions		

Table 5.4: Optimum vertical position $-z$ in [mm] relative to the top edge of the top detector of the calibration sources S1, S2 and S3 (see figure 5.2) for 2 and 3 vertical calibration positions per source. In the middle also the detector position in [mm] (top edge - bottom edge). Between each detector is a space of 60 mm.

For this purpose, a Gaussian was fitted to the count rates in each detector for the different z positions (see figure 5.8). The peak positions of the Gaussians were used for the 3 position case, the intersection points for the 2 position case. Since the sources S2 and S3 have to calibrate two detector strings, the mean value between both strings was chosen. The only exception is the bottom detector in string D4 (ANG 1): Since it is by far the smallest detector its optimum calibration position was weighted double when calculating the best position for source S3. The results are shown in table 5.4 together with the positions of the detectors.

As can be seen, the ideal positions are below the middle point of the detectors in the 3 position case and below the middle point between the detectors in the 2 position case. This was expected due to the shielding of the absorber at the bottom of the source. The exact amount was found to be -20 ± 3 mm with two exceptions. The first one is ANG 1 in the 2 position case: Since it is by far the smallest detector, it was found to be better to position the source at its middle point. The second exception is the top position in the 3 position case. Here, the best position was found to be -7 ± 3 mm below the middle point of the detectors. There is no obvious explanation for that. Nonetheless, these offsets can be used as a guideline for the source positioning for other detector array configurations.

To compare both cases, the total number of counts in the SEP for each detector was calculated using the optimum positions determined above and normalizing to a source activity of 20 kBq per source and a calibration time of 1800 s per position. The choice of these values will be explained in section 5.5. For each detector, the contribution of all three calibration sources was taken into account. The goal was to reach at least 1000 counts in the SEP in each detector. Table 5.5 shows the results for both cases. The different count rates per detector can be explained by their different masses (see figure 5.8 where the normalization was done). Since two calibration positions in the z-direction are sufficient and more time efficient, these positions will be used for the actual calibration.

5.5 Activity

In the next step the minimum source strength necessary to get sufficient statistics in all detectors has to be determined. Sufficient is defined in this case as a minimum of 1000 counts in the peak as well as a peak to background ratio of $2:1$. These values should be reached using the lowest possible activity within a total calibration run time of less than 4 h including the movement of the sources. As a conservative estimate, a total moving time of 1 h was

(a) String D1

(b) String D2

(c) String D3

(d) String D4
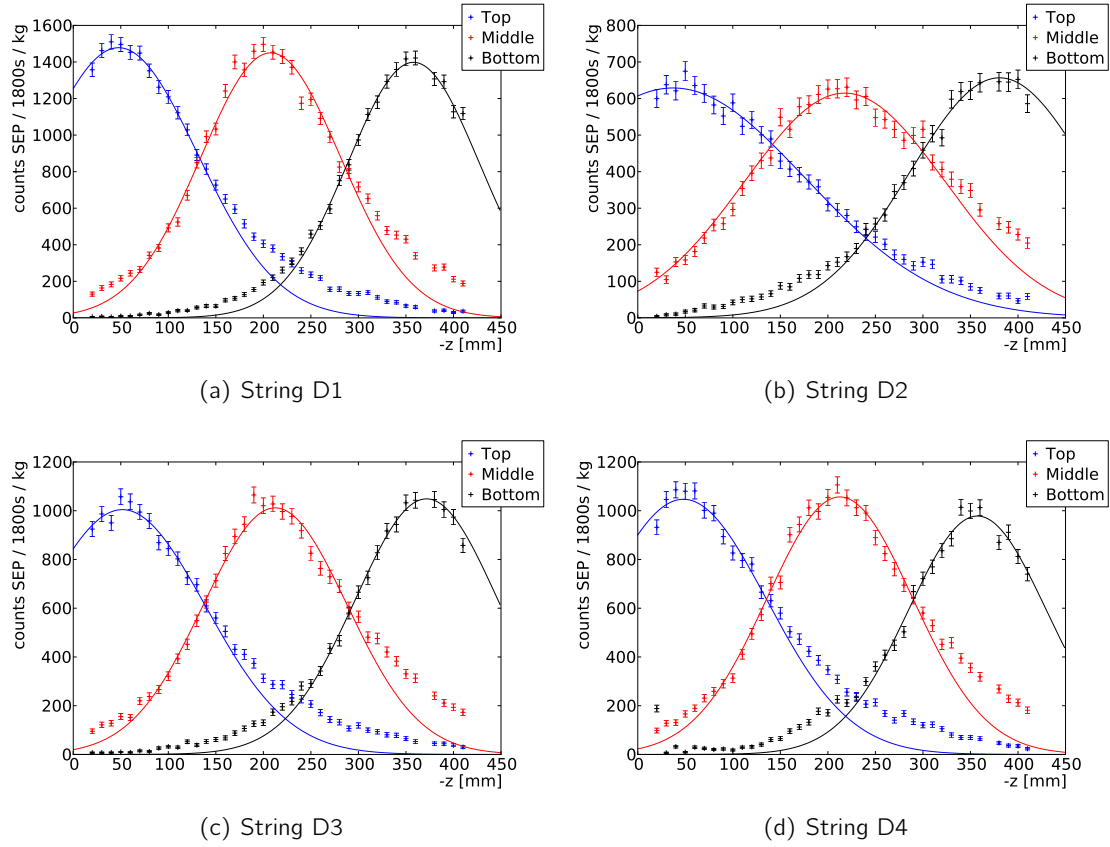
Figure 5.8: Number of counts in the SEP in each detector normalized to a source strength of 20 kBq, 1800 s calibration time and the detector mass. Gaussian functions, which describe the bulk of the data very well, were fitted to determine their peaks as positions with maximum count rate (3 calibration positions per source) as well as their intersections as optimum positions between two detectors (2 calibration positions).

assumed for lowering the source 5-6 m from their parking position on top of the cryostat down to their two calibration positions and lifting them up again. This leaves in total 3 h for the calibration itself meaning 1.5 h for each position. Since the half life of ^{228}Th is 1.9 y and the sources are left inside the experimental setup for the full phase I ($2-3$ y including ~ 1 y of commissioning) a calibration time of 30 min per position was assumed as a conservative estimate to ensure sufficient statistics also towards the end of phase I.

To estimate the necessary source activity the results of Monte Carlo simulations with each calibration source in its best positions were combined, therefore simulating a full calibration

	D1	D2	D3	D4	D1	D2	D3	D4
top detector	5100	4000	4200	3800	2800	2600	2600	2200
middle detector	5300	4700	5100	5900	4400	4000	4100	4300
bottom detector	5500	4300	4800	1600	2800	2300	2500	1100
		3 Positions				2 Positions		

Table 5.5: Number of counts in SEP with $A = 20$ kBq per source in [counts/1800s] in the different detectors for 3 or 2 calibration positions as given in table 5.4.

(a) Total energy spectrum

(b) Zoom into the region of interest
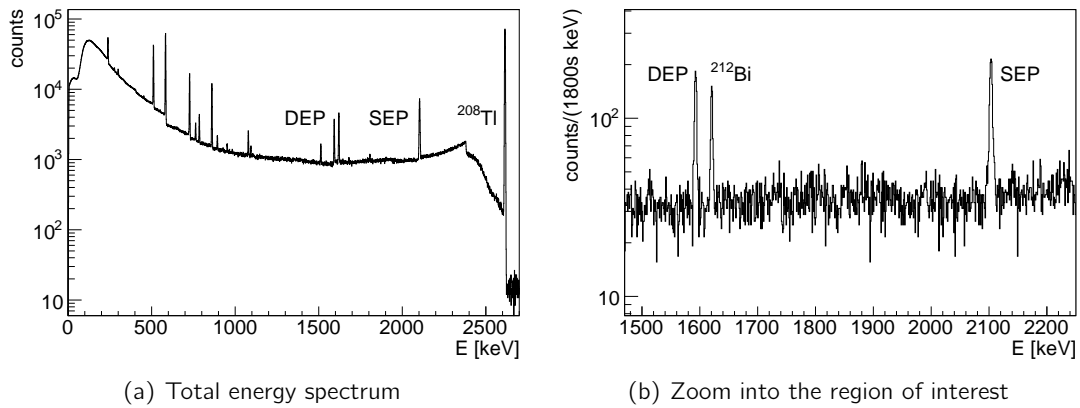
Figure 5.9: Simulated energy spectrum of the smallest detector in the array after a calibration run with 3 sources with an activity of 20 kBq each, 2 different *z* positions and a run time of 30 min per position.

run. Again, the SEP was chosen as the reference peak and the number of counts as well as the peak to background ratio was determined for each detector. Since the third detector in string D4 (ANG 1) has by far the smallest count rate, it was used as a reference.

A simulation of 3×10^7 decays per calibration source and position leads to 950 counts in the SEP in ANG 1 with a peak to background ratio of 2.4:1. Scaling these numbers up to 1000 counts was considered as sufficient, leading together with the calibration time of 30 min to a minimum activity of 17.6 ± 0.6 kBq. Therefore it was decided to use sources with an activity of $A = 20$ kBq for phase I. Figure 5.9 shows the energy spectrum of the smallest detector corresponding to this configuration.

## 5.6 Background from Calibration Sources

Since a low background environment is crucial for the success of the experiment, an estimate of the background contribution in the ROI from the calibration system in the parking position is essential. In this position, the sources are shielded by a combination of liquid and gaseous argon. Because of its very low density, the gas will not be considered in the following. Several isotopes in the ^{228}Th chain decay via α decay; hence both will be considered, the emitted γ's and the neutrons produced via (α,n) reactions in the surrounding material. The background contribution from neutrons during physics runs as well as calibration runs will be determined.

Originally, it was planned to place the detectors a little below the middle of the cryostat because more background is expected to come from the top than from the bottom due to cosmic rays. In this position, about 3.5 m of LAr shield the detectors from radiation coming from above and with a length of the detector array of about 0.4 m, there are 2.5 m of LAr shielding at the bottom. Unfortunately, as mentioned in section 4.3, one of the calibration sources fell into the cryostat in an accident. Owing that there is no easy way to remove the source, the possibility will be discussed to leave the source in the cryostat which strongly depends on the outcome of the following background study. Since it has to be assumed that the LAr is the only shielding between the bottom source and the detectors, it was decided to lift up the detectors by 0.5 m, hereinafter referred to as "current position". For a conservative background estimate, three calibration sources with an activity of 20 kBq each

will be assumed; for the source at the bottom of the cryostat, an activity of 30 kBq will be used. As shown in section 5.7, the current activities at the start of phase I are significantly lower.

γ Background

In case of the γ background, two methods were used and compared. The first one is a combination of an analytical estimate with Monte Carlo simulations, the second one is a pure Monte Carlo simulation with the sources in their parking position. The latter are very CPU consuming. Therefore the first method was used for faster results to be able to determine the necessary shielding. Owing to the larger uncertainties of the method which will be explained later, it was tried to be very conservative. Afterwards, the full MCS were used to verify the results. Since in the full MCS a shielding of 3.4 m of LAr was used, corresponding to the original detector position, this will be used to compare both methods. Since the semi-analytical method can be easily scaled to other shielding thicknesses, it will be used to determine the background contribution from the bottom source with the detectors in its original position. Afterwards, the background from top and bottom source in the current position will be determined, again with the semi-analytical method.

In the semi-analytical method, MCS are just used for the last 1 m of LAr. The flux at this position is estimated using linear attenuation $\phi = \phi_0 \times e^{-d/l}$ (see section 3.1) with ϕ_0 being the initial flux, d the thickness of the absorbing material, $l = \frac{1}{\mu \rho}$ the mean free path, μ the mass attenuation coefficient and $\rho = 1.394\,\text{g/cm}^3$ the density of liquid argon. The 2.6 MeV line from ^{208}Tl is the only line above the Q-value and therefore the only possible source for background in the ROI. Unfortunately, the NIST database just provides values for the mass attenuation coefficient for 2.044 MeV and 3.0 MeV photons. Therefore, the value for the 2.6 MeV photons had to be interpolated from those values. A mass attenuation coefficient of $\mu = 0.0352\,\text{cm}^2/\text{g}$ was found [74], resulting in a mean free path of $l_{\text{NIST}} = 20.4 \pm 0.4\,\text{cm}$.

To confirm this result, MCS were used to determine the mean free path of 2.6 MeV photons. A beam of 10^8 γ's directed to one detector was used with varying distances between source and detector. Fitting an exponential decay to the total counts in the detector over
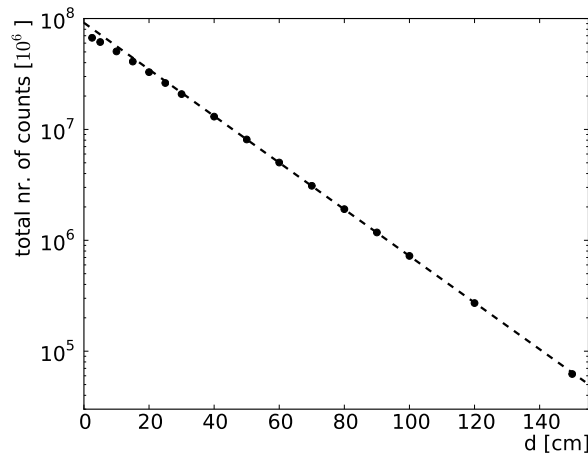

Figure 5.10: Total number of counts in one detector for different distances to the source. An exponential decay was fitted to the data points to determine the mean free path of 2.6 MeV γ's in LAr.

distance lead to a mean free path of $l_{\text{MCS}} = 20.65 \pm 0.01$ cm. The corresponding plot can be found in figure 5.10. The small deviations of fit and data for small distances are due to geometrical effects. With this method, the mean free path could be determined with much higher precision than from the NIST database. Furthermore, the used geometry reflects the actual situation in the cryostat as it will be investigated in the following. Thus, the mean free path determined by MCS will be used in the following.

For the initial flux, the number of decays in one year from 3 calibration sources with $A = 20$ kBq each was used and then taken into account that due to the branching ratio just 36% of these decays end with an emission of a 2.6 MeV γ. The other existing channel does not emit any γ's with energies above 2 MeV. Since the source radiates isotropically but the detector array covers just a small solid angle, the relevant flux reduces accordingly. For simplicity, the distance between the outermost detectors was used and a circle with half this distance assumed to be the area covered by the detectors. The reduction of the flux can than be calculated using

$$\frac{\Omega_{\text{sphere}}}{\Omega_{\text{det}}} = \frac{4 \cdot \pi}{\pi \cdot r_{\text{det}}^2 / d^2} = 2055 \tag{5.1}$$

with a radius of $r_{\text{det}} \simeq 15$ cm and a distance $d = 3.4$ m between source and detector in the original detector position. This reduces the original flux to $\phi_0 = 3.3 \times 10^8$ γ/y. To estimate the flux one meter above the detector array, linear attenuation is used with a thickness of $d = 2.4$ m, leading to $\phi(-2.4$ m$) = 3.0 \times 10^3$ γ/y.

For a conservative estimate of the background in the ROI, a photon beam directed to the center of one of the detector strings was simulated for the last meter of LAr. Figure 5.2(b) shows the xy position of the detector strings and the calibration sources. S1 pointed to D1, S2 to D2 and S3 to D4. In total, 4.8×10^9 γ's with an energy of 2.6 MeV were simulated. These simulations result in a total of 8.4×10^4 events in the ROI. Rescaling to the initial flux $\phi(-2.4$ m$)$ and using a total mass of 17.7 kg, a background contribution of $(2.9 \pm 0.1(\text{stat}) \pm 0.3(\text{sys})) \times 10^{-4}$ counts/(keV· kg· y) was obtained. Such a level is tolerable for phase I with a background goal of 10^{-2} counts/(keV·kg·y). However, since other parts of the experiment, especially the cryostat, will contribute to the background as well, further shielding is preferred and will be discussed later.

In the full MCS three calibration sources were placed 3.4 m above the detector array. To acquire more statistics in a shorter time, more detector strings were included in the simulations: Figure 5.11 shows all possible positions with the final lock system, which was suppose to replace the existing lock in phase II (see section 4.2). Three of these positions were planned to be used for the calibration sources, leaving 16 possible positions for detectors. All of these positions were filled with strings of three detectors each, leading to a total of 48 detectors with a total mass of 76.8 kg. Again, just 2.6 MeV γ's are simulated since they are the only possible source for background in the ROI. Photons emitted in the top 2π hemisphere will loose too much energy on their way to the detectors if they reach it at all and can be ignored. Therefore, just photons emitted in the lower 2π hemisphere were simulated.

The simulation of 1.05×10^{12} γ's lead to a total 19 events in a 400 keV ROI from 1839-2239 keV. This large region was necessary due to the low statistics. The energy spectrum in the full energy range as well as the ROI is shown in figure 5.12. This corresponds to a background contribution of $(1.98 \pm 0.62(\text{stat}) \pm 0.2(\text{sys})) \times 10^{-4}$ counts/(keV·kg·y). As expected, the semi-analytical approach shows the more conservative limit but both values
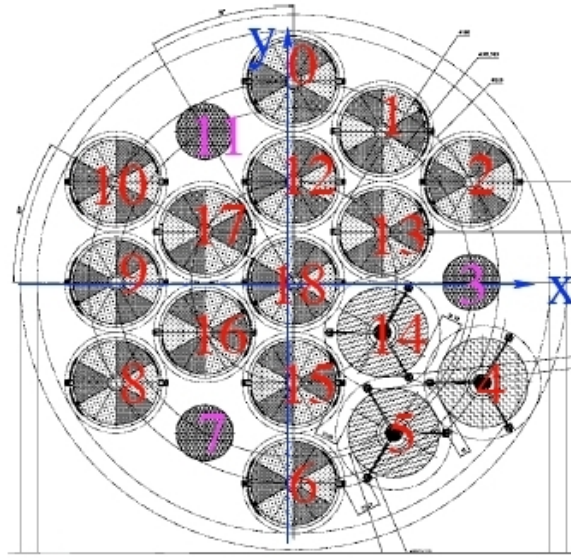
Figure 5.11: Possible positions with the final lock system which was suppose to replace the existing lock in phase II (see section 4.2). Positions 3, 7 and 11 are planned to be used for calibration sources, all other positions can be filled with detector strings. Strings with three detectors were used at each possible position for the full MCS to determine the gamma as well as the neutron background from the parking position.

agree within errors. This proves that the semi-analytical approach can be used to determine the background from the bottom source as well as for the different detector position.

In the original detector position, the bottom source is shielded by 2.5 m of LAr. The semi-analytical approach with this distance as well as an activity of 30 kBq led to a background contribution of $(2.1\pm0.1(\text{stat})\pm0.3(\text{sys}))\times10^{-2}$ counts/(keV·kg·y). This is already above the background goal for phase I of 10^{-2} counts/(keV·kg·y). Lifting the detectors by

(a) Full energy spectrum

(b) Energy spectrum in the ROI
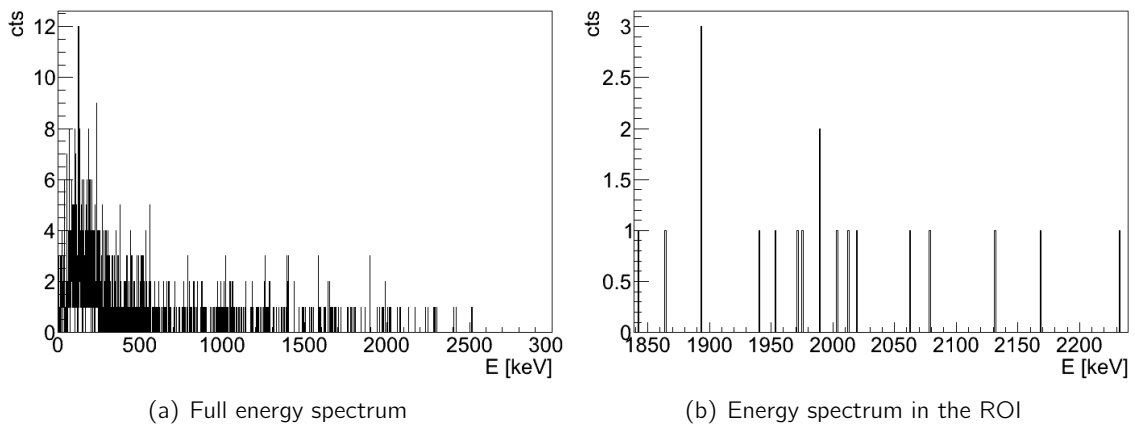
Figure 5.12: Energy deposition of 2.6 MeV γ's started 3.4 m above the detector array. A total of 1.05×10^{12} γ's were simulated in a 2π hemisphere which corresponds of the number of ^{228}Th decays in about 3 years.

0.5 m reduces the background to

$$B_\gamma^{\text{bottom}} = 1.3 \pm 0.1(\text{stat}) \pm 0.1(\text{sys})) \times 10^{-3} \text{ counts/(keV·kg·y)}. \quad (5.2)$$

This value is still relatively large and jeopardizes the phase I goal of the experiment. On the other hand the procedure to remove the source from the cryostat would be fairly long (minimum of half a year if the cryostat has to be emptied) and expensive. Additionally, the half life of 1.9 y reduces the background with time and the determined background estimate is rather conservative.

For a final decision if the source can stay in the cryostat, the larger background from the top sources due to the higher detector position has to be taken into account. Scaling to the new values leads to a background contribution of $2.6 \pm 0.1(\text{stat}) \pm 0.3(\text{sys})) \times 10^{-3}$ counts/(keV·kg·y). Therefore, further shielding becomes mandatory.

The possible shielding material needs to be as radio-pure as possible with very good absorption properties and it has to be machinable. The material fulfilling these requirements best is tantalum with $\mu(2.6\,\text{MeV}) = 0.04\,\text{cm}^2/\text{g}$, $\rho = 16.7\,\text{g/cm}^3$ and a natural radioactivity of about 50 mBq/kg from ^{182}Ta with a half life of 114 d. Details about the study of possible shielding materials can be found in section 6.1. Owing to the space issues described in section 5.6, the maximum possible absorber is a cylinder with a height of 6 cm which reduces the background to

$$B_\gamma^{\text{top}} = 4.3 \pm 0.1(\text{stat}) \pm 0.4(\text{sys})) \times 10^{-5} \text{ counts/(keV·kg·y)}. \quad (5.3)$$

which is well below the background goal for GERDA phase I. Combining both contributions, from the sources on top and the one on the bottom, lead to a background of

$$\boxed{B_\gamma^{\text{total}} = 1.4 \pm 0.1(\text{stat}) \pm 0.1(\text{sys})) \times 10^{-3} \text{ counts/(keV·kg·y)}.} \quad (5.4)$$

dominated by the contribution of the bottom source. As already mentioned, this value is of a critical level. Nonetheless, it was considered more important to start the experiment rather soon and decided that this background, which will decay away with time, is still at an acceptable level.

Neutron background

Neutrons from (α,n) reactions in the calibration source can contribute to the background in two different ways: By $(\text{n,n}'\gamma)$ inelastic scattering of fast neutrons in the surrounding materials, especially in argon, and due to neutron capture resulting in radioactive isotopes emitting photons with an energy close to the ROI. Elastic scattering is in this case not important as can be seen in the following estimate of the maximum energy transferred to a germanium nucleus by elastic scattering of a neutron. A maximum neutron energy of 8 MeV can be assumed as will be shown later (see e.g. figure 5.13) and therefore the nonrelativisic case can be used. The maximum energy will be transferred in a head-on collision, leading to a one dimensional problem. Calculating in units of the neutron mass, i.e. $m_n = 1$, the mass of the nucleus is equivalent to the atomic mass number of germanium $A = 72.63$. Energy and momentum conservation than leads to

$$E_{\text{transfer}}^{\text{elastic}} = \frac{(A-1)^2}{(A+1)^2} = 430 \text{ keV}. \quad (5.5)$$

(a) Commercial   (b) Custom
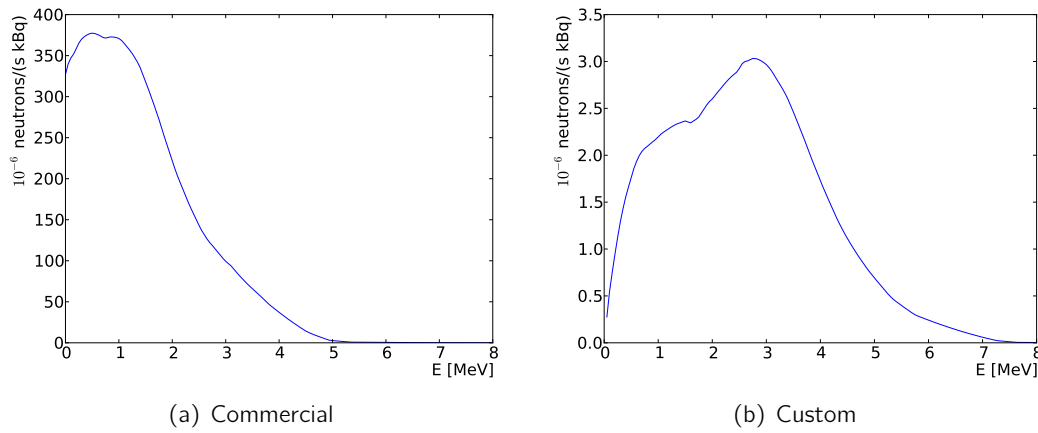
Figure 5.13: Neutron spectrum from (α,n) reactions of ^{228}Th embedded in a ceramic (commercial) or ThO_2 coated on gold (custom). Data provided by Michal Tarka.

Typical quenching factors of nuclear recoil energy into the equivalent of gamma energies lie in the order of 0.3. Thus, the maximum energy transferred in an elastic scattering event will be detected as a signal of about 130 keV. This is far below the Q-value of 2039 keV and will therefore not be considered in the following.

For the inelastic scattering, the contribution from the parking position is most important. For the case of neutron capture, the calibration runs are also important to consider, since isotopes close or in the detectors might be activated. Therefore Monte Carlo simulations for both cases were performed.

^{228}Th emits α's in an energy range up to 7.7 MeV. Commercially available sources are usually embedded into a ceramic of unknown composition. One possibility is $NaAlSiO_2$ where Na and Al dominate the neutron production by (α,n) reactions. The corresponding spectrum was determined using SOURCES4A [95] (see figure 5.13.), and a neutron production rate of 2×10^{-2} n/s/kBq was found [96, 97]. MCS with the sources in parking position were run to determine the background contribution due to scattering. The simulation of 10^9 neutrons led to 330 counts in the energy region between [1950,2060] keV. This enlarged region of interest was chosen due to the small statistics, similar to the full MCS for the γ background discussed above. This results for 3 sources with an activity of 20 kBq each and above neutron rate in a background contribution of 1.78×10^{-3} counts/(keV·kg·y). The resulting energy spectrum can be found in figure 5.14(a).

This background contribution is rather large, taking into account the background goal for phase I with 10^{-2}counts/(keV·kg·y) and that also other components of the experiment will contribute to the total background observed. Furthermore, it is well above the background goal for phase II which is 10^{-3}counts/(keV·kg·y). Since neutrons are difficult to shield, other possibilities to reduce the neutron flux had to be investigated not just to ensure the aimed low background for phase I but also for future prospects.

A possible solution is to prevent (α,n) reactions in the source itself. Therefore, the ceramic has to be replaced by a material with higher activation energy. A good candidate is gold which can be coated with a ThO_2 in a newly developed process. Owing to the high (α,n) threshold of gold, the only reaction partners for the α's from ^{228}Th is oxygen, which
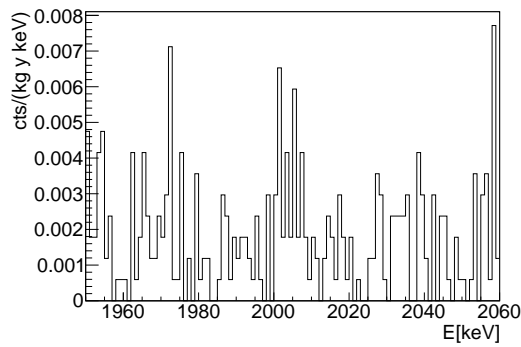
(a) Background contribution in the region of interest from commercial sources in parking position due to neutron scattering events.
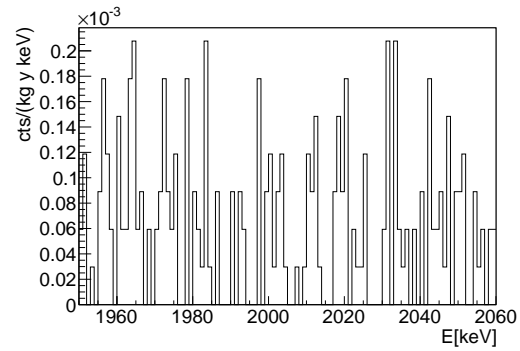
(b) Background contribution in the region of interest from custom sources in parking position due to neutron scattering events.
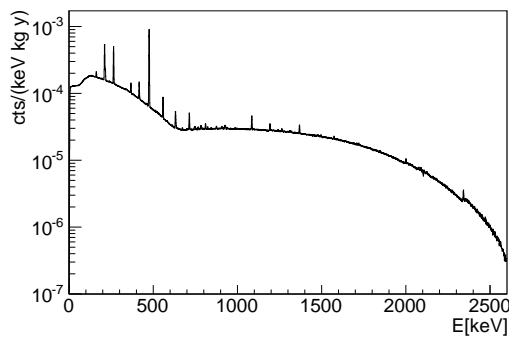
(c) Background contribution from the sources in parking position due to ^{77}Ge produced via neutron capture.
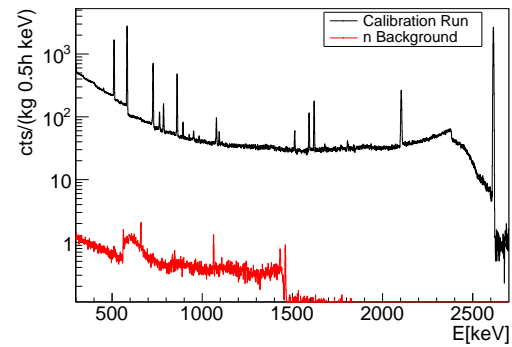
(d) Energy spectrum during a calibration run: The γ contribution (black) is shown together with the background from inelastic scattering of neutrons in the detectors (red).

Figure 5.14: Background contribution due to neutrons. The top row compare the contribution due to inelastic scattering events for two different neutron spectra: (a) A commercial ^{228}Th source embedded in a ceramic and (b) a custom ThO$_2$ solution coated on gold. Figure (c) shows the ^{77}Ge spectrum produced by neutron capture and (d) compares the γ and the neutron spectrum during a calibration run.

was taken into account in natural isotopic abundance in the calculations. Such a source with a low neutron yield will be referred to as 'custom' source in the following. The neutron spectrum was again determined using SOURCES4A and is shown in figure 5.13.

Measuring the neutron flux of a commercial as well as a custom made source showed, that the flux of the commercial source is with 4×10^{-3} n/(s·kBq) about a factor of 5 lower than expected from the estimate above, but still a factor of 4 larger than the flux of the custom source with 10^{-3} n/(s·kBq) [96, 97]. A possible explanation is the big uncertainty on the true composition of the ceramic. However, for an estimate of the background contribution due to neutrons, the exact spectrum has a minor influence and the actual flux is of main interest. Therefore, it was decided to just use simulations with the ThO$_2$ spectrum and scale the neutron flux in case of a commercial source in the following analysis.

Details on the neutron spectra, the development process as well as the corresponding measurements can be found in Michal Tarka's Ph.D. thesis [96] who was responsible for this part of the work. Monte Carlo Simulations and analysis necessary to determine the background

contribution due to neutrons were performed by the author.

As a first step, the background contribution from inelastic scattering of neutrons during the calibration run was inspected, again using MCS. A custom ^{228}Th source was assumed with a realistic neutron flux of 10^{-3} n/(s·kBq). As figure 5.14(d) shows, this background has no significant influence on the calibration spectrum. Therefore it will be ignored in the following.

For the estimation of the background due to inelastic neutron scattering, Monte Carlo simulations were performed with custom ^{228}Th sources in their parking position. The simulation of 10^9 neutrons resulted in 230 counts in the energy region between [1950,2060] keV. Again, a neutron flux of 10^{-3} n/(s·kBq) was assumed. The resulting spectrum can be found in figure 5.14(b) Using these numbers for three calibration sources with an activity of 20 kBq each, the following background contribution was found:

$$B_{\text{n, scatter}}^{\text{top}} = (6.2 \pm 0.4(\text{stat})) \times 10^{-5} \pm 20\%(\text{sys}) \text{ counts/(keV·kg·y)} \qquad (5.6)$$

It can be assumed that this background contribution does not significantly change within the range, the LAr level differ for the different detector positions since the LAr has minor shielding capabilities for neutrons. For the source at the bottom of the cryostat a neutron flux of 4×10^{-3} n/(s·kBq) was assumed since it is a commercial source, with an activity of 30 kBq. Rescaling leads to a background contribution of

$$B_{\text{n, scatter}}^{\text{bottom}} = (1.2 \pm 0.1(\text{stat})) \times 10^{-4} \pm 20\%(\text{sys}) \text{ counts/(keV·kg·y)}, \qquad (5.7)$$

which is well below the background goal for GERDA phase I.

In the next step the isotopes produced due to neutron capture reactions in all parts of the experiments were analyzed. Figure 5.15 shows the type and amount of produced isotopes in one year during calibration runs (figure 5.15(a)) as well as from the parking position (figure 5.15(b)), assuming one calibration run of 30 min per calibration position and week and three custom sources with an activity of 20 kBq each. Most of these isotopes do not emit photons nor β's with energies above 2 MeV and are thus no potential background candidates. The isotopes emitting photons or β's above 2 MeV are: ^{19}O, ^{28}Al, ^{41}Ar, ^{42}K, ^{49}Ca, ^{55}Cr, ^{56}Mn, ^{66}Cu and ^{77}Ge.

Concerning the photon emitters, those isotope were ignored, whose γ lines with energies above 2 MeV have intensities below 1 %. This reduces the possible background candidates to ^{49}Ca, ^{56}Mn and ^{77}Ge. ^{56}Mn is produced in several volumes, the highest production rates are the rock of the laboratory (6.2×10^4 isotopes/y) and the wall of the cryostat (2×10^4 nuclei/y), assuming again a neutron flux of $A_n = 10^{-3}$ n/(s·kBq) and a total activity of 3×20 kBq. Due to the continuous neutron flux from the sources in parking position and the short half-life of ^{56}Mn of 2.6 h, the production and decay rate are in equilibrium, leading to an activity in the rock of 2.8×10^{-4} Bq and in the wall of the cryostat of 8.9×10^{-5} Bq. A total of 1.2×10^9 decays were simulated in the cryostat wall. No events were found above 1.5 MeV leading to an upper limit on the background contribution of $< 1.5 \times 10^{-9}$ counts/(keV·kg·y), which is negligible. Since the water tank further shields the detectors from the radiation of the rock, its contribution can be ignored. The same argument holds for ^{49}Ca produced also in the rock of the laboratory with a very low production rate of 26 nuclei/y.

(a) Activated isotopes during calibration.   (b) Activated isotopes from source in parking position.
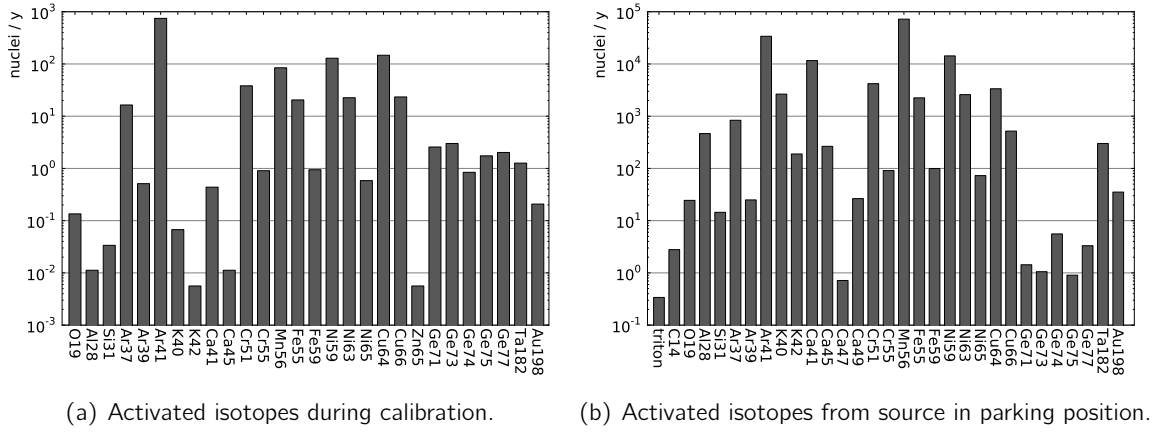
Figure 5.15: Neutron activated isotopes per year.

Due to the short stopping range of β's, only isotopes produced inside the cryostat were considered. This reduces the possible background candidates to ^{41}Ar and ^{77}Ge. ^{41}Ar, with a half life of 109 m and a β-decay Q-value of 2.5 MeV, is produced in the liquid argon with a production rate of 2.6×10^6 nuclei/y, assuming again a neutron flux of $A_n = 10^{-3}$ n/(s·kBq) and a total activity of 3×20 kBq. A total of 2.4×10^9 decays were simulated, isotropically distributed in the cryo liquid. To achieve reasonable statistics, the 200 keV interval around $Q_{\beta\beta}$ was chosen as ROI. A total of 48 counts were found, leading to a negligible background contribution of $(7.3 \pm 1.1) \times 10^{-8}$ counts/(keV·kg·y).

Therefore, only ^{77}Ge, produced in the detectors themselves, is potentially dangerous. After the neutron capture, the ^{77}Ge is highly excited and de-excites via a γ cascade into either the ground state or the metastable state ^{77m}Ge. The ground state β decays with $T_{1/2} = 11.3$ h, with endpoint energies up to 2.5 MeV and emits several gammas with energies up to 2.3 MeV. ^{77m}Ge decays with $T_{1/2} = 53$ s and a 19 % branching ratio into the ground state emitting a 160 keV γ. The other option with a 81 % branching ratio is a β decay with endpoint energies up to 2.9 MeV, emitting several gammas with energies up to 1.7 MeV. The total production rate of both, ^{77}Ge and ^{77m}Ge, is $A_{^{77}\text{Ge}} = 8.6$ nuclei/y, assumed to be equivalent to the decay rate. This includes both, the contribution from the sources in parking position as well as during calibration runs. Since the literature values of the corresponding cross sections vary significantly [98, 99, 100], the range of the background contribution was estimated using two simulations: One assuming that the total amount of the produced ^{77}Ge will decay from the ground state and the other one from the metastable state. In both cases a total of 2×10^7 decays were simulated, resulting in $B_{\text{ground}} = 9.7 \times 10^{-6}$ counts/(keV· kg· y) and $B_{\text{meta}} = 1.3 \times 10^{-5}$ counts/(keV· kg· y), both well below the GERDA background goals for both phases. As a conservative limit, B_{meta} will be used,:

$$B_{^{77}\text{Ge}}^{\text{top}} = (4.0 \pm 0.1(\text{stat})\,^{+0.3}_{-1.4}(\text{sys})\,) \times 10^{-5} \text{ counts/(keV·kg·y)} \qquad (5.8)$$

Rescaling again to a neutron flux for the bottom source of 4×10^{-3} n/(s·kBq) and an activity of 30 kBq leads to

$$B_{^{77}\text{Ge}}^{\text{bottom}} = (2.6 \pm 0.2(\text{stat})\,^{+0.6}_{-1.4}(\text{sys})\,) \times 10^{-5} \text{ counts/(keV·kg·y)} \qquad (5.9)$$

	γ	n scatter	^{77}Ge	Total
Top	4.28e-05	6.17e-05	4.01e-05	1.446e-04
Bottom	1.31e-03	1.23e-04	8.02e-05	1.513e-03
Total	1.35e-03	1.85e-04	1.20e-04	**1.658e-03**

Table 5.6: Different background contributions from the calibration sources. For the three calibration sources on top of the cryostat, $A_\gamma = 20$ kBq and $A_n = 10^{-3}$ n/s/kBq were considered per source. For the source, which fell in the cryostat, $A_\gamma = 30$ kBq and $A_n = 4 \times 10^{-3}$ n/s/kBq was used. All values are given in counts/(keV·kg·y).

Combining the different background contributions due to neutrons,

$$B_n^{\text{total}} = (3.0 \pm 0.1(\text{stat})\,^{+0.3}_{-0.4}(\text{sys})) \times 10^{-4}\ \text{counts/(keV·kg·y)} \tag{5.10}$$

was found, which is well below the background goals for GERDA phase I. The resulting energy spectrum can be found in figure 5.14(c). Summing up all background contributions from the calibration sources leads to

$$\boxed{B_{\text{total}} = (1.66 \pm 0.1(\text{stat})\,^{+0.13}_{-0.14}(\text{sys})) \times 10^{-3}\ \text{counts/(keV·kg·y)}.} \tag{5.11}$$

Again, this contribution is dominated by the γ background from the bottom source. It is of a critical level for phase I and already above the phase II limit. However, since the removal of the bottom source is complicated and this level acceptable for phase I, it was decided to continue the experiment. All different contributions are summarized in table 5.6.

5.7   Real Sources and Comparison with Data

For the GERDA calibration system, four different sources were available with a γ activity of 12.5 kBq, 17.5 kBq, 17.7 kBq and 51.1 kBq, respectively, at 31 March 2011. The relevant parameters can be found in table 5.7. To decide, which ones should be used, different parameters were compared: Necessary calibration time, achievable count rates in the detectors, background contribution as well as expected pile-up rate. After the installation in GERDA, calibration data taken with the crystals is compared to MCS results.

Real Source Activity

To determine the necessary calibration time for the different sources, MCS were used placing the sources at their optimum position. Each source was simulated separately to be able

	31 Mar 2011		01 Nov 2011		
Source	A_γ [kBq]	A_n [n/s]	A_γ [kBq]	A_n [n/s]	Type
SV 303	17.7	0.018	13.1	0.013	Custom
SV 304	12.5	0.013	9.3	0.009	Custom
SK 393	17.5	0.070	13.0	0.052	Commercial
TF 657	51.1	0.204	37.9	0.152	Commercial

Table 5.7: Relevant parameters for the different sources available for the GERDA calibration system. For custom sources, a neutron flux of 1×10^{-3} n/(s·kBq) was assumed and for commercial, a neutron flux of 4×10^{-3} n/(s·kBq). As reference dates, the middle of the commissioning phase (31 Mar 2011) and the start of phase I (01 Nov 2011) are used.

A_γ [kBq]	12.5, 17.5, 17.7				17.5, 12.5, 17.7			
	D1	D2	D3	D4	D1	D2	D3	D4
SEP [cts/1800s]	1832	1939	2085	1841	2414	2414	1759	1829
	2897	2977	3361	3697	3862	3163	2839	3630
	1883	1825	2008	950	2462	1874	1689	950
Cal time [s/pos]	1900				1900			

A_γ [kBq]	17.7, 17.5, 51.1			
	D1	D2	D3	D4
SEP [cts/1800s]	2773	3374	2594	4760
	4262	5038	4189	9443
	2850	3345	2630	2597
Cal time [s/pos]	700			

Table 5.8: Counts in the SEP in the different detectors after 30 min of calibration with different sources. Blue marks the detector with the highest number of counts while red marks the one with the lowest. The calibration time is estimated using the red marked detector scaled to 1000 cts which was assumed to be sufficient for a successful calibration. Reference date for all source activities is 31 March 2011.

to scale them according to the different source activities. A total of 3×10^7 decays were simulated per source. In the first step, the energy spectrum for each individual detector was normalized to 1 kBq and a calibration time of 30 min, leading to one spectrum per detector per source. This allows to scale the contribution of each source in one detector separately according to its strength before they were summed up. To be able to compare the count rates in the different detectors, the single-escape peak (SEP) of the ^{208}Tl line was again used as a reference. A Gaussian function above linear background was fitted to this line and then integrated over the 3σ region to determine the counts in the peak. Afterwards, the time was estimated to reach in all detectors a minimum of 1000 counts, which was assumed to be sufficient for a successful calibration.

Table 5.8 shows the results for three different source configurations. The activities of the sources are given for S1 to S3 in this order. For their exact position relative to the detector array, see figure 5.2. Marked in blue is the detector with the highest count rate, in red the one with the lowest in each case. The calibration time is estimated using the red marked detector scaled to 1000 cts. Note that the count rates are not normalized to the detector mass, since the goal is to calibrate them in a sufficient amount of time regardless of their size. Therefore, it is not surprising that the bottom detector in string D4 always shows the lowest or a very low count rate, since it is by far the smallest detector (see table 5.1). As previously discussed, 30 min of calibration time are considered acceptable at the beginning of phase I to ensure that calibrations can still be successfully performed at the end of the phase despite the half life of ^{228}Th of 1.9 y. 1900 s are just insignificantly longer from this perspective and therefore all three configurations are possible for phase I from this point of view.

Expected Pile-up Rate

Pile-up events have to be corrected or cut properly; otherwise they deteriorate the energy resolution. To even avoid this effect, smaller count rates are preferred. To determine the

Activity	[kBq]	12.5, 17.5, 17.7	17.5, 12.5, 17.7	17.7, 17.5, 51.1
mean event rate	[cts/s]	260	270	460
mean r_{pu}	[%]	4 ± 1	4 ± 1	6 ± 1
max event rate	[cts/s]	400	400	990
max r_{pu}	[%]	6 ± 1	5 ± 1	12 ± 2

Table 5.9: Mean and maximum pile-up for different source configurations. Reference date for all source activities is 31 March 2011.

pile-up rates for the different source configurations, the following estimate can be used [69]:

$$r_{\text{pu}} \cong n\left(1 - n\tau\right) n\tau \tag{5.12}$$

with n the event rate and τ the decay time of the preamplifyer. As a realistic estimate $\tau = 145\,\mu s$ was used (see section 7.3). To determine the average event rate per detector for the different configurations, the energy spectra of all detectors normalized to 1 h of calibration time were summed up, integrated and divided by the number of detectors. Additionally, the maximum event rate was determined integrating over the spectrum of the detector with the maximum count rate.

The results for the different configurations as absolute values as well as percentages of the event rate are shown in table 5.9. None of them is critical although the maximum rate for the third configuration (17.7, 17.5, 51.1 kBq) might be a little high.

Background from Real Sources

In the next step the background was scaled to the different configurations, rescaling the results from section 5.6. Since the background contribution is independent of the exact position of the source, just two of the three investigated possibilities are distinguishable: Configuration A with 12.5, 17.5 and 17.7 kBq sources and configuration B with 12.5, 17.7 and 51.1 kBq sources.

Table 5.10 shows the different background contributions for these two configurations, giving in comparison to the values for three custom 20 kBq sources. The latter especially

Activities	[kBq]	3x20	12.5, 17.5, 17.7	17.7, 17.5, 51.1
γ back	[10^{-5} cts/(keV kg y)]	4.3	3.4	6.2
n scatter	[10^{-5} cts/(keV kg y)]	6.2	10.3	30.0
Ge77	[10^{-5} cts/(keV kg y)]	4.0	6.7	19.5
Top Total	[10^{-5} cts/(keV kg y)]	14.5	20.4	54.9
Bottom			27.6 kBq	
γ back	[10^{-5} cts/(keV kg y)]		121	
n scatter	[10^{-5} cts/(keV kg y)]		11.0	
Ge77	[10^{-5} cts/(keV kg y)]		7.4	
Bottom Total	[10^{-5} cts/(keV kg y)]		139	
Total	[10^{-5} cts/(keV kg y)]	154	160	195

Table 5.10: Background contribution for different source configurations. Included also the background of the source at the bottom of the cryostat. Reference date for all source activities is 31 March 2011.

demonstrates the influence of the larger neutron flux in case of commercial sources (see table 5.7) which dominates the total background contribution. Both, higher γ and neutron flux, are combined in configuration B with two commercial sources (17.5 and 51.1 kBq) compared to one commercial source in configuration A. Nonetheless, both background contributions are well below the phase I goal of 10^{-2} counts/(keV·kg·y) and therefore an option for their usage in the calibration system. Since the aim is the lowest possible background, configuration A is obviously favored.

Taken into account that the activity of configuration A is sufficient for a successful calibration in a reasonable amount of time, these sources were chosen for GERDA's phase I. It was also decided to put the 12.5 kBq source on position S2 (see figure 5.2) since there is another source on this side of the array. It is nonetheless advisable not to place the smallest detector ANG 1 in detector string D3 which gets by far most of its statistics from the source at position S2.

The source at the bottom of the cryostat has at the reference date 31 March 2011 an activity of 27.6 kBq. Its background contribution is also listed in table 5.10 together with the total background expected from all four sources. The γ background from the bottom source is dominating not just the background from the bottom source itself but the background contribution of all sources in total. Thus, it is still under discussion if there is a possibility to remove the source from the cryostat, maybe even without emptying argon and water tank. However, at the time of writing, the best solution for phase I is still to leave it in the cryostat but it is obvious that this is not possible for phase II.

With the start of phase I at 01 Nov 2011, the source activities reduced to 13.1, 9.3 and 13.0 kBq for the calibration sources at the top and 22.3 kBq for the source in the cryostat. Rescaling the total background contribution to these values leads to

$$B_{\text{total}}(\text{P1}) = (1.28 \pm 0.01(\text{stat}) {}^{+0.10}_{-0.10}(\text{sys})) \times 10^{-3} \text{ counts/(keV·kg·y)} \qquad (5.13)$$

Comparison of GTF Data with MCS

The very first detectors deployed into GERDA were natural germanium detectors from the Genius Test Facility (GTF). The data of GTF 32 and GTF 112 was compared to MCS. In this case, the data was used to determine the energy resolution of each detector separately which was then folded into the MCS results. Figure 5.16 shows the full energy spectra for both detectors together with the 2.6 MeV lines of ^{208}Tl and their single and double escape peaks.

The 2.6 MeV line is used as the reference peak for the energy resolution of the detectors. The plots obviously show a tail to lower energies which is not visible in the MCS. This tail is due to pile-up events which are not yet corrected or cut properly. Later affords tried to take care of this feature to reduce the tail. However, it just appears in calibration data due to the higher trigger rate, and is not visible in background or physics data.

The SEP is important for the energy calibration since it is closest to the Q-value. The DEP is used as a sample of single-site events for pulse shape calibration. The overall agreement is very good. Small uncertainties remain because the position of the detectors in the cryostat is not well-defined. Current affords are ongoing to determine it precisely.
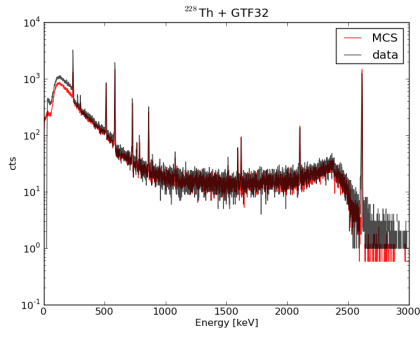
(a) GTF 32 total
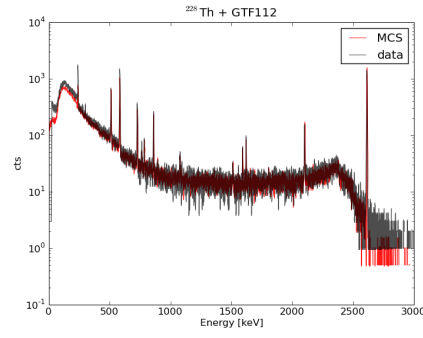
(b) GTF 112 total
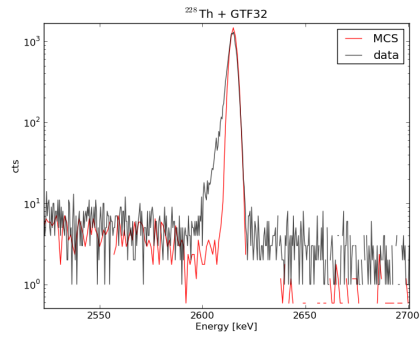
(c) GTF 32 2.6 MeV line
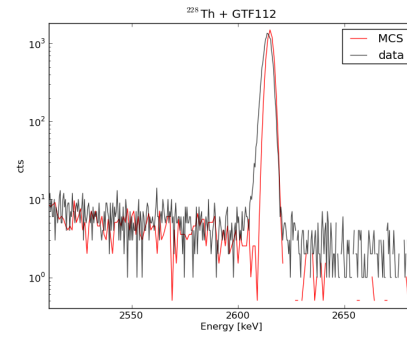
(d) GTF 112 2.6 MeV line
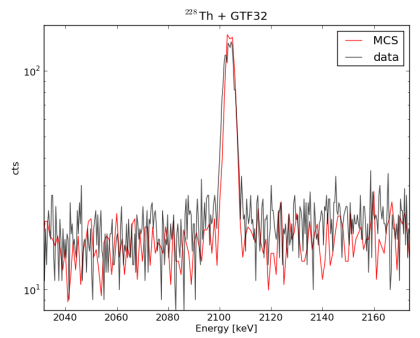
(e) GTF 32 SEP
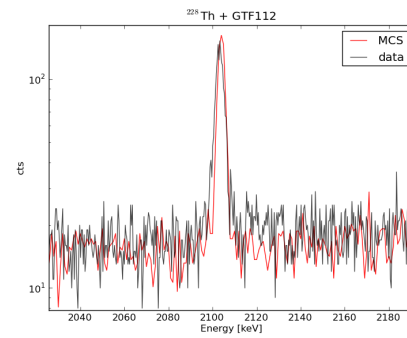
(f) GTF 112 SEP
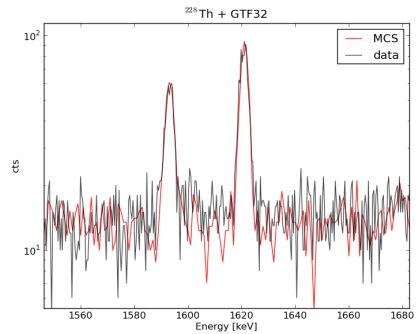
(g) GTF 32 DEP
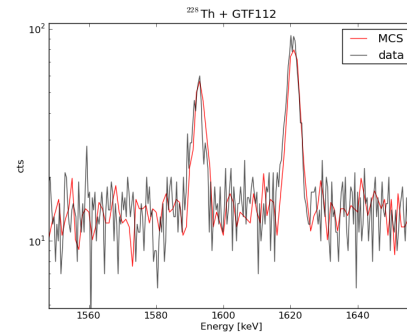
(h) GTF 112 DEP

Figure 5.16: Comparison of MCS with first data taken with GTF 32 and GTF 112. Besides the full energy spectrum, the 2.6 MeV line of ^{208}Tl is shown together with its single and double escape peak which are important for energy and pulse shape calibration. Besides the tail of the 2.6 MeV line which is due to pile-up events not present in the MCS, the agreement is very good.

5.8 Summary

Monte Carlo Simulations were used to determine the relevant parameters and characteristics of the calibration system for GERDA's phase I. Three ^{228}Th sources placed in the horizontal plane as close as possible to the detectors to prevent scattering of the γ's in the liquid argon are necessary for a successful calibration. In the vertical direction, two positions between the detector layers are necessary to reach sufficient statistics in each detector. The three sources used in the experiment have an activity of 17.5 kBq, 12.5 kBq and 17.7 kBq at 31 March 2011, which is in the middle of the commissioning phase. With this activity, a successful calibration can be performed in about half an hour per position. Two of these sources are custom made to lower their neutron yield.

During a physics run the calibration sources are parked on top of the cryostat and the radiation of the sources might contribute to the background in the region of interest. Furthermore, during an accident in September 2010 one of the calibration sources with an activity of 27.6 kBq fell into the cryostat and has to be taken into account as well. Both γ as well as neutron radiation as result of (α,n) reactions were considered and a total background contribution from the top sources of

$$B_{\text{top}} = (2.0 \pm 0.1(\text{stat}) \, {}^{+0.2}_{-0.3}(\text{sys})) \times 10^{-4} \text{ counts/(keV·kg·y)} \tag{5.14}$$

was found. This is well below the background goal for phase I, which is 10^{-2} counts/(keV· kg· y). A shielding of each of the top sources with 6 cm of tantalum was necessary to reach such a low background contribution. The bottom source contribute with a total of

$$B_{\text{bottom}} = (13.9 \pm 0.1(\text{stat}) \, {}^{+1.2}_{-1.3}(\text{sys})) \times 10^{-4} \text{ counts/(keV·kg·y)} \, . \tag{5.15}$$

Although this value is significantly higher than the background from the top sources it was decided that the source can stay inside the cryostat for GERDA's phase I.

Comparison of Monte Carlo simulations and the first data taken during the commissioning phase with GERDA is in very good agreement.

The GERDA Calibration System

After investigating the relevant characteristics of the calibration sources, the actual calibration system had to be designed. This system consists of three calibration sources, their tantalum absorbers, the systems to lower them to the calibration positions and its control unit.

To be able to compare Monte Carlo Simulations with data to determine and monitor the stability and efficiency of the detectors, a position determination of the calibration sources of 5 mm or better should be reached. The calibration sources are parked at the top of the cryostat at room temperature. During a calibration run, the sources are lowered through warm and cold argon gas in to the liquid argon down to the detectors. The different temperatures have to be considered for position determination and material selection. The latter is especially important for the capsule of the ^{228}Th source, which has to be applicable for cryo liquids. Due to space limitations explained in section 5.3 the system cannot extend a height of 27 cm. A sketch of the situation at the parking position of the calibration sources is shown in figure 6.1.

During the mounting process, the calibration system has to be vacuum pumped and flushed with argon gas for a few cycles in order to remove air and possible other contamination from the system. Afterwards in can be connected to the cryostat. Thus, all parts have to be applicable for vacuum and a connection to the GERDA gas system is necessary. The different parts of the prototype as well as the final system are described in detail in the following sections.

6.1 The Absorber

To ensure the low background required for a successful operation of GERDA, the calibration sources have to be shielded in their parking position. The possible shielding material needs to be as radio-pure as possible with very good absorption properties and has to be machinable. Three different materials were investigated: Tungsten with a purity of 99.97%, Densimet D176 which is a tungsten alloy with 92.5% W, 5% Ni and 2.5% Fe [101], and tantalum with a purity of > 99.90%.

The absorption properties of all three materials were compared using linear attenuation using equation 3.6. The relevant parameters are given in table 6.1. Since the mass attenuation coefficients are more or less the same for all three materials, the main difference is their density. It is therefore not surprising that tungsten shows the best absorption proper-
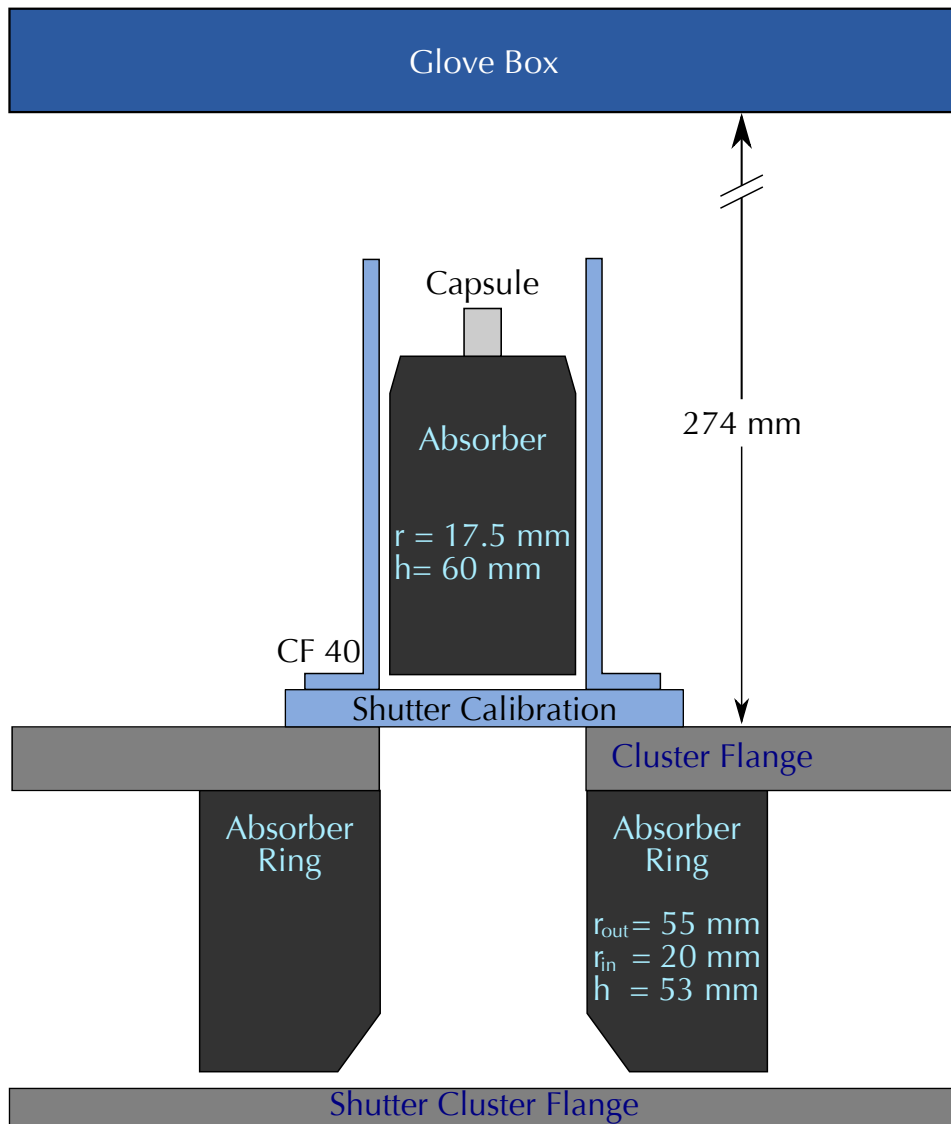
Figure 6.1: Schematic view illustrating the situation at the parking position of the calibration system. In light blue the shutter as well as the flange and pipe of the calibration system. In light grey the cluster flange and its corresponding shutter which closes the cryostat on its top. Both shutters are usually open in physics as well as calibration mode. In dark grey the shielding material including dimensions. The dark blue rectangle indicates the glove box. Included also the space between cluster flange and glove box available for the calibration system.

ties, then Densiment and then tantalum.

For better comparison on the influence on the background estimate for the GERDA experiment, the contribution was calculated using 3 m of LAr and 6 cm of absorber material. For the shielding capabilities of LAr the semi-analytical approach described in section 5.6 was used with three sources and an activity of 20 kBq each. Due to the height restrictions of the whole calibration system, the shielding cylinder has a maximum height of 6 cm (see figure 6.1). Thus, the 6 cm represent the maximum shielding capability of the investigated materials in this case. It turns out that the background contribution with a tantalum ab-

	Tungsten	Densimet	Tantalum
ρ [g/cm^3]	19.3	17.6	16.6
μ [cm^2/g]	0.0414	0.0414	0.0413
l [cm]	1.250	1.371	1.460
B [10^{-5} counts/(keV·kg·y)]	2.17	3.31	4.28

Table 6.1: Comparison of the absorption properties of different absorber materials. The mass attenuation coefficient is given for 2.6 MeV γ's. The background index was calculated using the semi-analytical approach (see section 5.6) for 3 m of LAr and linear attenuation for 6 cm of the absorber material.

sorber would be about twice as large as with a tungsten absorber. The contribution with a Densimet absorber would be between both values. However, all values are well below the GERDA phase I goal and therefore all materials are possible candidates, with a preference to higher densities.

All possible materials were screened for radioactive contamination with the Gator screening facility [102]. The results can be found in table 6.2. Tungsten has a high ^{238}U contamination which emits photons with an energy over 2 MeV and can therefore contribute to the background in the region of interest (ROI). The emitted α's, however, are uncritical since their energies with a maximum of 6.1 MeV are well below the minimum activation energy of 9.2 MeV of the different tungsten isotopes and thus no (α, n) reactions can take place. Another problem of tungsten is that it is very hard to machine because it is very brittle. In principle, ultra high purity tungsten with a 99.9999 % purity level exist but it is a custom product with a minimum purchase of 135 kg and therefore not suitable for GERDA.

Densimet is a tungsten alloy designed to be easier machinable than tungsten but keeping its other properties. Unfortunately, its radioactive contamination is relatively large with ^{238}U and ^{232}Th as possible γ emitters. Furthermore, the produced α's with energies up to 8.8 keV find reaction partners in the iron and nickel content which has activation energies as low as 1.5 MeV. Therefore, neutron production is very likely.

Tantalum showed the best radio purity with a ^{182}Ta contamination of 52 ± 5 mBq/kg. ^{182}Ta does not emit β's or γ's with an energy above 2 MeV and no α's at all. Therefore, no background contribution in the ROI can be expected. It is brittle as well and therefore also difficult to machine but not as hard as tungsten. It is therefore the best candidate. Since its shielding capabilities are good enough for GERDA's phase I, it is used in the experiment.

[mBq/kg]	Tungsten	Densimet	Tantalum
^{238}U	300 ± 100	180 ± 30	< 11
^{232}Th	30 ± 10	70 ± 20	< 9
^{60}Co	< 8.1	7 ± 2	< 1.9
^{40}K	40 ± 20	< 57	< 33
^{137}Cs	-	-	< 2.5
^{182}Ta	-	-	52 ± 5

Table 6.2: Screening results of possible absorber materials. No contamination of ^{137}Cs or ^{182}Ta were found in case of Tungsten or Densimet.

(a)   Tantalum   (b) Ring including its holder with the   (c) Rings mounted at the bottom of the clus-
absorber including   absorber inside   ter flange
holder
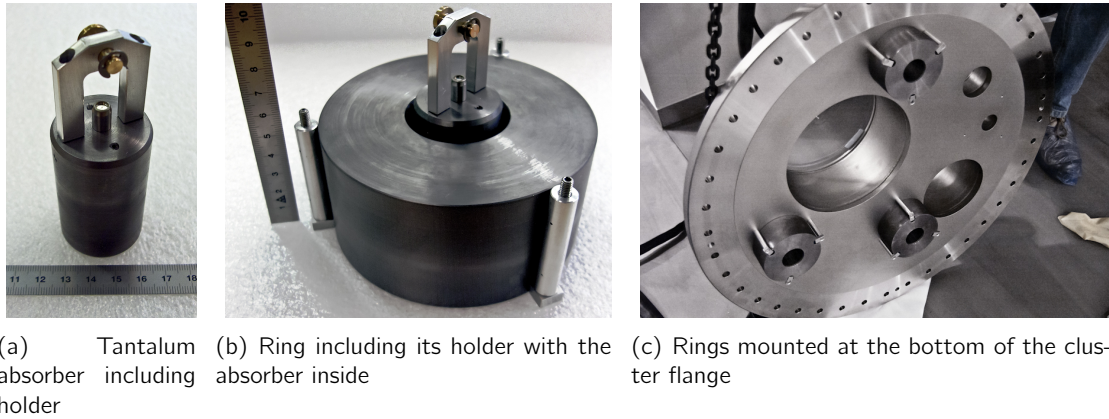
Figure 6.2: The different parts of the first version of the calibration system built by
UZH: The tantalum absorber with holder and the tantalum rings to shield the source
in the parking position. The rings are mounted below the cluster flange and are still
present in GERDA. The design of the holder changed in later versions.

The tantalum cylinder ensures the necessary shielding just for photons emitted downwards.
However, photons traveling with a small angle towards the downwards direction might not
be sufficiently shielded because of the relatively small diameter of 35 mm of the cylinder.
Therefore, further shielding is necessary. Since there is basically no space on top of the
cluster flange, it was decided to mount tantalum rings below it. Their height is limited due
to the corresponding shutter used to close the cryostat, which is located 55 mm below the
flange, their outer radius due to the distance to the detector flanges. An schematic view
of the system illustrating the dimensions can be found in figure 6.1. Indicated as well are
the chamfered edges of the absorber as well as the ring which ensures smooth entry of
the absorber when lifted up. The rings were installed in January 2010. Pictures after their
installation as well as the other parts of the calibration system built by the UZH can be
found in figure 6.2.

The cylindrical absorber was included in all Monte Carlo Simulations. The only excep-
tion are the simulations required for the determination of the background contribution of
the sources. In this case no absorber was simulated in order to increase the statistics.

6.2   The Prototype

The first, preliminary version of the calibration system was built for the commissioning
phase in order to determine the detector performance, especially their energy resolution.
It was planned to built two more system for the start of GERDA's phase I. The time gap
between the building of the first system and the second and third system was scheduled
to be able to modify the later systems according to experience with the usage of the first one.

The system consisted of a lowering system built by LNGS, and a cylindrical absorber plus
holder with the calibration source on top built by UZH. The technical drawing as well as a
picture of the mounted system can be found in figure 6.4.
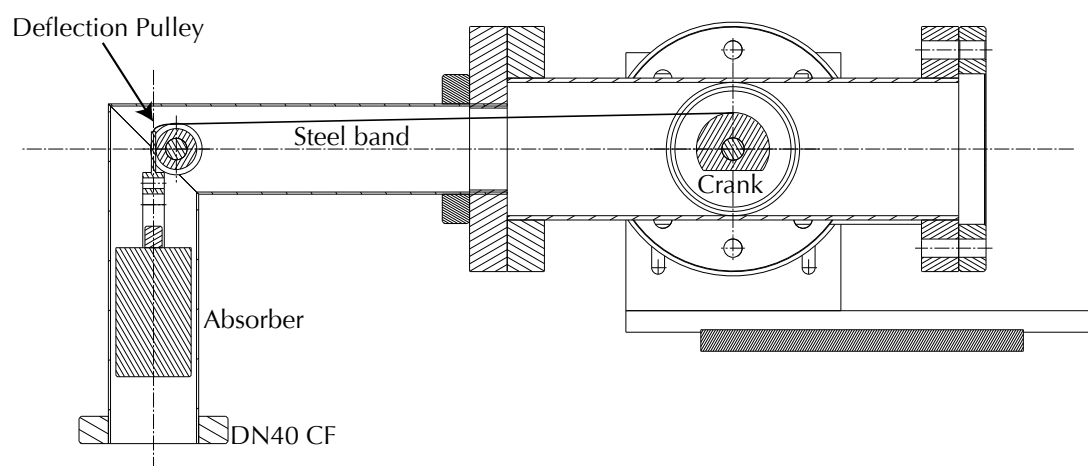
Figure 6.3: Technical drawing of the prototype showing a cut through the system. Labeled are the most relevant parts. Drawing provided by Donato Orlandi, LNGS.

The calibration source is encapsulated in a PO2 capsule shown in the figure on the right. It is tested in cryo liquids and can be screwed on top of the absorber via an M4 thread. The absorber itself is a tantalum cylinder with a height of 6 cm and a diameter of 3.5 cm; the latter it the maximum possible diameter which still fits through the DN 40CF flange and pipe. A picture of the absorber together with the holder and a calibration source is shown in figure 6.2. The holes on the surface of the absorber connect the thread of the calibration source with the remaining volume to fulfill the required vacuum standard.
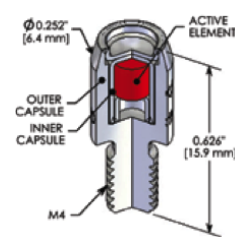
The holder is then connected to a steel band which was in the first prototype just the band from a 10 m roll-up tape measure. Such a band had the required length, width and thickness, it is cheap and it made adjusting the system in the first tests very easy. The band is rolled up an a crank, whose full turns have to be connected to the length of the steel band rolled-up. This is position dependent due to the changing radius. In principle, this can be calculated but a measurement is necessary to determine the effect of imperfect rolling-up. For details on the tests and measurements performed prior to installation of the system, see section 6.3. However, it turned out that the band does not fulfill the requirements on radio purity even after removing all the paint from the tape measure.

Instead, a steel band from the Meterdrive system by Vectral [103] was used which also measures the movements of the detector strings. The used band had a width of 15 mm, a thickness of 0.1 mm and is perforated. The Meterdrive system uses the perforation together with optical sensors to determine the movement of the band. Unfortunately, the entire system was to large to be implemented in the prototype but the idea was used in the final system. Therefore, just the steel band was used for the prototype.

Owing to the limited space between cluster flange and glove box (see section 5.4), the steel band is deflected by 90 degrees before it is rolled up on a crank as can be seen in figure 6.3. All parts are housed in vacuum pipes. Since the radius of the crank is too big for a DN40 CF cross, a DN63 CF is used instead. However, this requires that the 90 degree angle connects on one side to a DN40 CF flange on one side but to a DN63 CF on the

(a) Technical drawing of the prototype

(b) Mounted prototype during commissioning phase.
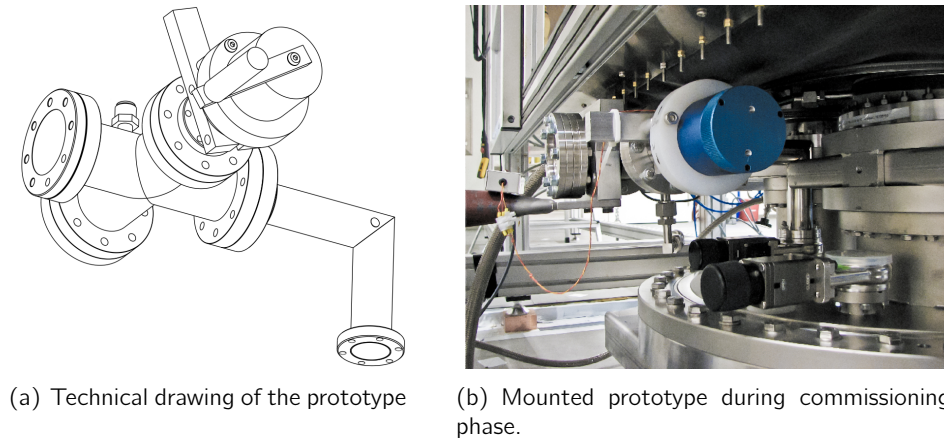
Figure 6.4: Prototype of the calibration system. Figure (a) shows a technical drawing of the system. The handle at the end of the rotary feedthrough was removed due to space issues. Figure (b) shows a picture of the mounted system during commissioning phase. Blue the end of the rotary feedthrough with the nonius, in white just behind it the teflon pieces of the break. On the left the glass flange of the DN63 CF cross.

other. Together with the required length of each arm, such a piece is commercially not available. During the welding process, the deflection pulley was also inserted in the angle.

The crank is connected to a hermetic, bellow sealed rotary feedthrough with nonius allowing manual operation of the system. Four magnets were implemented on the nonius and a hall sensor is used to count the turns of the feedthrough. Since this system is obviously insensitive to the direction of the movement, the operator had to take care of this. Furthermore, each count of the hall sensor represents a 90 degree turn, which corresponds roughly to 3 cm of band. This, together with the slip of the rotary feedthrough, leads to an accuracy for position determination with the system of about 5 cm. However, the reproducibility of a position determined in tests described later, is much better. Nonetheless, an improvement for the final system is necessary. It was planned to be reached with the installation of a motor where is no need a teflon break and whose turns can usually be determined with much higher precision.

Two teflon pieces were installed as a break for the system; it had to be released in order to move the system. A connection to the GERDA gas system is required for the mounting procedure. Thus, a VCR 1/2" was welded to the DN63 CF cross. For easier and more precise mounting two rotating flanges were used, one at the end of the 90 degree angle connection to the cluster flange and one at the DN63 CF cross connecting to the 90 degree angle. The end of the cross pointing to the operator was closed by a glass flange showing the band on the crank and therefore allowing to supervise the movement of the band. The parking position was marked on the band to verify that the source if fully lifted up after a calibration run. Another indicator that the absorber is back in the parking position is the water condensating on the outside of the pipe due to the cold absorber inside of it. Figure 6.4 shows a technical drawing of the system together with a picture of the mounted prototype during calibration phase.

After first tests in January 2010 the prototype was installed in the first week of June 2010 together with the first lowering system for the detectors. The performed tests and

the resulting procedure to operate the system are described in the next section. Manual operation of the system went smoothly.

End of September 2010 the system was upgraded by a step motor connected to the rotary feedthrough. Motor and the corresponding control unit were designed and tested by LNGS and mounted together with UZH. The Hall sensor was kept as a reference system. The motor control unit allowed basic functions: One button each to lower or lift the source, one to reset the position to zero and one to safe the current position. An LED panel showed the current position. One full turn of the rotary feedthrough corresponds to 200 cts on the motor control unit and therefore 50 motor counts correspond to 1 hall sensor count leading to a much better accuracy of the system. During installation, just basic functionality tests were performed and calibration data taken.

6.3 Testing the Prototype

In January 2010, first tests were performed with the prototype to determine its functionality and accuracy as well as to test its vacuum tightness. The system was mounted on a rail first in the LNGS workshop and than at the GERDA building underground, allowing to lower the source for 3 m and 10 m, respectively. During these tests, the measuring tape was still in use allowing easy determination of the actual position.

For the first tests in the LNGS workshop, a test weight of 3 kg was used which is about 3 times heavier than the actual weight of the absorber. This was done primarily to ensure the proper functioning of the teflon break, which was suppose to hold the absorber in its current position. The weight was lowered to 2.5 m and left there overnight. No movement of the system was found and thus, the break is working properly in this terms.

However, first movements showed that the break was not working equally, leading to ranges with less resistance than others. Furthermore, the rotary feedthrough had some play at the beginning of each movement. Both effects lead to a decrease in the positioning accuracy but does not affect the overall usability of the system. It was therefore decided by LNGS to leave the system as it was.

During movements the system showed just little oscillation but larger rotations. They were enhanced by nonuniform rotations of the crank which were mostly caused by the unequal resistance of the break. A guiding rail at the deflection pulley was advisable. The oscillations were further investigated at the staircase of the GERDA building underground, which allowed to lower the system over its full range of 10 m. After shielding the experimental side with plastic foil to avoid external winds, oscillations of less than 5 mm were found. This is already small enough for GERDA and even further damping due to the liquid argon can be expected. Pictures of the experiment can be found in figure 6.5. During these tests, no problems were found with the reentry of the absorber into the pipe.

All above tests were repeated by the LNGS group solely after exchanging the steel band. No changes were found especially in case of oscillations or rotations.

Before the installation of the system in the first week of June 2010, the system was successfully tested for vacuum leaks, leading to leak rates of 10^{-7} mbar l/s. After mounting, the influence of the argon was tested for the first time an the real scale. It was expected
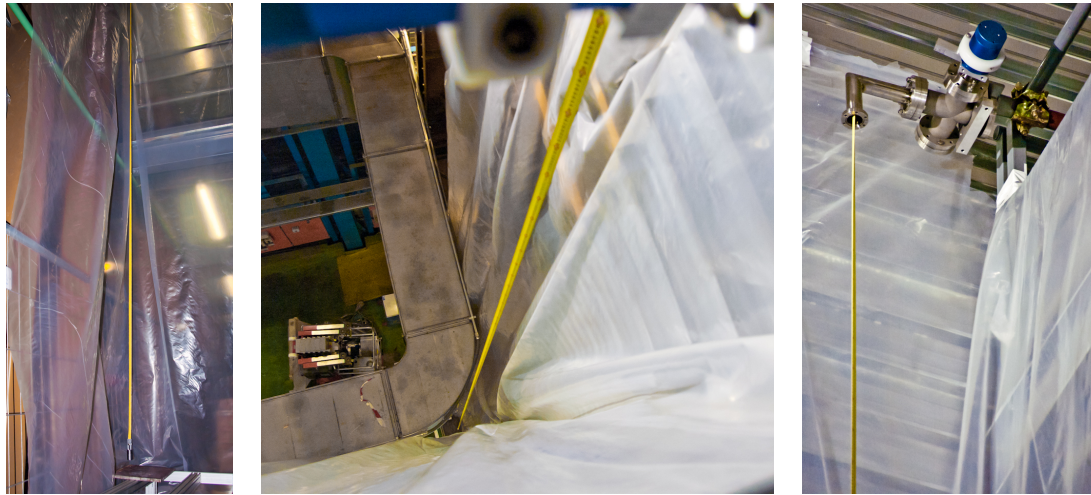
(a) Absorber lowered over 10 m.

(b) Lowered absorber seen from the top with the rotary feedthrough at the upper edge of the picture.

(c) Prototype mounted at the GERDA rail.

Figure 6.5: First tests with the prototype calibration system at the GERDA building underground.

that the boiling of the LAr, when the absorber enters for the first time, might cause some enhancement of the oscillations and rotations of the system. Since no detectors were operating, it was possible to switch on the light in the cryostat and use a view port to check this effect. The position of the LAr level was determined in Hall sensor counts and tests showed, that stopping the absorber at this point for about 5 min is sufficient to ensure that oscillations and rotations are on a small enough level. The order of magnitude was comparable to measurements before the entry and can be assumed to be on the same level as those measured outside.

The whole procedure to operate the calibration system, including the counter for the Hall sensor and the stop position at LAr level, was fixed in a logbook which also provided the operator with the necessary tables to save the current position of the calibration system.

6.4   The Intermediate System

During a calibration run just after the motor installation, problems with the calibration system occurred and in the consequence the calibration source and its absorber fell into the cryostat and are now lying on its bottom. Since the steel band could be nearly fully recovered, it broke or got cut just above the holder of the absorber. The reason, however, is still unclear and two theories exist. Both assume a disagreement in the actual position of the source and those indicated by the two positioning systems, the Hall sensor and the motor, which both showed different values.

The first theory assumes that the steel band was cut by the shutter of the calibration system. The latter was closed when the problems occurred in order to inspect the system and the operator assumed the source already in its parking position. As a consequence, a shutter control was implemented in the final system.

(a) Steel band   (b) Plug-in unit with absorber at the mechanical end stop   (c) Absorber with new holder
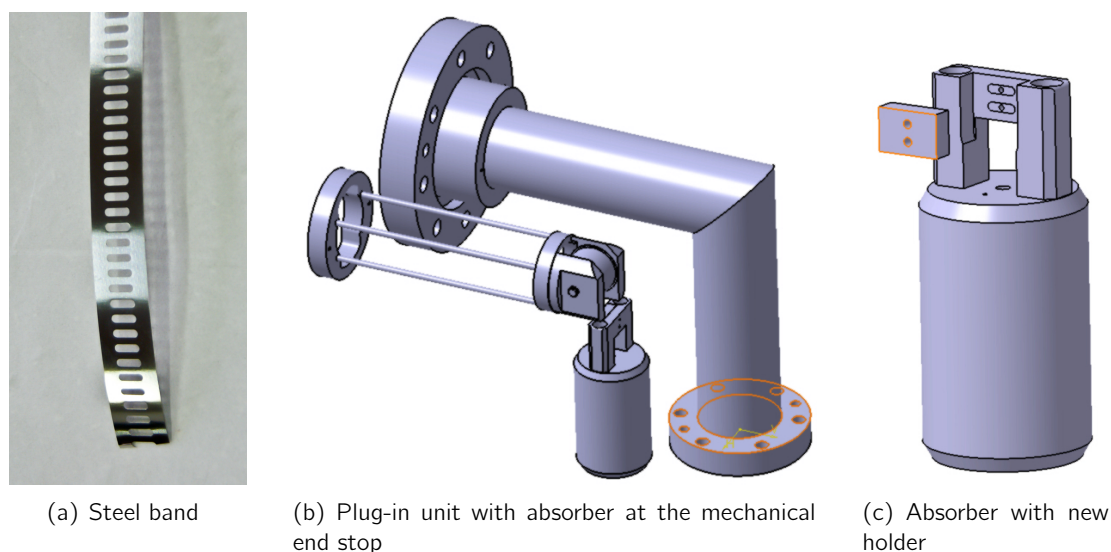
Figure 6.6: The intermediate calibration system. Figure (a) shows the Meterdrive steel band which was already used in the prototype. The holder of the absorber was adjusted to this band such that the perforations fit into two precisely machined bosses, see figure (c). Figure (b) shows the new plug-in module providing the required end stop for the absorber as well as easier mounting of the system.

The second theory assumes that the absorber was pulled up higher than it was suppose to. As a consequence, it would not smoothly bend over the deflection pulley anymore but rather folded just behind the holder. This could create a predetermined breaking point. Since the motor had no current limitation or other safety precautions it is possible that it continued pulling until the band broke. To prevent this in future systems, a stopper is requested below the deflection pulley which ensures that the absorber cannot lift any further. Additionally, several precaution systems are installed to limit the force the motor can transmit on the band.

To ensure a reliable positioning for the final calibration system, two independent systems are used. In case the difference between their values is larger than a predefined threshold, the system stops automatically. The error protocol than requires a supervised lift up of the source; the arrival at the parking position will be ensured by an electrical end stop. Details will be described in section 6.5.

After the accident, it was important to get a new calibration system as fast as possible to not interrupt the commissioning phase more than necessary but not without taking into account some safety issues. Since the motorization required extensive reviewing, it was decided to build a manual system for intermediate usage and postpone the motorization for the final system to be installed later after extensive testing. One major request was an end stop for the absorber to prevent the holder from being pulled over the deflection pulley. Due to the lack of any electronics inside the vacuum pipes for the intermediate system, this had to be done mechanically.

The UZH group took over the responsibilities for the modifications and the design and construction of the final system. The LNGS group assisted by providing all technical drawings of the prototype and planning the connection to the gas system. The main principle

stayed the same, with the motor disconnected again. A major change was the design of the 90 degree angle and the design of the deflection pulley. Instead of welding the latter into the angle, a complete new plug-in module was designed as shown in figure 6.6. This has the advantage of an easy implementation of the required end stop: Due to the rectangular shape at the deflection pulley the new holder hits this structure when reaching the parking position before it can be pulled over the deflection wheel. Furthermore, later revisions can be performed easily and the mounting procedure was simplified significantly.

The holder of the absorber was also adjusted to the new design, especially the connection to the steel band changed, which can be seen in figure 6.6 in comparison to figure 6.2. The steel band was placed onto the top part of the holder which had two precisely machined bosses exactly fitting the perforation and thickness of the band. A second part was screwed on top of it with two M2 screws. The deflection pulley was also adjusted to the width of the steel band and provides a small rail as guidance system for the band. The latter should decrease oscillations and rotations of the steel band. The plug-in module was screwed into the 90 degree.

The other parts with the DN63 CF cross, crank and rotary feedthrough were used from the prototype. The vacuum leak test of the intermediate system was successful with rates around 10^{-7} mbar l/s. It was tested in the workshop at LNGS similarly to the prototype, before it was installed at GERDA in November 2010. Its manual operation went smoothly until the final system was installed.

6.5   The Final System

The final calibration system consists of three identical units, one for each calibration source. Each unit is motorized and connected to the same motor control unit which provides basic functionality of the three lowering systems. The motor control unit is connected to a remote control. The design is based on the prototype by LNGS and the subsequent experiences in its usage. The different parts are described in detail in the following. A 3D view can be found in figure 6.7.

Source encapsulation and absorber stayed the same as in the intermediate system. The first change was forced by the fact that Vectral could not provide us anymore with the 0.1 mm thick stainless steel band. Unfortunately, the 0.2 mm version is too big for the DN63 CF cross: Even a perfectly rolled-up band would have due to its minimum bending radius and the thickness of the band a radius of 32.6 mm for the crank, assuming a length of 7 m. The usage of a bigger cross is not possible because of the space available between cluster flange and glove box, and the required shielding of the source leading to an absorber height of 6 cm.

It was therefore decided to buy a standard stainless steel band with the required thickness of 0.1 mm and laser cut the necessary perforation into it. Round holes were used instead of the oblong ones from the old band to ensure the stability of the band and because of financial reasons. Holder and deflection pulley were modified accordingly.

The plug-in module was extended by a micro switch installed at the rectangular end of the module. A small bar connected to the holder of the absorber pushes this switch signaling the uppermost position, the initializing position. The parking position is 1 cm below
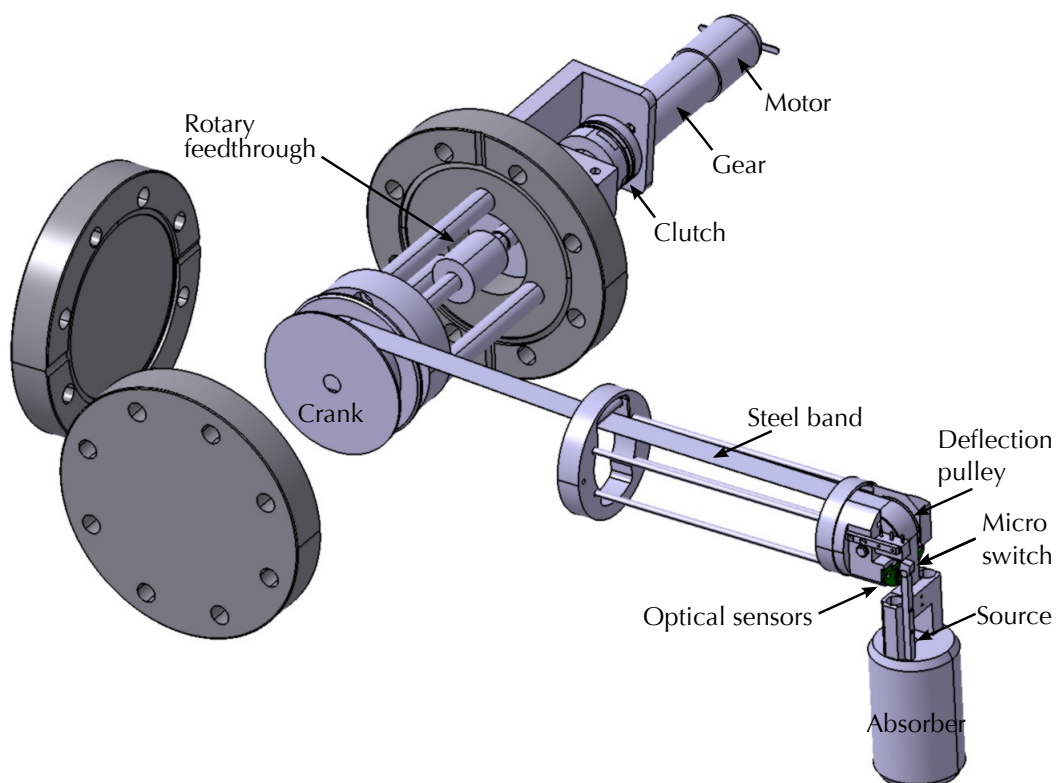
Figure 6.7: 3D view of the final system labeling the most important parts.

this position. The new absorber, holder and plug-in module are shown in figure 6.8.

The rotary feedthrough was replaced by a Vacom Superseal with magnetofluid sealing, details can be found in appendix B. The main reason is the better connection to the motor used in this system. It is shown in figure 6.8. Opposite to the feedthrough is a blind flange, which will be used for electronic feedthroughs described later as well as the connection to the gas system, which will be again a VCR 1/2" connector.

The motorization is realized connecting the rotary feedthrough via a Maxon GP22C planetary gearhead to a Maxon RE-max24 DC motor. The combination was chosen because it fulfills two major requirements: First, it is able to lift more than 1 kg, which is sufficient for the absorber plus steel band. Second, the required movement speed can be adjusted to around 10 mm/s with some flexibility. A DC motor was chosen because the DC mode minimizes radiation (connection cable) and the control is simple and therefore the hard- and firmware effort for the motor control unit minimal. The latter was important because the final system had to be installed before the start of phase I to provide the two more necessary calibration sources and to not disturb the physics data taking. The stopping time of the DC motor after switching off its supply voltage was found to be insignificant. The complete data sheets are available in appendix B. For safety reasons, a friction clutch is located between the gearhead and the rotary feedthrough to restrict the force from the motor on the crank. Furthermore, the motor current is limited for the same reason.

The system is equipped with two independent positioning systems: The first one is the incremental encoder counting the holes in the steel band with the help of one LED on one

(a) Absorber

(b) Plug-in Module

(c) Crank

(d) Rotary feedthrough

(e) Motor Controller
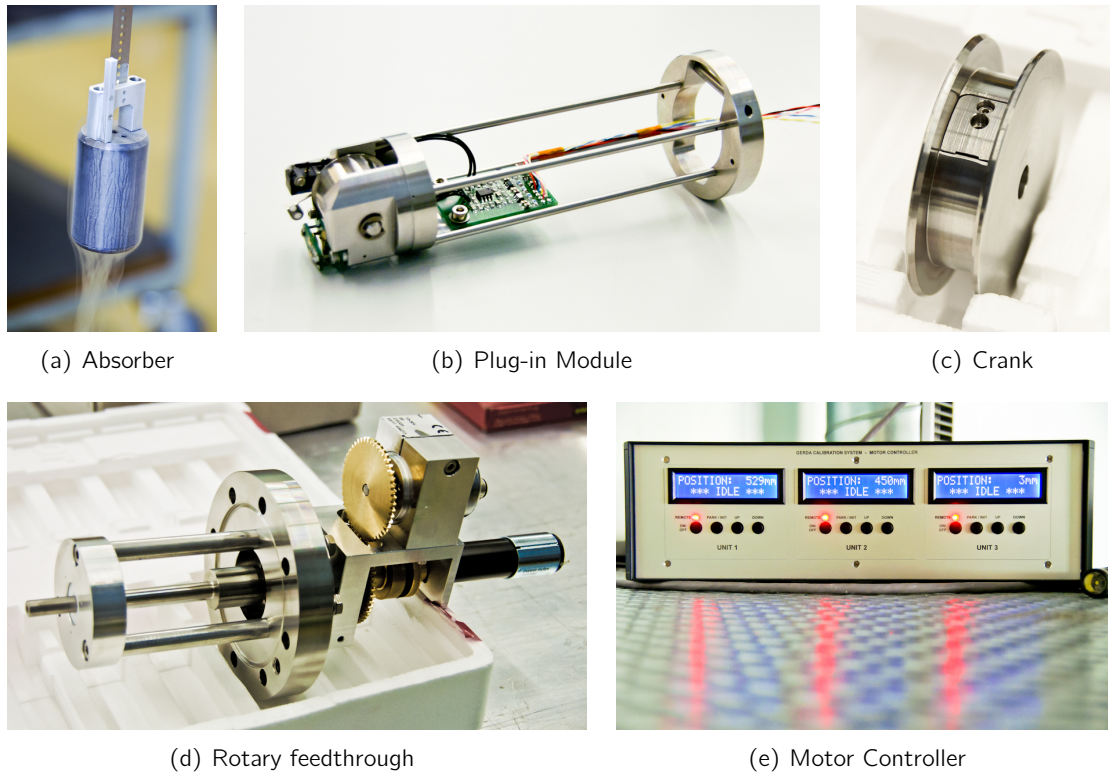
Figure 6.8: Different parts of the final calibration system.

side of the band and two optical sensors on the other. The chronology of the impulses of the two sensors determines forward and backward direction and can be used for error detection. The position is calculated via the known distance of the holes, which is 4 mm. The incremental encoder is positioned just below the deflection pulley; it can be seen together with the required electronics in figure 6.8(b). It has to be initialized before usage since it is sensitive only to relative position changes. The initialization is performed by moving the source up to the micro switch, which is the defined reference point. The second system is the absolute encoder, which counts the rotations of the crank. It is connected via two cog wheels between rotary feedthrough and gear system. The number of rotations is stored with the help of an absolute multiturn rotary encoder, which provides absolute values even in case of a power failure. A position dependent function converts rotations into position.

The motor control unit shown in figure 6.8 consists of three functional identical blocks, one for each calibration system. The reference position is the parking position on top of the cryostat 1 cm below the end stop defined by the micro switch. All following movements are measured relative to this reference position via the two independent positioning systems. The control units checks for discrepancies between the two positioning systems, malfunction of each system separately, the motor current and other parameters to detect possible errors. An error protocol exists for the different cases.

A user interface at the motor control unit provides basic functionality of the three calibration system. Each calibration unit is controlled by four buttons to move the source up or down as long as the button is pressed, to go to the initializing position and a kill switch stopping all current actions. Each block has one LCD to show the current position of the

(a) Teststand UZH   (b) Teststand UZH   (c) Final calibration system
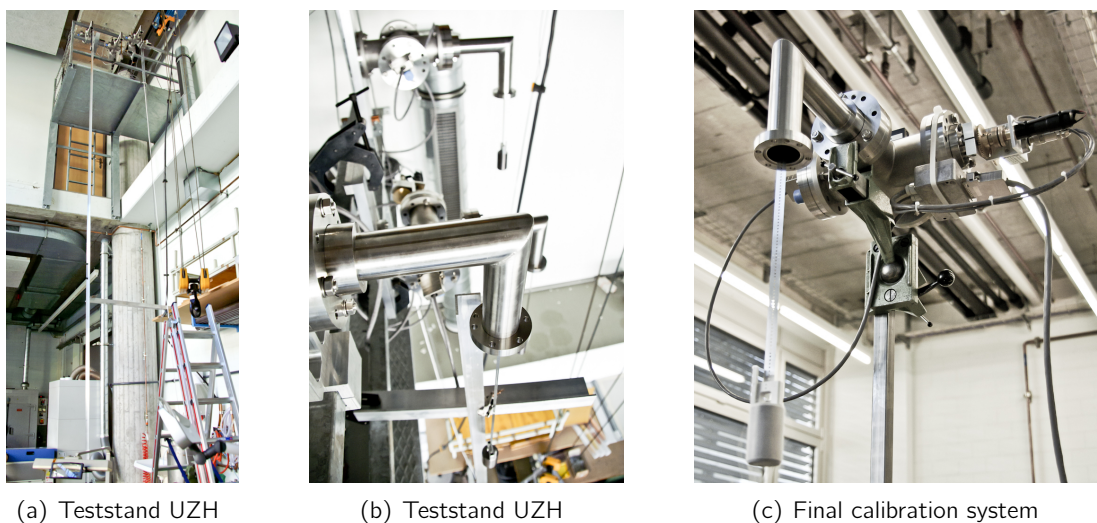
Figure 6.9: The final calibration system and the test stand in the assembly hall at the Physik Institut at UZH.

corresponding source or error messages respectively.

To provide a more convenient usage of the system, the motor control unit has an RS 232 as well as an RS 422 port to connect to an external computer. A remote control programmed in LabView enables various sets of tasks together with a long term monitoring of the system. It is connected to the GERDA slow control system.

Details on the motorization as well as the remote control can be found in the Ph.D. Thesis of Michal Tarka [96], who was responsible for this part of the project.

6.6   Testing the Final System

The final system was tested extensively before its installation in June 2011. It had to be verified that the new steel band can be used in a cryogenic environment. More detailed oscillation tests were performed, also replicating the entry of the absorber into the cryo liquid. The two new positioning systems were studied to determine their accuracy and to define the threshold they are allowed to diverge before the system is stopped. Furthermore, the long term stability was investigated. The error handling as well as the remote control were successfully tested by Michal Tarka and detailed results can be found in his Ph.D. thesis [96].

First tests were performed in the assembly hall of the Physics Institute at UZH allowing to lower the systems down to 6.5 m. Pictures can be found in figure 6.9. For one system, a guide rail was installed next to the band with reference points marked on it. After testing all systems successfully, they were cleaned in an ultrasound bath except for the electronics prior to shipment to LNGS. All parts were successfully tested for vacuum leaks. The fully assembled systems were again tested for vacuum leaks in the clean room before mounting them on the cluster flange. Last tests were performed on site.

Properties of the Steel Band in Cryogenic Liquid

The influence of a cryo liquid on the stainless steel band was tested using liquid nitrogen (LN). LN is easily available in the lab in Zurich and since it has about the same temperature as LAr (boiling temperature of N is 77.3 K and of Ar 87.2 K), test results are expected to be transferable. A test sample of about 70 cm of steel band was used for this test.

The thermalisation of the steel band with its surrounding temperature was measured in two different variation with 20 cycles each: In the first setting, one end of the steel band was still in the LN, in the second version the band was taken out of the LN completely. In case of inserting the band into the LN, the band was assumed to have the same temperature when the boiling stops. When removing the band afterwards, water from the air is condensating on the band which than evaporates while the band warms up. The band was defined to have room temperature after the water was evaporated.

With both version,s the thermalization was found to be the same inside the errors with $(21.0 \pm 1.2(\text{stat}) \pm 3.0(\text{sys}))$ s for the version with one end in LN and $(21.5 \pm 2.0(\text{stat}) \pm 3.0(\text{sys}))$ s with the fully extracted band. Therefore, it can be assumed, that the band always has the same temperature as its surroundings. Thus, the part of the band in LN has cryo temperature while the part outside has room temperature, with just a small transition zone.

In the next test, the steel band was cooled down to LN temperature. Than, it was pulled out of the dewar and bend over a pipe with a radius of 2 cm by a minimum or 90 degrees, which is the minimum bending radius required. The procedure was repeated for 20 cycles. No problems were found bending the band and a visual inspection after the cycles revealed no damages to the band.

In principle, the thermal expansion coefficient of the band should be measured as well to be able to correct the positioning systems accordingly. However, since the band thermalizes so quickly, it is not possible to measure the contraction outside the dewar and no measuring tools were available to measure the length inside the LN correctly. Instead, the thermal expansion was calculated using [104, 105]

$$\frac{L_T - L_{293}}{L_{293}} = (A + BT + CT^2 + DT^3 + ET^4)\,\text{e}^{-5} \tag{6.1}$$

with L_T the length of the band at temperature T, L_{293} its length at room temperature, and the coefficients $A = -2.9554 \times 10^2$, $B = -3.9811 \times 10^{-1}$, $C = 9.2683 \times 10^{-3}$, $D = -2.0261 \times 10^{-5}$ and $E = 1.7127 \times 10^{-8}$. The database provides values for four different types of steel. For the above case, they are all the same. Besides the LAr, also the cold argon gas above the LAr was taken into account in the correction function applied in the remote control. As an example of the significance of the effect the case with the source at its calibration position is used. In this case, a total of 4.1 m of cold environment is present, reducing the length of the band in this part to 4.089 m.

Oscillation Tests

One lowering unit of the calibration system was positioned in a distance of about 1.8 m from its top position to the LN level of a dewar. This is the expected distance in GERDA between parking position and LAr level. The oscillation and rotation of the system during movement was measured before and after entering the LN. Furthermore, a stop watch was

used to determine the time, the LN was boiling due to the immersion of the warm absorber as well as the time, oscillations and rotations are enhanced due to this fact. The test was repeated five times.

Before immersion, oscillations of < 5 mm and rotations of $25 - 30$ degrees were found. The boiling, which lasts for about 3 min, enhanced the oscillations to values up to 10 mm and rotations of $45 - 50$ degrees. All values were measured from peak to peak. The enhancement lasted for about 4 min. Afterwards, they were on the same level as before the immersion, which is sufficiently low for GERDA. Therefore, a stopping time of 5 min at the LAr level was found to be sufficient.

Different maloperations were investigated. In the first case, the absorber was moved further into the LN before stopping it to wait the required 5 min. The same effect as described above was found; the enhanced oscillations and rotations were again down to an acceptable level after the stopping time. Therefore no problem was found.

Next, the absorber was moved up to its parking position while the oscillations were more pronounced: The enhanced oscillations and rotations showed neither problems in moving the source (the incremental encoder was working properly) nor while re-entering the DN40 CF pipe of the calibration system. The absorber was also moved down while the oscillations were more pronounced. Again, no problems were found but testing possibilities were limited due to the size of the cryostat. At the end of this procedure, the absorber hit the bottom of the cryostat: The band started to slightly bend before the motor stopped as expected. The designated procedure in this case envisages to switch off and on the motor control. The now required initialization of the system lifted the absorber back in its parking position. Everything went fine.

In the next test, the absorber was moved just 10-20% into the LN and 5 min were waited, which is the intended stopping time at LAr level. Afterwards, the absorber was moved further down. This was simulating the case where the LAr level is not determined correctly or changed due to small instabilities in the cryostat. During the following lowering of the absorber, the LAr started to boil as expected. Again, more pronounced oscillations and rotations were found, consistent with the levels measured above.

It was than investigated, if this enhanced oscillation could lead to a collision of absorber and detector in the unlikely case where the oscillations do not damp during movement. The distance between LAr level and detector array is 3 m. Taking the moving speed of the absorber of 10 mm/s into account, it takes 1.8 m until the absorber thermalized and 2.4 m until the enhanced oscillation stops, assuming that the vertical movement does not influence the damping of the oscillation. An oscillation of 1 cm at the 2 m level correspond to a 3.5 cm oscillation on the 5 m level. These oscillations are peak to peak. With the closest distance between absorber and detector of 6.7 cm, this leads to a space of 4.95 cm still available between detector and oscillating absorber, which should not cause any problems.

Accuracy of the Positioning Systems

The offset between the two positioning systems as well as their absolute accuracy had to be determined. Therefore, starting with one system, the absorber was moved down in steps of 20 cm. At each stop, the position was measured with the incremental and absolute encoder as well as with a laser rangefinder for absolute position determination. In the first circles, the
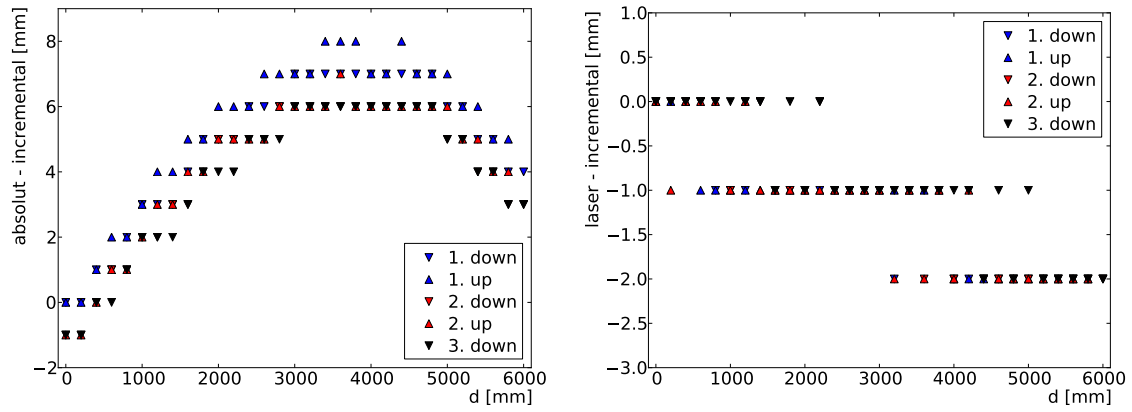
(a) Discrepancy between incremental and absolute en- (b) Discrepancy between incremental encoder and laser
coder   rangefinder

Figure 6.10: First test of the discrepancy between the different position determination
methods. The first calibration system was used. Details can be found in the text.

source was lowered down to 6 m; later to 6.5 m, before moving it up again in 20 cm steps.
Since it is expected and also verified in these tests that the incremental encoder shows the
better accuracy, it is used as the main positioning system in the calibration system.

In a first test, 2.5 cycles down to 6 m were performed. The difference between incremental
and absolute encoder showed a peak at 4 m with a discrepancy between both systems of
7 mm. The comparison of the laser rangefinder with the incremental encoder showed an
increasing discrepancy with distance up to 2 mm. Both results are shown in figure 6.10.
The position determination of the absolute encoder based on the theoretically calculated
dependency of band length versus rotation of the crank and includes a small error. It was
expected that this function had to be corrected to heterogeneous reeling of the band. The
peak at 4 m is nonetheless surprising, lacking a physical explanation. However, the data was
used to implement a correction function for the absolute encoder in the motor control unit.

After implementing the correction function, the positioning systems were tested again with
the above procedure. In the first cycle, the absorber was lowered down to 6 m, in the second
down to 6.5 m. The measurement with the laser rangefinder was done several times to
minimize errors. The results are shown in figure 6.11. The test showed a good agreement
between incremental and absolute encoder but a discrepancy in the laser measurement. The
latter can be explained by an inaccuracy of 2 μm per hole for the laser cutting of the holes
in the steel band. Thus, the distance between two holes is 4 ± 0.004 mm. This inaccuracy
can sum up over the length of the band to a measurable effect. It can be included into the
correction function for the effect of thermal expansion.

The same correction function determined for the first system was implemented in the sec-
ond and third system before testing their positioning systems according to above procedure.
Two cycles down to 6.5 m were performed with both systems; the results can be found in
figure 6.12. The difference between incremental and absolute encoder decreased with de-
creasing distance. A maximum of 16 mm (14 mm) for the second system in the first
(second) cycle and 13 mm (10 mm) for the 3rd system in the first (second) cycle was
found. Comparing the incremental encoder with the laser rangefinder, a discrepancy consis-

(a) Discrepancy between incremental and absolute encoder

(b) Discrepancy between incremental encoder and laser rangefinder

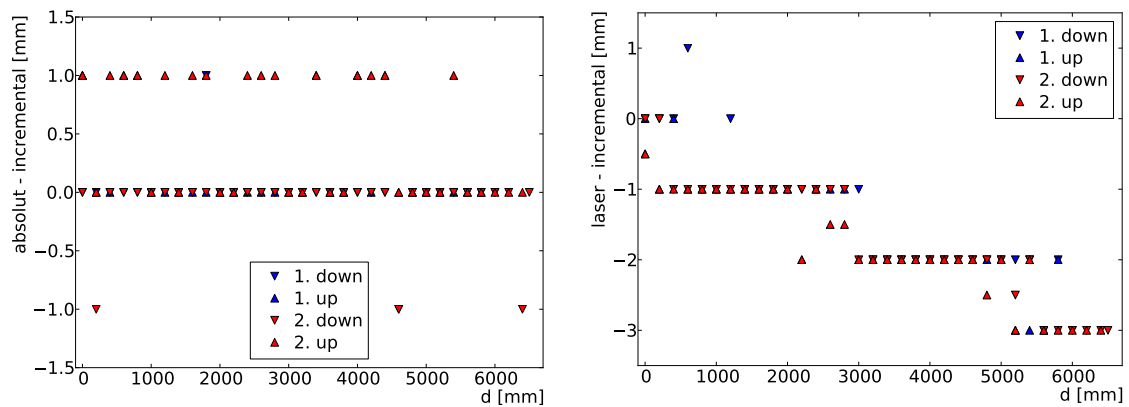**Figure 6.11:** Discrepancy between the different position determination methods after implementing the correction function for the absolute encoder. The first calibration system was used.

tent with the measurements of the first system was found. These results show two effects: First, after mounting the system for the first time, the absorber has to be lowered for several cycles, before the reeling of the band is reproducible within small errors. Second, each system needs its own correction function. Since the latter might depend also on the environment, the system was extended to the possibility to calibrate the absolute encoder also after mounting in GERDA. This calibration has to be performed once at the beginning of operation of the calibration system. After implementing individual calibration functions for the absolute encoders for the second and third system, they showed similar results as the first system.

To determine if an error accumulates over time, a series of positions was approached without initializing the system in between. Three positions were used: 2 m, 4 m, and 6 m and measurements performed with incremental and absolute encoder as well as the laser rangefinder. A total of five cycles were performed. Figure 6.13 shows the difference between incremental and absolute encoder. No error accumulation was found; the discrepancies between the different measuring methods are stable.The 2 m measurement shows a negligible discrepancy in the measured position of 1 mm; the measurements at 4 m and 6 m are stable. No difference was found if the source was approached from the top or the bottom.

The reproducibility of one position was determined moving the absorber down to 4 m and measuring the position with the incremental and absolute encoder, the laser rangefinder as well as a ruler on a guide rail installed vertically next to the band. A total of 10 cycles were performed; the results can be found in table 6.3. The measurement shows a difference between the values of the different positioning systems of up to 6 mm. Since this measurement was performed before the final calibration functions for the positioning systems were implemented, this is not surprising. The important fact is that for each positioning system the determined value is reproducible.

(a) Incremental minus absolute encoder

(b) Laser rangefinder minus incremental encoder

(c) Incremental minus absolute encoder

(d) Laser rangefinder minus incremental encoder
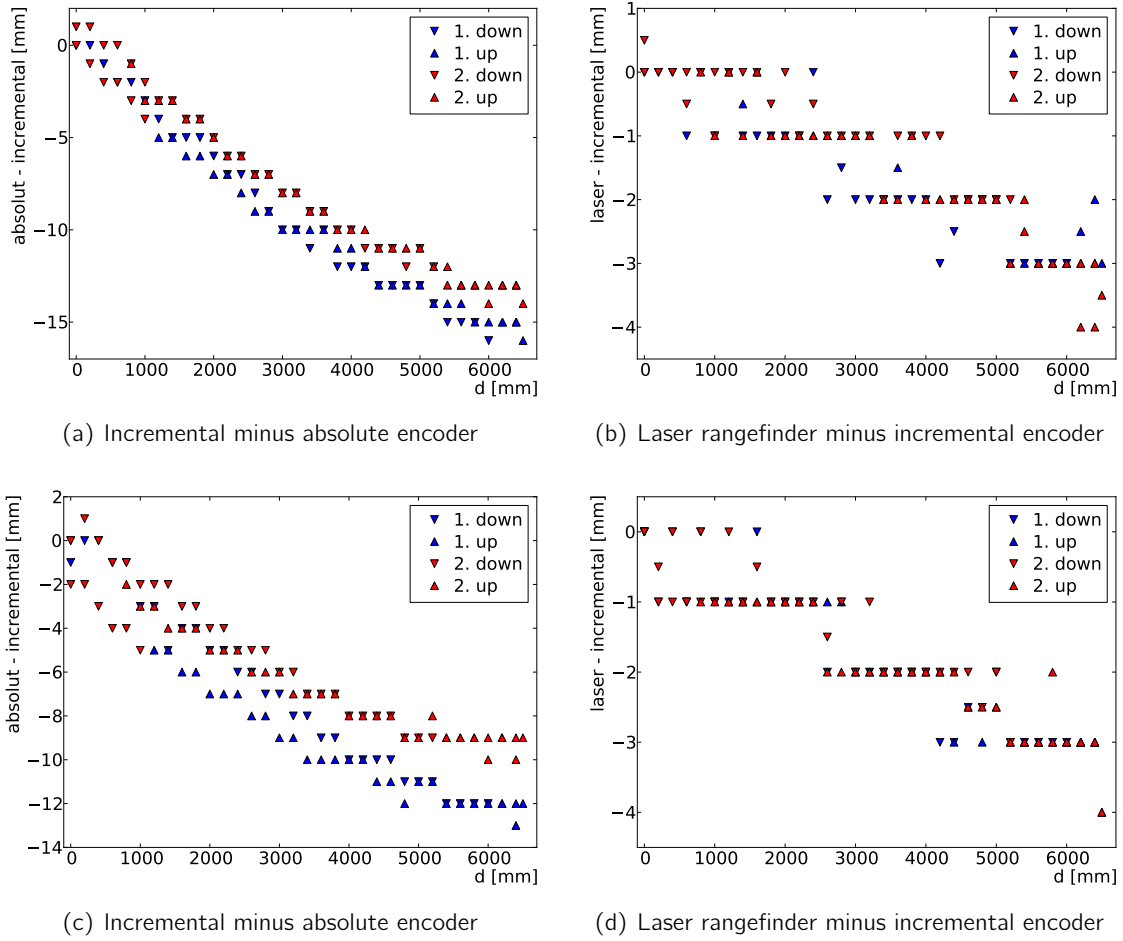
Figure 6.12: Discrepancy between the different position determination methods for the second and third system after implementing the correction function for the absolute encoder determined with the first system. The difference of incremental and absolute encoder shows in both systems a large discrepancy resulting in the necessity of individual correction functions for each system. Details can be found in the text.
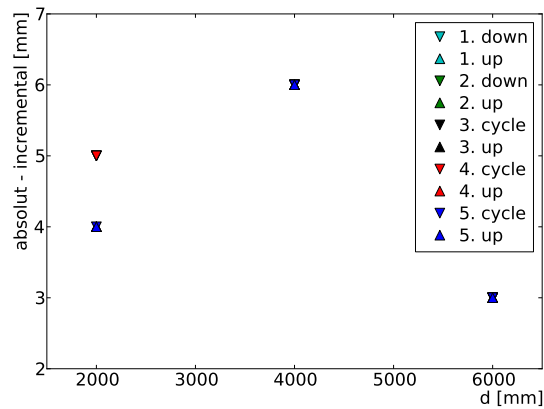
Figure 6.13: Difference between incremental and absolute encoder for three different positions showing no error accumulation over time. Since the values of the different cycles fall on top of each other, just the last are visible.

	Incremental [mm]	Absolut [mm]	Ruler [mm]	Laser [mm]
Ini pos	0 ± 0	-0.6 ± 0.5	-	0 ± 0
4 m	4000 ± 0	4006.1 ± 0.6	4002.5 ± 0.5	4001.6 ± 0.5

Table 6.3: Reproducibility of one position measured with four different methods in a total of 10 cycles.

Long Term Stability

In the last test, the sequencing implemented in the remote control for the calibration source positioning as well as the long term stability of all three systems was investigated. Two fixed waiting positions were implemented in the remote control: One is at the LAr level as described above, the second one is just before the reentry of the absorber in the pipe. The latter shall ensure a smooth procedure, although during the test phase no problems were found. At these positions, the absorber always stops, independently of the input of the user. Furthermore, the user can use predefined calibration positions and set a calibration time for each position. With such a sequence, the whole calibration run can be preprogrammed [96]. A sequence with three calibration positions down to 6 m was programmed; all three systems were used in parallel for 30 cycles. After debugging the remote control, this procedure went smoothly.

All three calibration systems were cleaned in an ultrasonic bath prior to their shipment to LNGS. A final vacuum leak test was performed with all three systems and rates of $< 10^{-7}$ mbar l/s were found. After mounting the systems in GERDA, they were lowered for several cycles down to 6 m before calibrating the absolute encoder. Last error tests were performed and the first calibration run was performed on 22 June 2011. Pictures can be found in figure 6.14. Operation of the calibration systems runs smoothly since then.

6.7 Performance of all three Calibration Systems

The performance of the calibration systems is monitored over time using the output of the calibration analysis script written by Tobias Bruch. This script uses seven lines of the ^{228}Th spectrum to determine the calibration function which is a second order polynomial. Four of these lines are monitored to determine the stability of the calibration system, namely the 583 keV line of ^{208}Tl, the 1621 keV line of ^{212}Bi, the 2615 keV line by ^{208}Tl and its single-escape peak (SEP) at 2104 keV.

Figure 6.15 shows the difference between the expected and fitted position of the SEP as well as the energy resolution of the 2615 keV line over time. Blue and grey bands mark the different runs with different configurations. The individual runs included between 2 and 11 detectors which are plotted together. The plot shows all three calibration systems: The prototype until Sep 2010, the intermediate system between Nov 2010 and May 2011 and the final system starting in June 2011.

The peak position of the SEP was found to be very stable with deviations of a maximum of ± 1 keV. The energy resolution of the 2615 keV line on the other hand shows larger deviations with σ varying between $2 - 9$ keV, especially in the time between December 2010 and May 2011. In this phase, various different tests were performed to understand the experiment and especially the background. This included the usage of different detectors
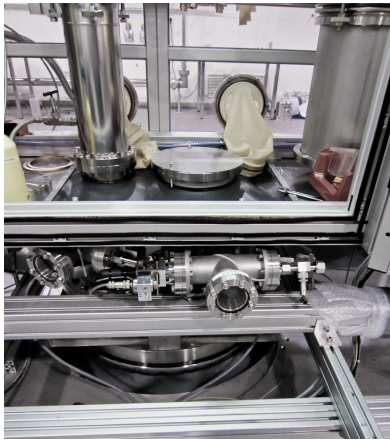
(a) System 1 and 2 mounted with the door of the glove box open, showing the 1 string arm with closed pipes and the 3 string arm prior to detector mounting.
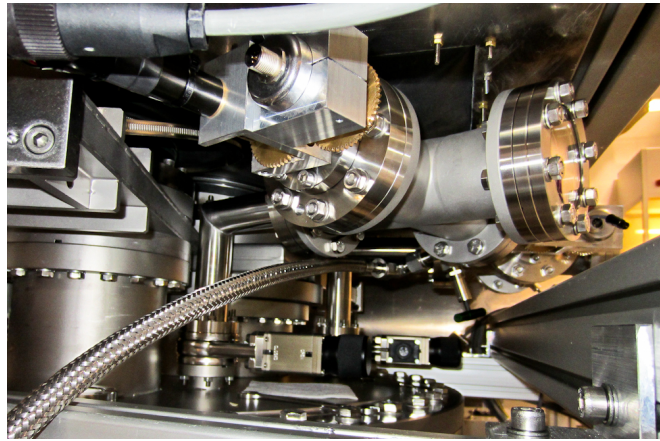
(b) Situation below the glove box. In the foreground system 1.
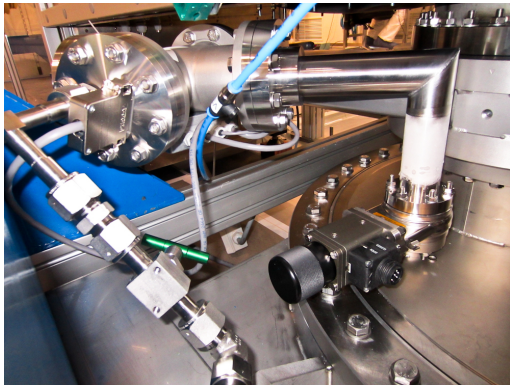
(c) System 3 just after the absorber arrived back in the parking position. The gas system is connected

(d) Situation in the clean room after mounting the final systems.

Figure 6.14: Mounting the final system at LNGS.

in different settings and configuration. Furthermore, the analysis was not yet optimized. There are two periods without calibrations runs. The first one is from September to December 2010 which is the upgrade of the prototype to the motorized version and the time after the followed accident. In this phase, background measurements with different detector configurations were still ongoing. The second is the period between mid April to end June 2011 which was a general construction break including the installation of the final calibration system. Afterwards, the analysis software was upgraded and run configuration stabilized, and with that also the energy resolution.
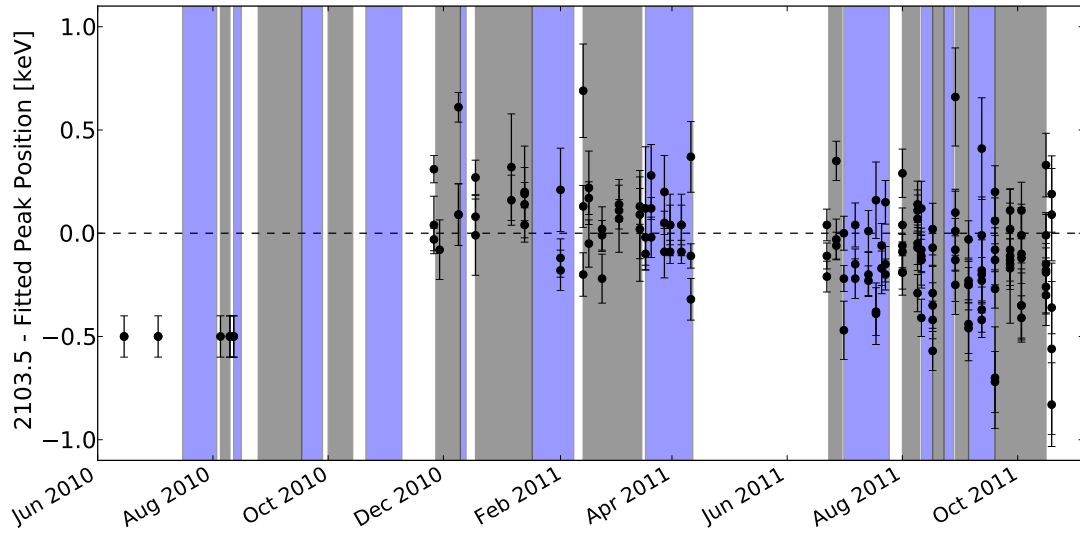
(a) Difference between expected and fitted position of the SEP over time
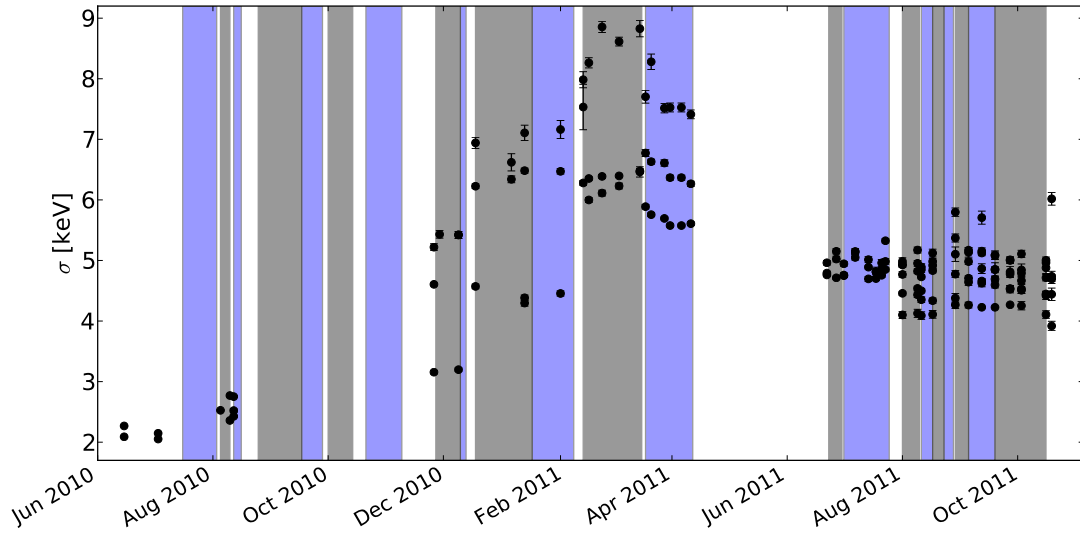
(b) Energy resolution of the 2.6 MeV peak over time

Figure 6.15: Long term stability of the calibration system during commissioning phase showing (a) the fitted SEP position over time and (b) the energy resolution of the 2.6 MeV peak. The blue and grey bands represent the different runs with different configurations. The individual runs included between 2 and 11 detectors which are plotted together. The plot shows all three calibration systems: The prototype until Sep 2010, the intermediate system between Nov 2010 and May 2011 and the final system starting in June 2011. Large variations especially in the energy resolution are due to different configurations used to investigate the background. With the installation of the final calibration system, also the analysis software was upgraded and the detectors operated under more stable conditions, leading to more stable calibration results.

6.8   Summary

The GERDA calibration system consists of three identical units to lower the calibration sources from their parking position at the top of the cryostat over several meters down to the detector array and to lift them up again after a calibration run. The sources are encapsulated in PO2 capsules which are screwed on top of a tantalum cylinder shielding the sources while in parking position. A perforated stainless steel band connects the absorber via a 90 degree deflection pulley to the crank. All these parts are vacuum certified in order be able to vacuum pump and flush with argon gas during mounting and to operate it in argon atmosphere.

The crank is turned by a motor via a rotary feedthrough. A friction clutch as well as a current limitation restrict the force from motor on the crank. The system is equipped with two independent positioning systems: The first one counts the holes in the steel band with the help of an LED on one side of the band and optical sensors on the other. The second system measures the rotation of the crank. The motor can be operated either via the motor control unit or a LabView remote control.

Extensive tests were performed prior to installation of the system,, investigating the in-fluence of oscillations as well as the accuracy of the positioning systems. Oscillations and rotations were found to be minimal with values of < 5 mm and $25 - 30$ degrees, respectively. Both are enhanced while entering the LAr due to boiling, with values up to 10 mm and rotations of $45 - 50$ degrees. After about 4 min, they were on the same level as before the immersion. Therefore, a fixed stop of 5 min just below the LAr level is implemented in the final calibration routine. The accuracy of the positioning systems was found to be ± 2 mm. The system operating three sources independently is installed in GERDA and runs stable since then.

Optimization of Signal Processing 7

As discussed in section 2.6, the energy resolution is one of the important parameters to reach the best experimental sensitivity. A good energy resolution helps to distinguish the $0\nu\beta\beta$ signal from background contributions, especially that coming from the $2\nu\beta\beta$ decay. Typical germanium detectors can reach an energy resolution of 2-3 keV at 2.6 MeV. The GERDA phase I detectors showed similar values during tests before they were installed in GERDA. It was expected that the resolution in GERDA might be slightly worse due to the long cables required for the immersion in the large GERDA cryostat.

However, the energy resolution measured during calibration runs, especially in the period between Nov 2010 and May 2011, was significantly higher (see figure 6.15). Comparing the resolution of the offline analysis of the individual pulses with those reached by electric components, the latter was significantly better. Typically, the better resolution is reached with an offline analysis. Thus, an optimization is required.

7.1 Principles of Signal Processing

The following section describes the processing of the signal produced in the germanium detectors. After a preamplification of the signal, there are two option as shown in figure 7.1: An analog approach resulting in a histogram of the amplitudes produced with a multichannel analyzer (MCA); the second approach digitizes the signal after preamplification with an analog-to-digital converter (ADC) and therefore stores the shape of the pulse for offline analysis. The shape of the pulse does not only store the deposited energy but can also be used for background identification. Since both approaches are used and compared in GERDA, both will be described.
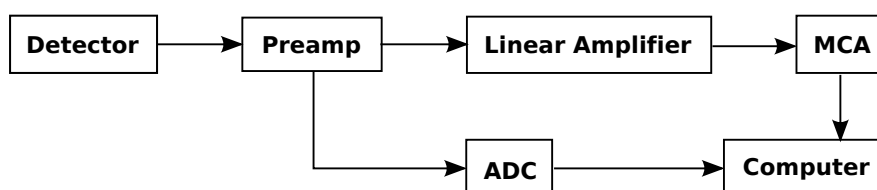
Figure 7.1: Overview of the signal processing with electric components (top arm) or digital approaches (bottom arm).
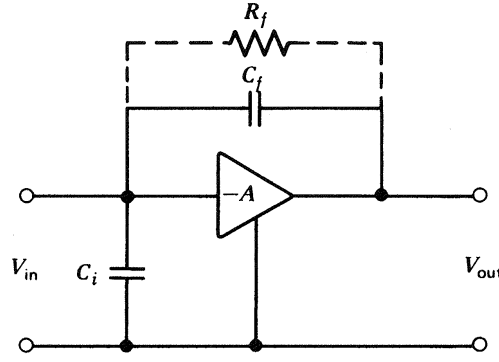
Figure 7.2: Schematic diagram of a charge-sensitive preamplifier. To discharge the capacitor C_f, a resistor R_f is usually placed in parallel with C_f. From [69].

Signal Amplification

The necessary amplification of the signal is performed in two steps: The first is a preamplifier close to the detector, the second step the main amplifier for further amplification and if desired also shaping of the pulse. Since the pulse height is the desired information, a strict proportionality between the input and the output amplitude must be preserved which is best reached with linear amplifiers.

For semiconductor detectors charge-sensitive preamplifiers are usually used, which basically integrate the charge of the incoming pulse. A circuit diagram is shown in figure 7.2. The charge Q is stored on the capacitor C_f and then removed through a resistance feedback network. The output voltage is independent of the detector capacitance:

$$V_{\text{out}} \cong -\frac{Q}{C_f} \tag{7.1}$$

An important characteristic parameter of a preamplifier is the decay time which is defined as the time required to discharge it to $1/e$ of its initial voltage and given by the capacitance and the resistance of the feedback network:

$$\tau_{\text{preamp}} \equiv R \cdot C_f \tag{7.2}$$

The decay time is adjusted to balance a complete charge collection on the one hand and a short dead time of the detector on the other. A finite decay time leads to a migration of the charge on the capacitor while it still collects the pulse, resulting in a deficit in amplitude (ballistic deficit). The charge collection time, and with it the ballistic deficit, can vary not just with the amplitude of an event, but also with its location in the detector. On the other hand, if the decay time is longer than the time between two events, the corresponding pulses will overlap (pile-up) and the amplitude information for the second pulse is distorted. An example is shown in figure 7.3. Usually, a good compromise lies in the microseconds regime.

Pulse Shaping Networks

The main amplifier not only amplifies the signal enough to match the input range of the following electronics like the MCA, but also shapes the signal. Besides its necessity for pulse height analysis, pulse shaping can reduce the rate of pile-up events with a shortening of the tail of the pulse and significantly improve the signal to noise ratio. For a given noise
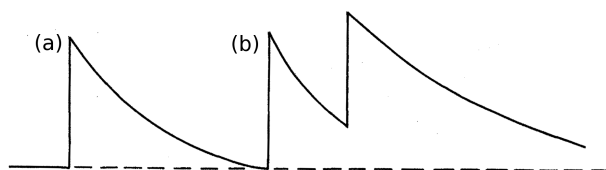
Figure 7.3: (a) Exponential tail pulse from a preamplifier. (b) Pile-up event: The
second pulse is riding on the exponential tail of the first one. From [70]

spectrum, there usually exists an optimum pulse shape in which the signal is least disturbed
by noise. Typically, a Gaussian or trapezoidal pulse shape is advantageous. Again, since the
information is stored in the maximum amplitude of the signal, it has to be preserved.

In electronic components, the shaping is performed by combinations of CR and RC net-
works. These can be understood either as differentiator and integrator or high pass and low
pass filters, respectively. Each element is again characterized by its time constant $\tau \equiv RC$
and the same considerations as for the decay time of the preamplifier have to be taken into
account when choosing its value.

Assuming approximately a step function as input signal, the output of a single differentiating
network has two major drawbacks: First, the sharply pointed top of the differentiated signal
makes pulse height analysis difficult because the maximum amplitude is maintained only for
a very short time. Second, noise mixed with the signal passes the network. This can be
considerably improved by combining the single differentiator with an integrator, separated
by an operational amplifier. In most cases, optimum signal-to-noise ratios can be obtained
with equal differentiation and integration time constants.

The signal-to-noise ratio of a CR-RC shaping circuit can be further improved if the pulse
is given a Gaussian form. An ideal Gaussian is not realizable electronically. However, an
approximate semi-Gaussian shaping can be reached with a CR-$(RC)^n$ cascade. In general,
$n = 4$ is sufficient to reach a negligible difference between the pulse and a true Gaussian.
Another advantage of Gaussian shaping compared to a CR-RC pulse is its faster return to
the baseline and therefore a reduction of pile-up events.

Digitally, a Gaussian shape can be reached with a cascade of one moving window deconvolu-
tion (MWD) and two or more moving window averages (MWA). The MWD is equivalent to
a differentiation and a pole-zero cancellation (explained in the following subsection) whereas
the MWA is equivalent to an integration. In case of Gaussian shaping, the window sizes for
the deconvolution as well as the averaging are the same.

In (large) coaxial germanium detectors, the amplitude of Gaussian shaping can vary slightly
due to ballistic deficit. In such situations, pulse shapes with a flat top are preferred since
they are less affected as can be seen in figure 7.4. Digitally, such a shape can be reached us-
ing a MWD followed by an MWA with an averaging window smaller than the deconvolution
window [106]. An analog realization is described in [107].

Baseline Restoration

Besides the phenomenon of pile-up events, there are two other effects which have an in-
fluence on the baseline relative to which the amplitude of the pulse will be measured. The
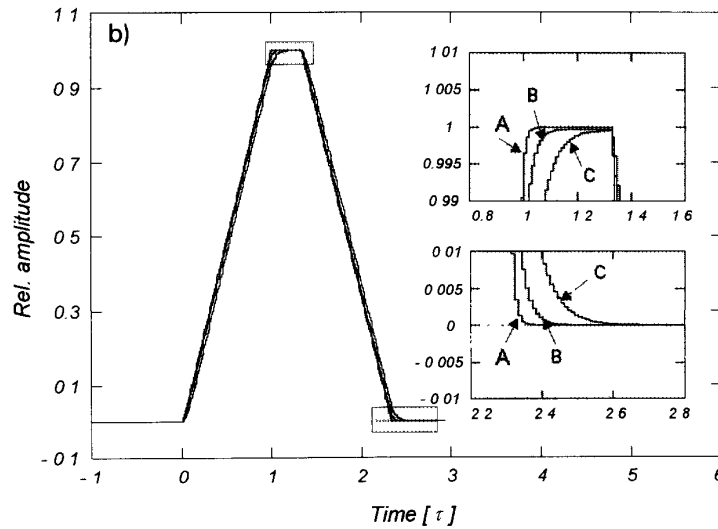
Figure 7.4: Trapezoidal shaping of three pulses arising from the same total charge but different rise times. The latter results in position dependency of the charge collection time. It increases in the sequence A, B, and C. As long as the flat top of the trapezoidal shapte is longer than the variation in rise time, the same amplitude is reached and ballistic deficit avoided.[106, 69]

first one results from the fact that the output of the preamplifier is not a perfect step function but in fact has a long but finite tail. The response of the shaping network hereon is an undershoot of the pulse which then returns back to zero with the decay time of the preamplifier. If a second pulse rides on this undershoot, an amplitude deficit arises. Such an undershoot can be corrected by a pole-zero cancellation circuit and involves adding a variable resistor in parallel with the capacitor in the CR stage. The coupling capacitance has to be large to avoid producing another undershoot with the receiving module.

With increasing count rates, the pulses begin to fall on top of each other and the small undershoots are multiplied several times. The net result are baseline fluctuations and amplitude distortions.

Increasing count rates lead to another problem. Since a capacitor cannot conduct direct current, the average output voltage of the differentiating network must be zero. Therefore, the area enclosed by the output pulse above and below the true zero must be equal leading to a shift of the baseline as shown in figure 7.5(a). Regularly spread pulses with equal amplitudes would lead to a fixed baseline shift which could easily be corrected. However, real pulses are randomly distributed with variable amplitude which leads to variable shift as shown in figure 7.5(b).

A possibility to restore the baseline electronically is to shorten the coupling capacitor to ground just after passage of the pulse. Such a baseline restorer introduces some additional noise, but usually the benefits predominate.

Digitally, the baseline can be restored averaging over a sufficiently large window and setting this value to zero. To correct for pile-up events or undershoots, it is also possible to fit an exponential function to the baseline and subtract this function from the pulse. Pile-up rejection can be performed cutting on the difference between the average value of the

(a) Regular spaced, rectangular pulses   (b) Random pulses
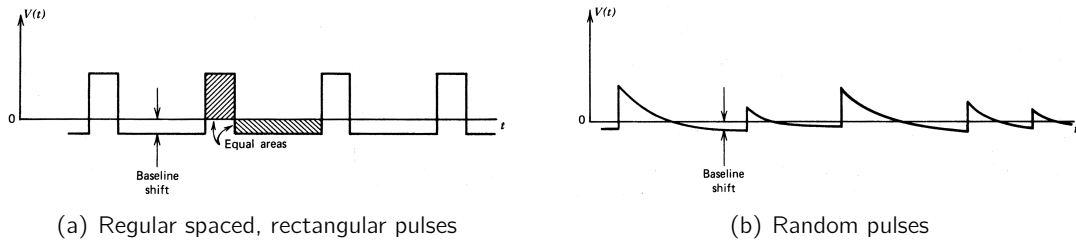
Figure 7.5: Illustrating the baseline shift in ac coupled circuits. Uniform and rectangular pulses lead to a fixed shift shown in figure (a), while randomly spread pulses with variable amplitudes cause variable shifts as shown in figure (b). From [69]

baseline at the beginning of the pulse and just before the trigger. Furthermore the baseline spread can be used to filter out high noise events.

7.2   Signal Processing in GERDA

The data analysis is performed with GELATIO [108], a software framework based on ROOT [109]. It was specially developed for GERDA, using a modular approach for the different tasks. This allows the user to easily tailor the analysis to his own needs. A basic analysis needs three different modules: The baseline restoration module, the trigger module and an energy reconstruction module which is most probably either a Gaussian reconstruction or a Gast filter. One more module called quality module is required from GELATIO v2.0 at the end of each analysis, but it is of no interest here.

Figure 7.6(a) shows a raw pulse recorded by GERDA. As can be seen, the pulse is inverted in this case which means that its amplitude deflects downwards. In the first step, the baseline restoration module checks, if the pulse is inverted or normal and corrects inverted ones such that all pulses deflect upwards in the following. To restore the baseline to zero, the module determines the average value of the baseline in a time window and subtracts this value from the entire pulse. The beginning and end point of the time window, the baseline restoration window, can be set by the user. Typically, it includes most of the recorded baseline. Figure 7.6 shows the pulse at each step of the processing of the module.

The user has the possibility to enable a pile-up correction. In this case, the baseline restoration module checks for pile-up events using the gradient of the baseline: The average value of the baseline is compared in two time windows. The first one is at the beginning of the recorded pulse, the second one just before the trigger. If the difference between both values is larger than a user defined threshold, the event is considered a pile-up and the pulse is riding on the tail of the previous one. In this case, the module fits an exponential function to the baseline restoration window using the decay time of the preamplifier provided by the user and subtracts this function from the entire pulse. Otherwise, the average baseline in the baseline restoration window is subtracted from the pulse.

The trigger module takes the output of the baseline module and implements a leading edge discriminator to determine the trigger position. For this purpose, it calculates the baseline spread of the baseline in a user given time window. The baseline spread is defined as the root mean square of the bin content in a certain time window. Multiplying it by a user given factor defines the threshold. The trigger position is then defined as the time

(a) Original Pulse

(b) Pulse after inversion

(c) Pulse after baseline restoration
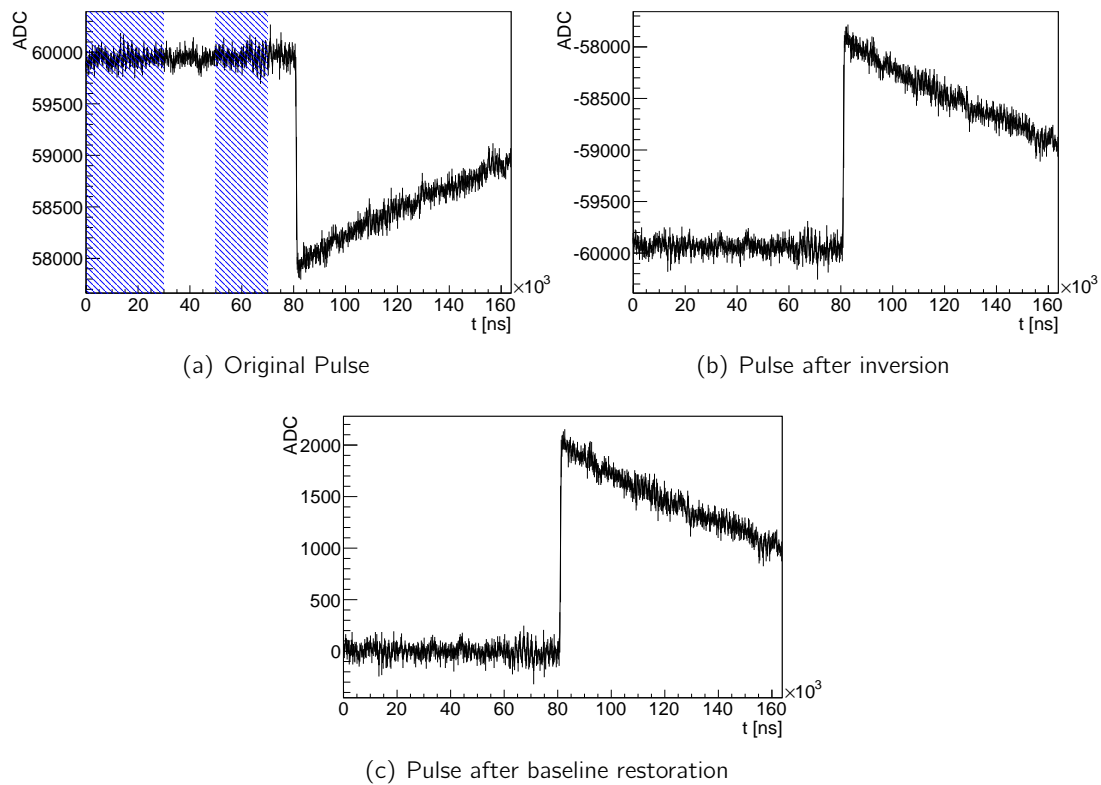
Figure 7.6: Pulse recorded by GERDA processed by the baseline restoration module of GELATIO. Shown is the effect of each transformation, the module is performing on the pulse. The blue shaded areas in figure (a) mark the two windows used to identify a pile-up event: The average value of the baseline is calculated in these windows in order to determine its gradient. Above a user defined difference between these values, the event is considered a pile-up event. Details can be found in the text.

after which the signal stayed above this threshold for a user given time. To reduce noise, the signal can be integrated using an MWA with a user defined width.

The Gaussian filter module takes as input also the output of the baseline module. It deconvolves the pulse from the exponential decay tail, differentiates it and integrated several times. For the deconvolution, the trigger position provided by the tigger module is used. Furthermore, the decay time of the preamplifier, as given by the user in the baseline module, is requested. The integration is performed using an MWA. The window width can be set by the user; it is typically the same for all integrations. Figure 7.7 shows the pulse at each step of the processing of the module. It demonstrates also, why the shaping is necessary at all: Owing to the noise of the signal, the analysis software cannot simply search for the maximum value of the pulse. The Gaussian filter does not only shape the pulse, but also filters noise, resulting in a higher precision of the determined amplitude, as it is required for this type of experiment.

The Gast filter module applies an MWD and then an MWA to the ouput of the baseline module, leading to a trapezoidal shaping. The algorithms is implemented according to [110]. The user can set the window width for both, MWD and MWA. Typically, the window width of the MWA is shorter than the one used for the MWA in order to reach a flat top.

(a) Pulse after baseline restoration

(b) Pulse after MWD

(c) Pulse after first MWA

(d) Pulse after second MWA
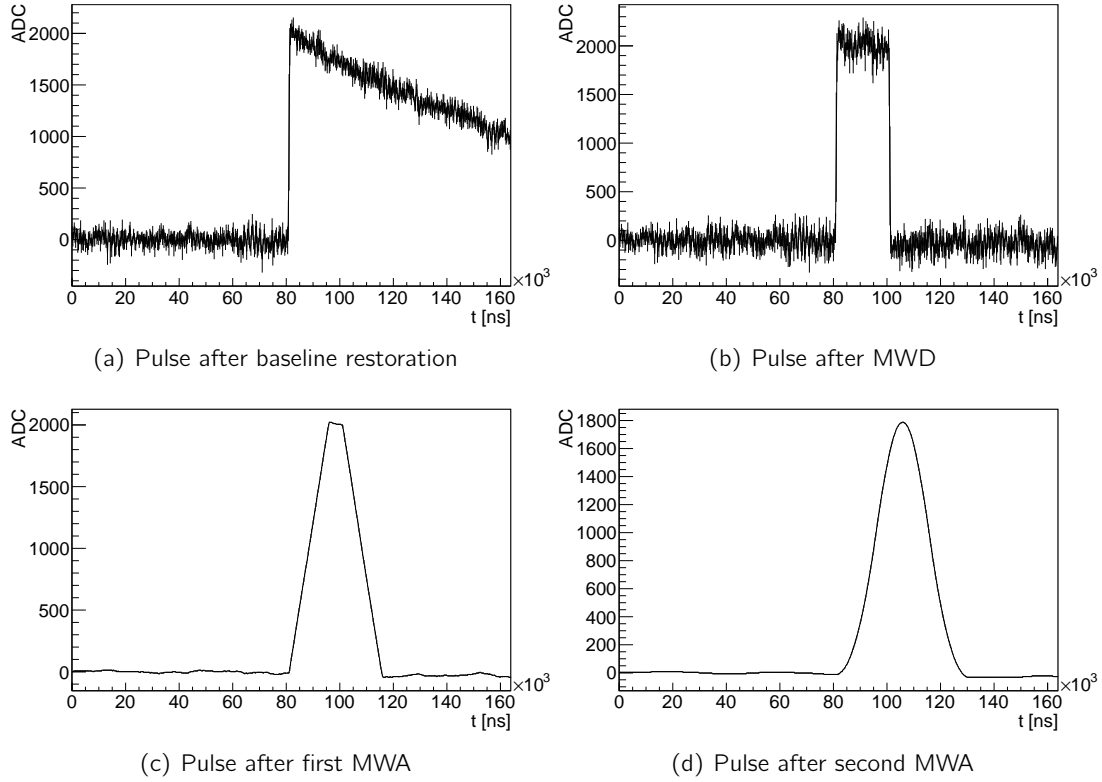
Figure 7.7: Pulse recorded by GERDA. The output of the baseline restoration module (see figure 7.6) is processed by the Gaussian filter module. Shown is the effect of each transformation, the module is performing on the pulse. Noise reduction due to the filtering can be seen during the process. Details can be found in the text.

The position on the top, where the amplitude is measured, is also given by the user. Analog to the Gaussian filter module, the Gast filter module needs the trigger position as well as the decay time of the preamplifier as provided by the trigger and the baseline module, respectively. Figure 7.8 shows the pulse at each step of the processing of the module.

The free parameters of each module had to be optimized, starting at the beginning of the analysis chain. The parameters expected to have the most impact on the energy resolution were investigated first. Calibration data from 01 August 2011 (run 16) was used in this work with a focus on the three enriched detectors included in this run, namely RG 1, ANG 4 and RG 2, from top to bottom in one string. Details on the detectors can be found in table 5.1 or [93].

GELATIO v2.0 was used. Results from this work were implemented into GELATIO v3.0 which is used since Nov 2011, which lead together with a study by Matteo Agostini on the Gaussian filter module [111] to a significant improvement of the energy resolution and comparable values with the FADC data.

7.3 Decay Time of Preamplifier

The decay time of the preamplifier τ_{preamp} enters the data analysis in two ways: The first one is the pile-up correction in the baseline restoration module, the second one is the moving

(a) Pulse after baseline restoration

(b) Pulse after MWD

(c) Pulse after first MWA
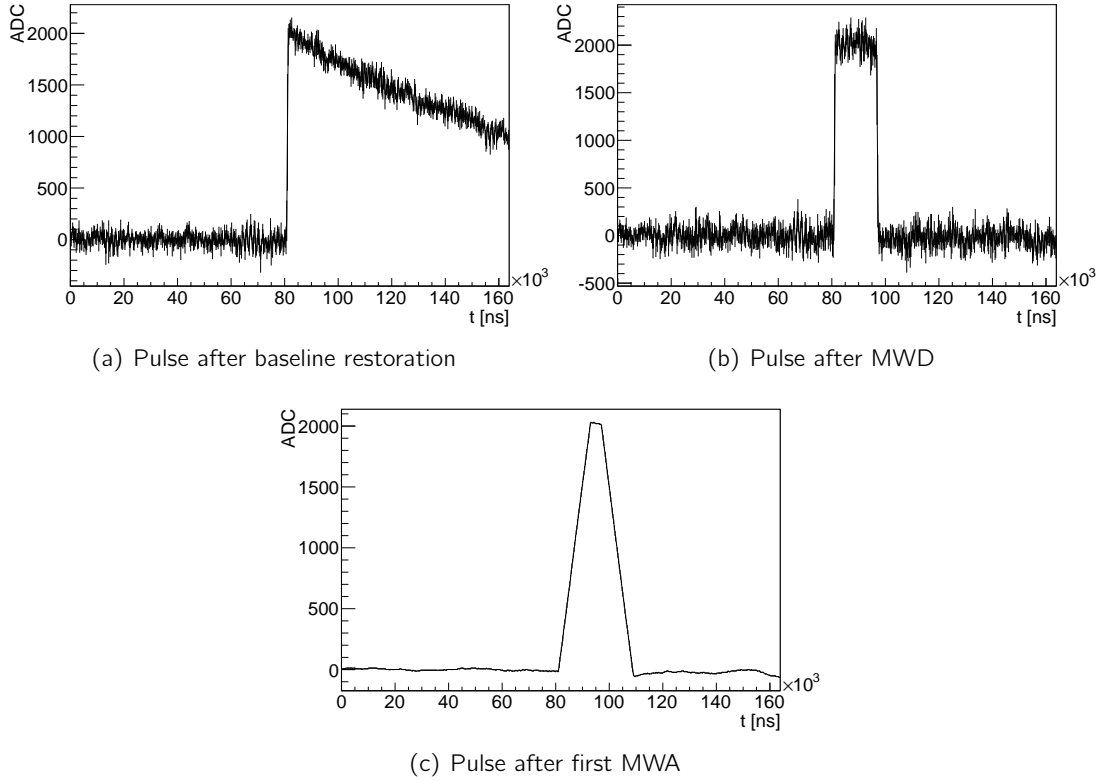
Figure 7.8: Pulse recorded by GERDA. The output of the baseline restoration module (see figure 7.6) is processed by the Gast filter module. Shown is the effect of each transformation, the module is performing on the pulse. Noise reduction due to the filtering can be seen during the process. Details can be found in the text.

window deconvolution used in both, the Gaussian as well as the Gast filter module. The first one will be explained an analyzed in detail in the following. Theoretically, τ_{preamp} can be calculated. However, it is typically just measured because it is influenced by the electronics and surroundings.

The baseline restoration module identifies pile-up events by determining the gradient of the baseline. Therefore, the average values of the baseline in two windows, one at the beginning, one at the end of the baseline, are calculated. If their differences is above a certain threshold, an exponential function using τ_{preamp} is fitted to the baseline and subtracted from the pulse. Figure 7.9 shows a pulse recorded by GERDA together with the window width of these two windows used in the analysis during commissioning phase.

Both, the Gaussian as well as the Gast filter start with the deconvolution of the pulse from its exponential tail. The required τ_{preamp} is provided by the user through the baseline restoration module and therefore identical to that used for the pile-up correction throughout one analysis.

To determine τ_{preamp}, the exponential tail of a pulse can be fitted. One such fit has a large uncertainty since the pulses recorded by GERDA have tail significantly shorter than the expected τ_{preamp}. Therefore, a large number of pulses have to be fitted and the results for τ_{preamp} are filled in a histogram. It is expected that the histogram shows a peak at
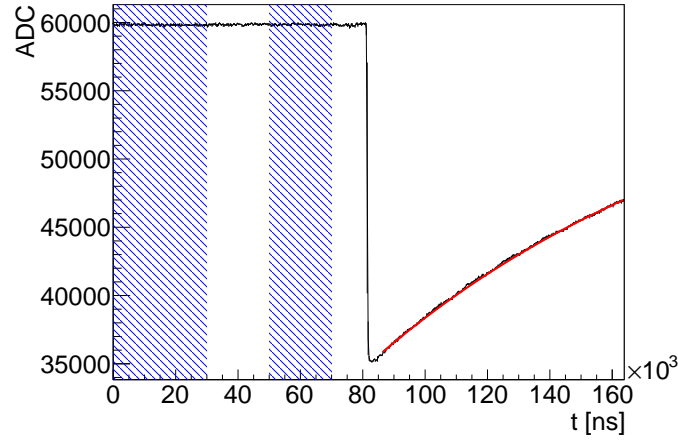
Figure 7.9: Pulse recorded by GERDA together with the performed exponential fit to the tail (red) to determine the decay time of the preamplifier. The blue shaded areas mark the two windows used to identify a pile-up event: The average value of the baseline is calculated in these windows in order to determine its gradient. Above a user defined difference between these values, the event is considered a pile-up event.

the true τ_{preamp}. This procedure has to be performed for each detector separately. If the influence of an optimized τ_{preamp} value on the energy resolution would be found to be significant in the following analysis, a calibration run with longer digitizer window might have been taken for a more precise measurement. However, it will turn out that the effect is rather minor and not worth the afford.

GELATIO provides an executable for this procedure, taking as input the relevant data files and the number of events to be analyzed. The output is a ROOT tree with one histogram for each detector. The results for 10^5 events can be found in figure 7.10. They show a second, smaller peak besides the main peak of the distribution. This second peak was found to be an artifact due to an improper fitting procedure. It is more pronounced in other runs. The positions of the main peak of each detector were found to be $\tau_{1,2,3} = 146, 154, 124$ μs and are marked in the results.

To crosscheck the results obtained by GELATIO, an independent fitting routine based on ROOT was written. The same data set was used as in the above analysis. Pulses in this run are recorded with the trigger position at 80 μs as can be seen in figure 7.9; they are inverted which means that their amplitude deflects downwards. The following fit function was used:

$$f(t) = B - A \times e^{-t/\tau_{\text{preamp}}} \tag{7.3}$$

A fixed fitting range from $t = [86, 164]$ μs was used for all pulses, which is safely after the trigger to the end of the recorded pulse. The value for the baseline B was determined for each pulse averaging over the window from $[5,70]$ μs and was than fixed for the fitting procedure. A start value for A was calculated with the following method: The midpoint of the fitting range was used and the corresponding value of the pulse determined using the bin entry at that point. Together with an initial guess for τ of 150 μs, A can be calculated. Afterwards, the fit was performed. The procedure was repeated for each pulse and a total of 2×10^4 pulses were used.

The fit results are again stored in histograms, one for each detector. The main peaks

(a) RG 1

(b) ANG 4

(c) RG 2
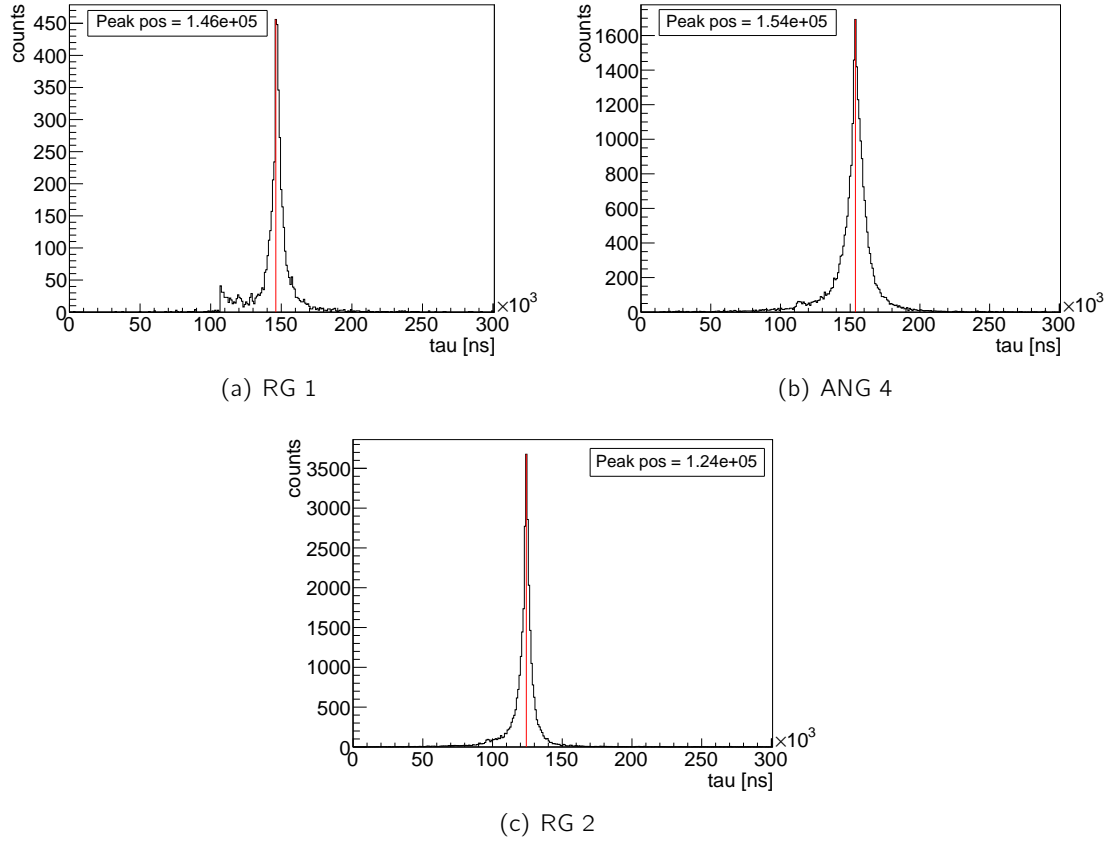
Figure 7.10: Determination of τ_{preamp} for the three enriched detectors using GELA-TIO. The exponential tail of several raw pulses was fitted and the found τ_{preamp} filled in these histograms. Marked is the peak position. The small extra peak in figure (a) is the result of a bug found in the script.

were found to be at $\tau_{1,2,3} = 146, 152, 124$ μs for the three detectors respectively. Assuming a systematic error of 2 μs this is consistent with the results from the GELATIO fit routine within the error.

However, there also appear three smaller peaks next to the main peak. The peaks at 10 μs and 400 μs are artifacts because the fit range of τ_{preamp} was limited to this range. The last peak might be due to improper fitting of pulser events but further investigations are needed. Another problem might be the fixed baseline to its average value since this value is imprecise in case of pile-up events. There is also no correction for unphysical events. However, since both fitting procedures agreed on the main peak position, the optimization process continued with these values.

The original data analysis performed prior to the optimization of τ_{preamp} in August 2011 used a mean $\tau_{\text{preamp}} = 145$ μs for all detectors. To determine the improvement gained by an optimized τ_{preamp} for each detector, the original data analysis was compared to a new one using the exact same parameters for all modules but changing τ_{preamp} for each detector to its optimized value. A Gaussian filter was used for the energy reconstruction. To insert as little systematics as possible, the resulting spectra were not calibrated and therefore, ADC channels are used instead of energy. The 2.6 MeV line of ^{208}Tl was used as a reference peak and a Gaussian function fitted to this line above linear background. The data of the

(a) RG 1

(b) ANG 4

(c) RG 2
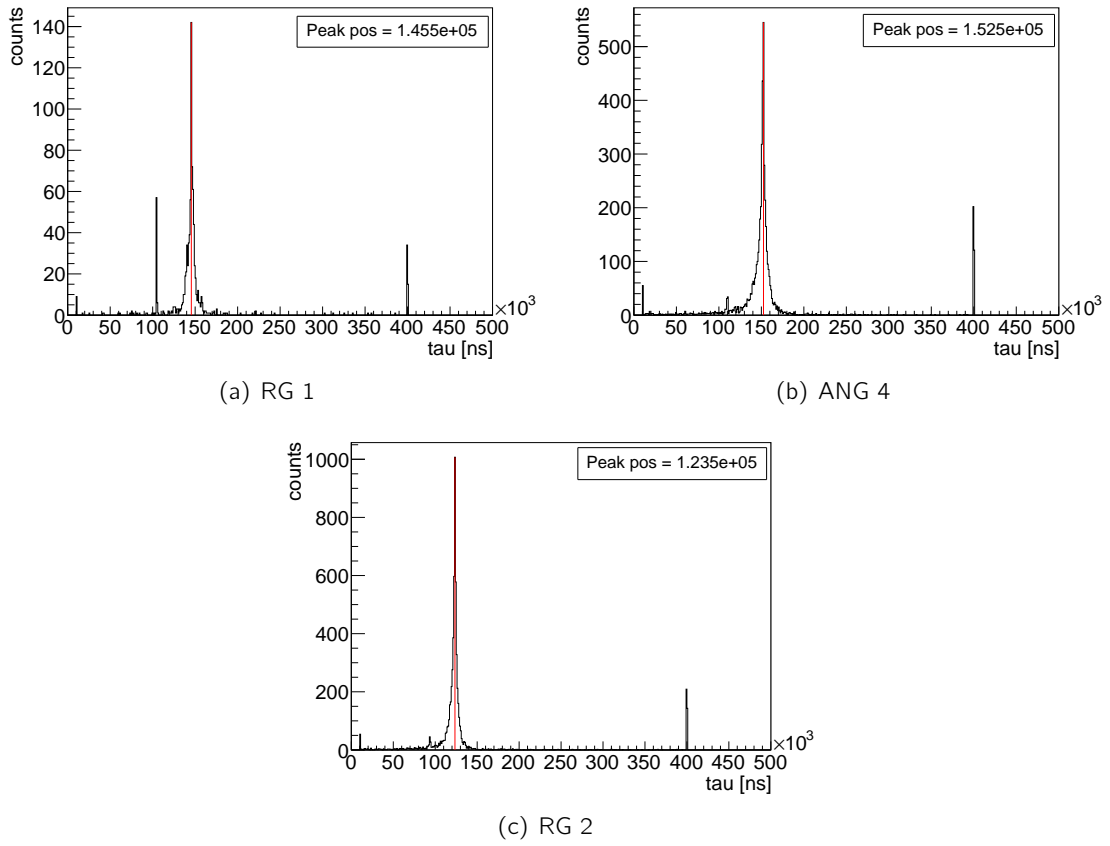
Figure 7.11: Determination of τ_{preamp} for the three enriched detectors using a self-written routine. The exponential tail of several raw pulses was fitted and the found τ_{preamp} filled in these histograms. Marked is the peak position. The extra peaks are artifacts of the the fitting procedure. Details can be found in the text.

σ [%]	RG 1	ANG 4	RG 2
Original	0.091 ± 0.001	0.092 ± 0.001	0.089 ± 0.001
This work	0.090 ± 0.001	0.092 ± 0.001	0.088 ± 0.001

Table 7.1: Comparing the original analysis with one using optimized values for τ_{preamp}. The energy resolution σ of the 2.6 MeV line was used as a reference and calculated as percentage of the peak position.

full calibration run was used.

As shown in table 7.1, the results of both analyses are the same within the errors. Therefore, an optimized τ_{preamp} for each detector is not improving the analysis in term of energy resolution. In agreement with the original analysis, a mean value can be used instead.

7.4 Baseline Restoration

To improve the baseline restoration, the influence of the exact length of the baseline restoration window as well as the pile-up correction has to be investigated. In the first step, the window width was varied and the influence on two parameters checked. The first one is again the energy resolution of the 2.6 MeV line fitting a Gaussian function above linear

background, the second one is the full width at half maximum (FWHM) of the baseline spread.

The baseline spread is useful to identify high-noise events or (improperly corrected) pile-up events. It is defined as the root mean square of the bin content in a certain time window before the trigger. The baseline spread of each pulse as provided by GELATIO is stored in a histogram. The FWHM of the resulting distribution is calculated in order to compare different analysis.

Both endpoints of the baseline restoration window were varied. For the left bound, 60, 100, 220, 480 and 1000 ns were used and for the right bound 20, 30, 45, 55 and 70 μs. The original analysis used the window between 100 ns and 30 μs. For each possible parameter combination, a separate analysis was performed and analyzed. All other parameters of the analysis modules were kept as in the original analysis to be able to compare the results and quantify the improvements. A Gaussian filter was used for the energy reconstruction.

The results are shown in figure 7.12 with the two endpoints of the baseline restoration window on the x and y axis respectively. The energy resolution or the baseline spread of each detector and analysis is than shown as color coded contours. The energy resolution shows clearly, that larger window sizes are preferred. The baseline spread on the other hand shows some favored regions whose physical origin is not obvious. The most prominent difference between the three detectors is the absolute scale for the FWHM, where ANG 4 shows significantly larger values than the other two detectors. For the energy resolution, all three detectors show similar values.

To understand this behavior, the baseline spread for one specific parameter combination was compared, namely the restoration window from 220 ns to 45 μs. Figure 7.13 shows the histograms for each detector, marking also the position with the maximum value and the determined FWHM. ANG 4 shows a well pronounced tail to higher spreads plus an overall higher count rate than the two other detectors. Therefore, a possible reason might be an insufficient pile-up correction.

To investigate this further, data analysis with and without pile-up correction but otherwise identical parameters were compared. Figure 7.14 shows the results of the 2.6 MeV line including the performed fit for ANG 4. As can be clearly seen, the tail of the peak to lower energies is more pronounced in case of no pile-up correction. However, the fact that it is still present even in case of pile-up correction might indicate that the effect is not sufficiently corrected for. Another effects might be likewise possible.

On the other hand, a comparison of the fit and the actual peak also shows, that the background model is not sufficient. In a GERDA data analysis, the peaks are usually fitted with one of two possibilities: In case of the calibration data, the analysis script written by Tobias Bruch is used to fit the relevant peaks and determine the calibration function as well as the energy resolution of the relevant peaks; otherwise, GELATIO provides a fitting routine. Both employ a smooth approximation of a step function. In case of the calibration script, the Heaviside step function is used while GELATIO uses a logistic function. Both should lead to the same results. Discussions about the usage of other fit functions are still ongoing in the collaboration.

To understand the systematic effect introduced by the fit function, the above analysis
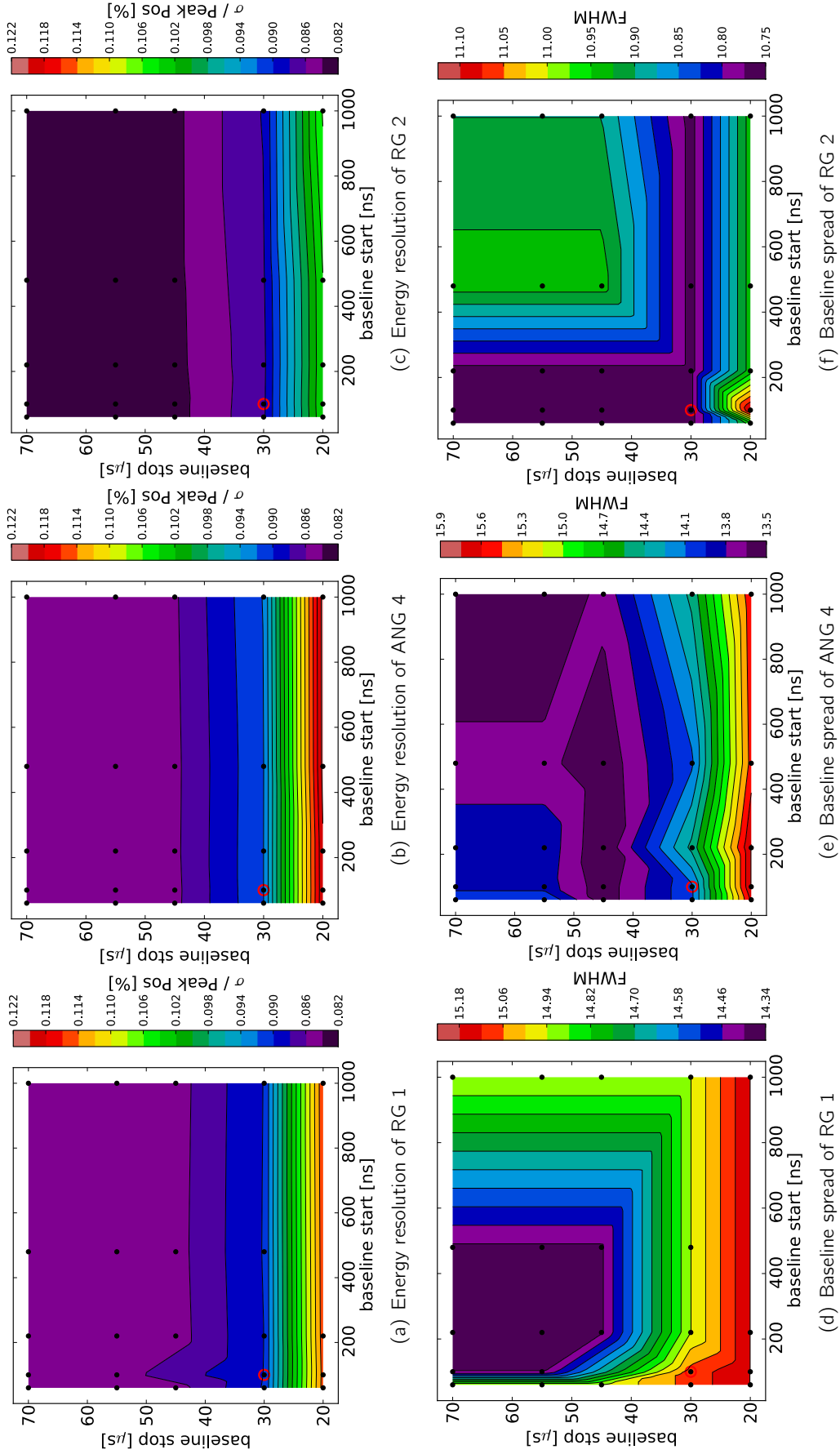
Figure 7.12: First optimization of the baseline restoration window. Both endpoints were varied in the different analysis and their values are shown on the x and y axis respectively. The resulting energy resolution of the 2.6 MeV line (top row) and the FWHM of the baseline spread (bottom row) of each detector is represented by color coded contour levels. The red circle marks the original analysis. The distribution of the energy resolution shows that larger baseline restoration windows are favored. The distribution of the baseline spread needs a more detailed investigation which can be found in the text.

(a) RG 1

(b) ANG 4

(c) RG 2
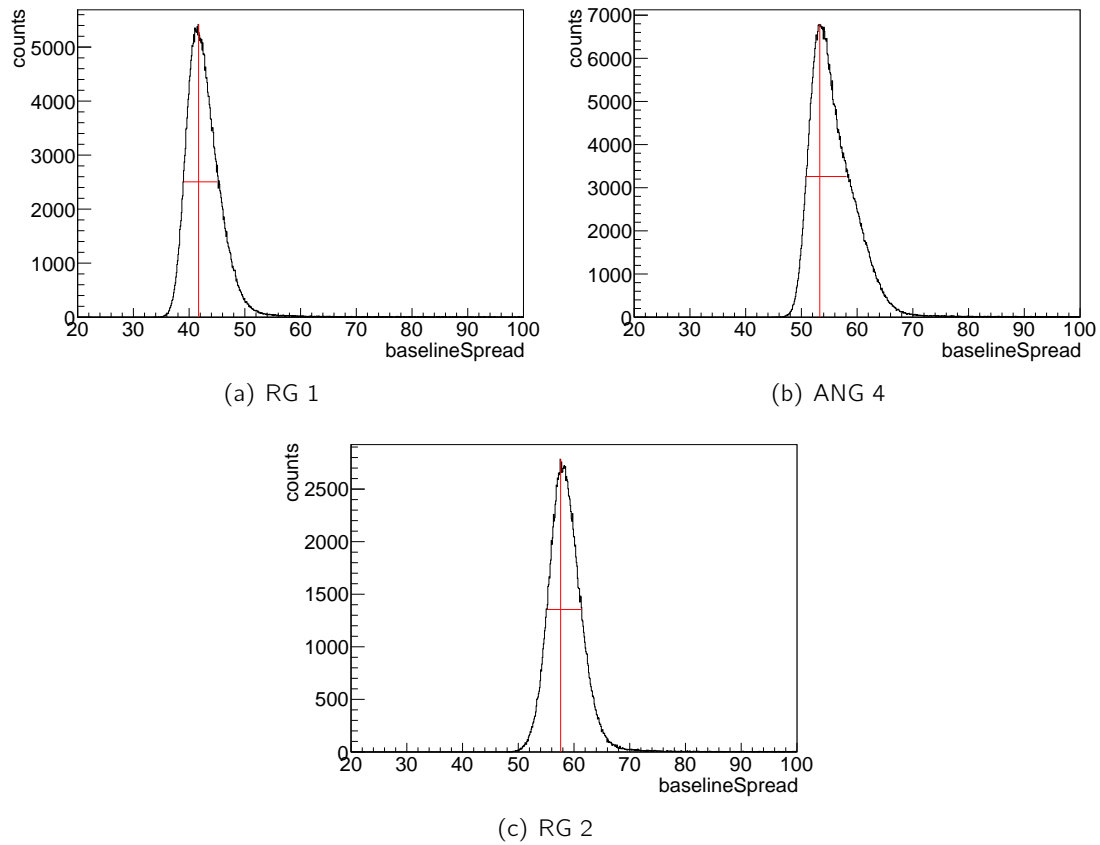
Figure 7.13: Baseline spread for the restoration window from 220 ns to 45 μs for the different detectors. The red lines mark the position with the maximum value and the determined FWHM.

of the pile-up correction was repeated using the GELATIO fit routine. The corresponding fits are also included in figure 7.14. For a more quantitative comparison, the energy resolution of all detectors was compared with and without pile-up correction for both fitting routines. Table 7.2 shows the results. The overall results are better using the GELATIO fit routine. Thus, it will be used in the following. In both cases, the energy resolution improves with pile-up correction. The effect is small but consistent in all detectors with both fitting routines. Nonetheless, even with pile-up correction there is a tail to lower energies visible comparing both fits with the data. Therefore, a cut instead of a correction of pile-up events should be defined and results of both cases compared.

σ [channels]	Linear background		GELATIO fit	
	with	without	with	without
RG 1	0.086 ± 0.001	0.091 ± 0.001	0.083 ± 0.001	0.088 ± 0.001
ANG 4	0.086 ± 0.001	0.092 ± 0.001	0.084 ± 0.001	0.090 ± 0.001
RG 2	0.083 ± 0.001	0.089 ± 0.001	0.080 ± 0.001	0.086 ± 0.001

Table 7.2: Influence of the pile-up correction on the energy resolution of the 2.6 MeV peak. Shown are the results for two different background models for the used fit. One uses a linear background while the GELATIO fit uses a smooth approximation of a step function.

(a) With pile-up correction, linear background

(b) Without pile-up correction, linear background

(c) With pile-up correction, GELATIO

(d) Without pile-up correction, GELATIO
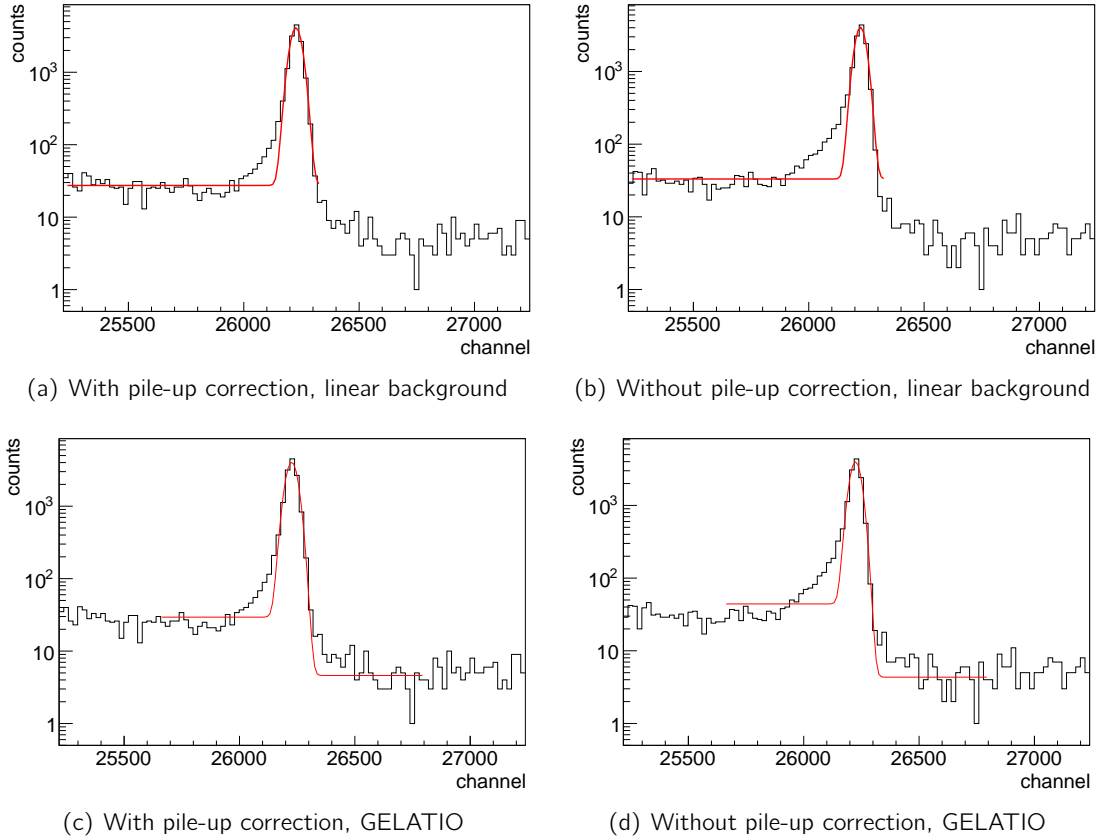
Figure 7.14: Influence of the pile-up correction on the peak shape and as a consequence the determined energy resolution. Shown are the results for ANG 4.

Therefore, a second scan through parameter space was performed, this time using as left bound for the baseline restoration window 60, 100, 220, 480, 740 and 1000 ns and for the right bound 20, 30, 40, 50, 60 and 70 μs. Again, all possible parameter combinations were used to run an independent data analysis without pile-up correction. A mean value of $\tau_{\text{preamp}} = 145$ μs was used. The pile-up correction was disabled; all other parameters were kept as in the original analysis. A possible cut is defined in the following.

To identify pile-up events, the slope of the baseline was used. GELATIO provides the average values of the baseline in a user defined window at the beginning of the pulse (1st Base) and a second window usually chosen just before the trigger (2nd Base). The difference between both values can be filled in a histogram and used to cut on pile-up events.

The distribution of the difference of the average values of both baseline windows is shown for ANG 4 in figure 7.15. A Gaussian function was fitted to the distribution and its width used to define the cut boundaries. Comparing the measured distribution with the Gaussian function, the distribution shows a small tail to negative values. This is not surprising since pulses are inverted and thus pile-up events show a negative difference between the two baseline windows when subtracting 2nd Base from 1st Base as done here.

To define the actual pile-up cut, several cut boundaries based on the width of the Gaussian function were compared. Events inside the boundaries are kept. Table 7.3 shows the influ-

	Events	σ [ch]	Base Spread
No cut	5.5 e5	22.0 ± 0.2	7.2
2σ	4.6 e5	20.6 ± 0.2	6.6
1.5σ	4.2 e5	20.5 ± 0.2	6.4
1σ	3.4 e5	20.4 ± 0.2	6.6
1σ N	4.2 e5	20.6 ± 0.2	6.6
0.5σ N	3.5 e5	20.7 ± 0.2	6.6

Table 7.3: Comparison of different boundaries for the pile-up cut. The effect on the energy resolution as well as the baseline spread is shown together with the event loss due to the cut. Entries marked with 'N' just cut the negative side but leave the positive untouched.

ence of the different cut boundaries on the energy resolution as well as the baseline spread together with the event lost due to the cut. Since the pile-up events are expected to have negative values, the option to just cut on the negative side but leave to positive uncut, is investigated. This reduces the event loss which might improve the fit error due to better statistics. Figure 7.16 shows the effect on the 2.6 MeV peak as well as the baseline spread.

Table 7.3 shows, that the biggest improvement is from no cut to the cut on the 2σ range. The exact cut width, however, has no effect on the determined values. This can be understood comparing the plots in figure 7.16. The shape of the 2.6 MeV peak used to determine the energy resolution show an obvious improvement visible in a decreasing tail to lower energies with more strict cuts. Since the Gaussian fitted to the peak does not describe this tail well, it does not change significantly with the different cut widths. Therefore, either another fit function should be used which considers the tail properly, or the cut parameter should be defined on a visible check that fit function and peak shape are in reasonable agreement. The latter will be performed in the following.

The baseline spread shows a similar phenomenon. The introduction of a pile-up cut improves the range independent of the actual cut range. However, the overall asymmetry of the distribution does not change with a stronger cut. Therefore, pile-up events just partly explain the width and especially the asymmetry of the distribution. Further investigations
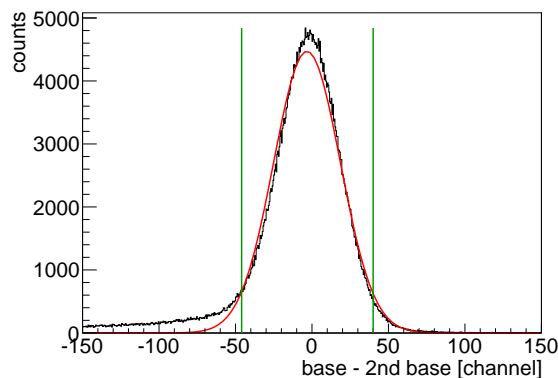
Figure 7.15: Difference between the average baseline in a window at the beginning of the pulse and one just before the trigger. A Gaussian function was fitted to the distribution to define a possible pile-up cut. Shown here are the cut boundaries on 2σ of the Gauss.

(a) 2.6 MeV peak, no cut

(b) Baseline Spread, no cut

(c) 2.6 MeV peak, 2σ

(d) Baseline Spread, 2σ

(e) 2.6 MeV peak, 1σ

(f) Baseline Spread, 1σ

(g) 2.6 MeV peak, 0.5σ L

(h) Baseline Spread, 0.5σ N
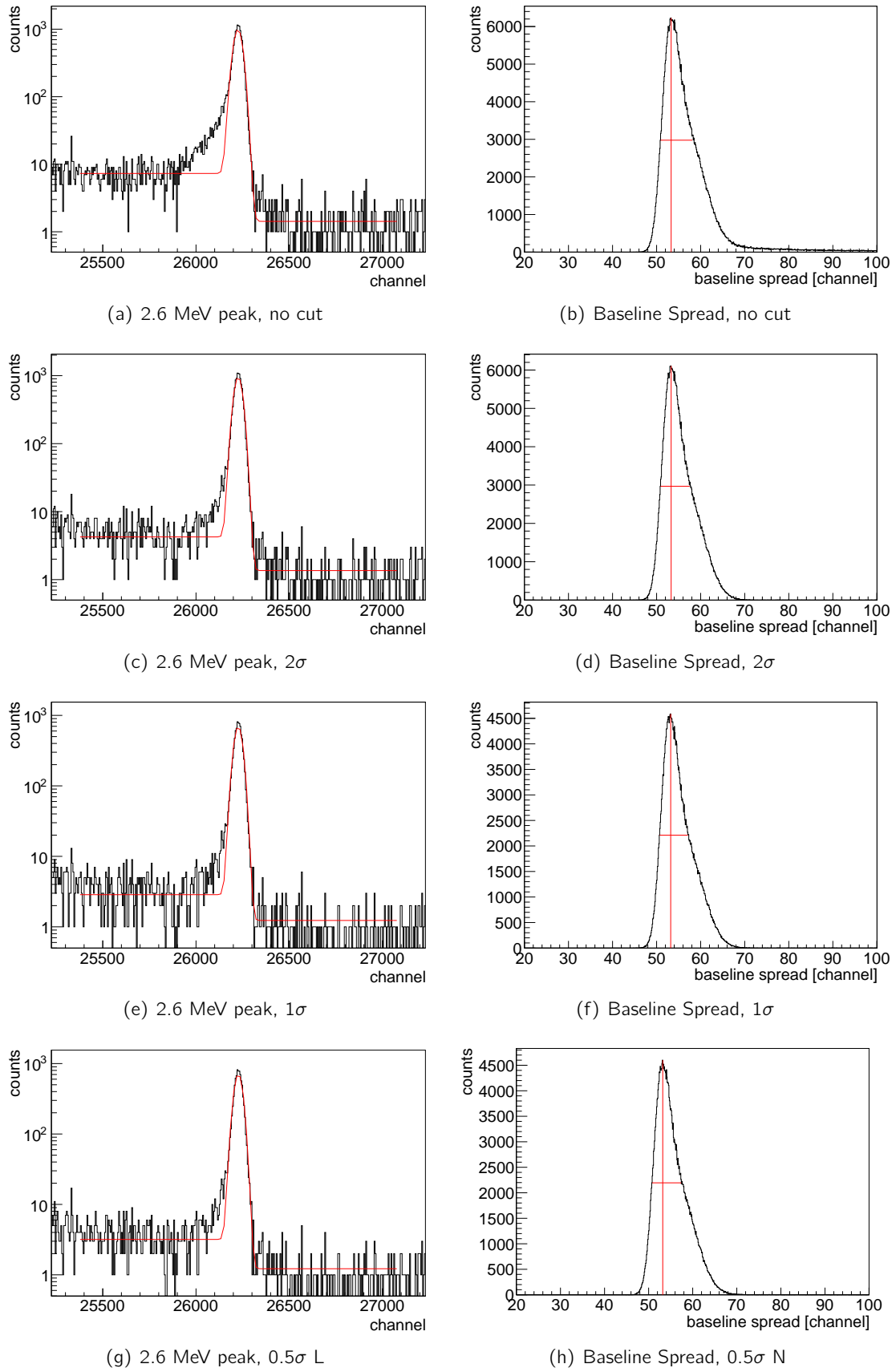
Figure 7.16: Effect of different pile-up cut ranges on the energy resolution of the 2.6 MeV peak (left column) and the baseline spread (right column). A quantitative comparison can be found in table 7.3.

including also possible origins and reduction of noise would be necessary for a deeper understanding.

A stronger cut reduces the overall number of events. With reduced statistics it becomes more and more difficult to get a stable fit with the same parameters for all performed data analysis. The latter is necessary to be able to compare their results without introducing systematic effects. The smallest cut range providing stable fit results is a pile-up cut on 0.75σ on the negative side leaving the positive side uncut. This cut also shows a reasonable agreement between data and fit necessary for a meaningful analysis. Therefore, this setting was used for the comparison of the different baseline restoration window widths.

It was found that the baseline spread shows exactly one width for all data analyses per detector, namely 5.9 ± 0.2 channels for RG 1, 6.6 ± 0.2 channels for ANG 4 and 5.9 ± 0.2 channels for RG 2. This is an overall improvement compared to the first analysis with pile-up correction, where the baseline spread varied between $6.0-6.3$ channels in case of RG 1, $7.1-8.4$ channels in case of ANG 4 and $6.2-6.4$ channels in case of RG 2. This indicates that the baseline spread is independent of the baseline restoration window width after a proper pile-up cut.

The distribution of the energy resolution of the 2.6 MeV peak is shown in figure 7.17. There are some features in the distribution especially in the case of RG 1 which are not understood yet. It is for example not clear why the best energy resolution was found for a baseline restoration starting at either 60, 100 or 220 ns and stopping at 40μs. Physically, a longer window should provide better results as can be found for the two other detectors. Therefore, further investigations are necessary to fully understand the distribution. However, an an overall improvement compared to the first analysis was found, where the resolution varied between $\sigma/\text{peak pos} = 0.082-0.122$ % while it now varies just between $0.077-0.079$ % with a statistical error of 10^{-5} %. An overall improvement compared to the original analysis of 13.6 % in case of RG 1 as well as RG 2 and 14.8% in case of ANG 4 could be reached.

7.5   Summary and Outlook

An optimization of the data analysis chain and its parameters is necessary to reach to best energy resolution possible. Therefore, the influence of different parameters on the energy resolution as well as the pulse shape itself was investigated. It was found, that the exact value of the decay time of the preamplifier τ_{preamp}, used for pile-up correction as well as the moving window deconvolution of the Gaussian as well as trapezoidal shaping, has only a minor effect and a mean value of $\tau_{\text{preamp}} = 145$ μs can be used instead.

The used window for the baseline reconstruction needs to be 40-50 μs, with a preference to longer windows. Since pile-up events just appear in case of calibration data, a cut based on the slope of the baseline was found to be more efficient than a correction. An overall improvement compared to the original analysis of 13.6 % in case of RG 1 as well as RG 2 and 14.8% in case of ANG 4 could be reached.

In the latest version of the analysis software used by the GERDA collaboration, the Gaussian filter was revised, allowing the user to define the number of used MWA. It was found, that a larger number of MWA of the order of 10 leads to better results in terms of energy

(a) RG 1

(b) ANG 4

(c) RG 2
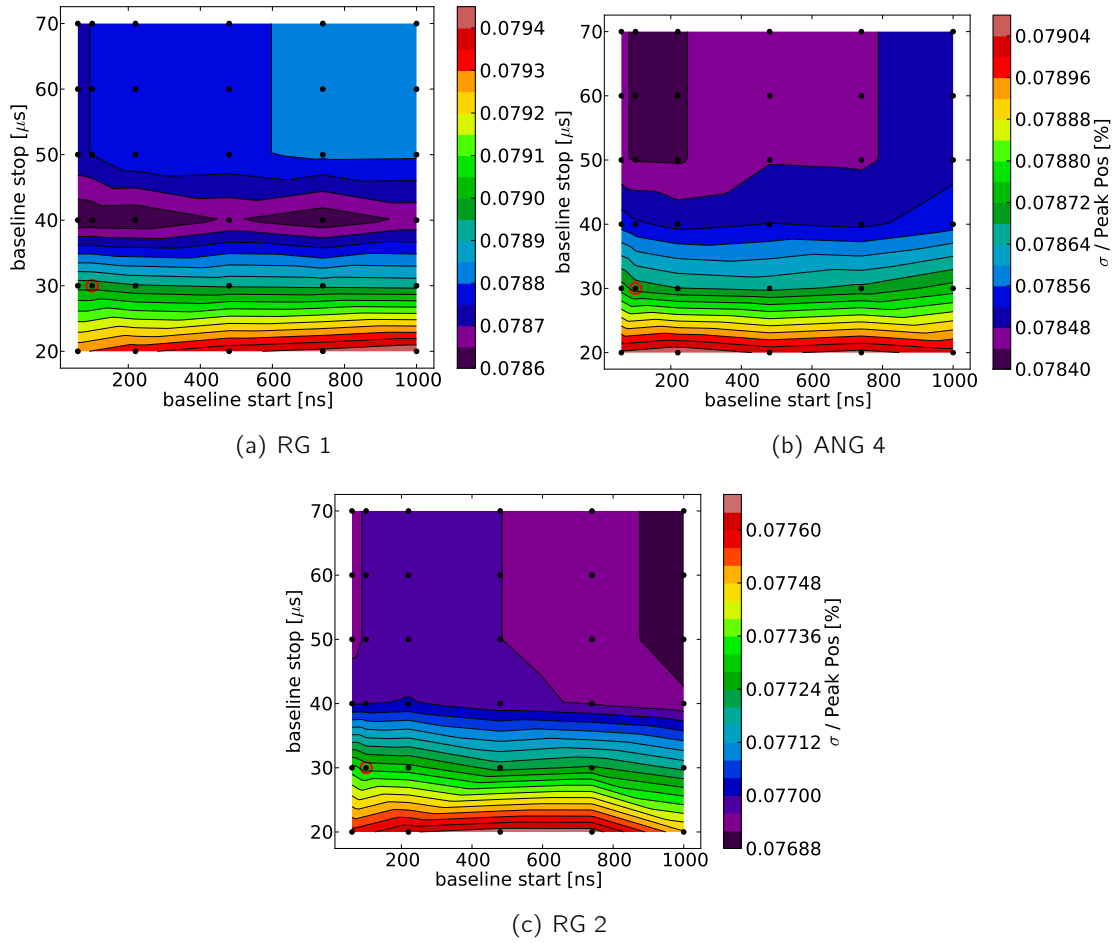
Figure 7.17: Second optimization of the baseline restoration window. Both endpoints were varied in the different analysis and their values are shown on the *x* and *y* axis respectively. A cut on pile-up events was performed; details can be found in the text. The resulting energy resolution of the 2.6 MeV line of each detector is represented by color coded contour levels. The red circle marks the original analysis.

resolution [111].

Besides the studied parameters, the trigger efficiency of the trigger module as well as the parameters of Gaussian and Gast filter should be investigated in the future. Especially the Gast filter, which is suppose to show the best energy resolution for this type of detectors, need a thorough analysis. An investigation on possibilities to reduce noise might be an asset.

Conclusion and Outlook 8

Neutrinoless double beta decay is a very powerful tool to understand the nature of neutrinos and measure their masses. The GERmanium Detector Array, GERDA, searches for this decay with germanium detectors enriched in the double beta decaying isotope ^{76}Ge. It is located at Laboratori Nazionali del Gran Sasso (LNGS) in Italy, where 3100 mwe (equivalent vertical depth relative to a flat overburden) of rock shield the experiment from cosmic radiation. To reach the necessary low background, the detectors are submerged nakedly into the liquid argon. The argon acts simultaneously as cooling liquid as well as shielding material for the detectors. The argon cryostat is surrounded by a 10 m diameter water Cerenkov veto, which further shields the detectors.

During the first phase of the experiment, which started in November 2011, a total of eight closed-ended, coaxial detectors enriched in ^{76}Ge together with four natural germanium detectors are used. They are arranged in four detectors strings with three detectors per string. A total of 17.7 kg of germanium is reached. The goal is to improve current limits on the $0\nu\beta\beta$ sensitivity in only a year of data taking with an exposure of 15 kg·y and a background of 10^2 counts/(keV·kg·y). In case no events will be observed above background, a half life limit of $T_{1/2} > 2.2 \times 10^{25}$ y can be established, resulting in an upper limit for the effective neutrino mass of $m_{ee} < 0.23 - 0.39$ eV.

Phase II will use in addition newly developed broad-energy germanium detectors enriched in ^{76}Ge, leading to a total mass of about 40 kg. An further improvement of the background by one order of magnitude compared to phase I is planned, which leads with an aimed exposure of 100 kg·y to a half life sensitivity of $T_{1/2} > 15 \times 10^{25}$ y and a corresponding effective neutrino mass of $m_{ee} < 0.09 - 0.15$ eV.

The aim of this work was the development of the calibration system for the commissioning as well as the first phase of the experiment. Radioactive sources will be used for an energy as well as a pulse shape calibration with a calibration run once a week. During physics runs, the sources are parked at the top of the cryostat.

In the first step, Monte Carlo Simulations were used to determine the relevant parameters of calibration system, such as type and activity of the used sources, the required number of sources as well as their optimum position. It was found that three ^{228}Th sources placed in the horizontal plane as close as possible to the detectors to prevent scattering of the γ's in the liquid argon are necessary for a successful calibration. In the vertical direction, two positions between the detector layers are necessary to reach sufficient statistics in each detector. The three sources used in the experiment have an activity of 13.1 kBq, 9.3 kBq

and 13.0 kBq at the start of GERDA's phase I, which was at 01 Nov 2011. With this activity, a successful calibration can be performed in about half an hour per position. Two of these sources are custom made to lower their neutron yield.

Since the experiment aims for the lowest possible background in the region of interest, the contribution from the calibration sources is important to determine. With the sources in parking position, the detectors are shielded by 3 m of liquid argon from the radiation of the sources. A further reduction of the background was reached by the installation of 6 cm of tantalum just below the calibration sources. Both, γ as well as neutron radiation as result of (α,n) reactions in the capsule of the sources were considered and a total background contribution of

$$B_{\text{top}} = (1.52 \pm 0.01(\text{stat}) \, {}^{+0.16}_{-0.23}(\text{sys})) \times 10^{-4} \text{ counts/(keV·kg·y)} \qquad (8.1)$$

was found. This is well below the background goal of phase I.

During an accident in September 2010 one of the calibration sources with an activity of 22.3 kBq at 01 Nov 2011 fell into the cryostat and has to be taken into account as well. It contribute with a total of

$$B_{\text{bottom}} = (11.25 \pm 0.10(\text{stat}) \, {}^{+0.99}_{-1.01}(\text{sys})) \times 10^{-4} \text{ counts/(keV·kg·y)} \, . \qquad (8.2)$$

Although this value is significantly higher than the background from the top sources it was decided that the source can stay inside the cryostat for GERDA's phase I.

In the next step, the hardware necessary to lower the calibration sources from their parking position over several meters down to the detector had to be designed, built, tested and installed at the experiment. Three identical units, one for each source, are used for this purpose.

The capsule of the source is screwed on top of a tantalum cylinder required for the shielding of the source. A perforated stainless steel band connects the absorber via a 90 degree deflection pulley to the crank. All these parts are vacuum certified in order be able to vacuum pump and flush with argon gas during mounting and to operate it in argon atmosphere. The crank is turned by a motor via a rotary feedthrough. A friction clutch as well as a current limitation restrict the force from the motor on the crank. The system is equipped with two independent positioning systems: The first one counts the holes in the steel band with the help of an LED on one side of the band and optical sensors on the other. The second system measures the rotation of the crank. The motor can be operated either via the motor control unit or a LabView remote control.

Extensive tests were performed prior to installation of the system, investigating the influence of oscillations as well as the accuracy of the positioning systems. Oscillations and rotations were found to be minimal with values of < 5 mm and $25-30$ degrees, respectively. Both are enhanced while entering the LAr due to boiling, with values up to 10 mm and rotations of $45-50$ degrees. After about 4 min, they were on the same level as before the immersion. Therefore, a fixed stop of 5 min just below the LAr level is implemented in the final calibration routine. The accuracy of the positioning systems was found to be ± 2 mm. The final system operating three sources independently was installed in GERDA in June 2011 and runs stable since then. A good agreement of first data with Monte Carlo simulations was found.

The energy resolution of the detectors measured during calibration runs, especially in the period between Nov 2010 and May 2011, was significantly higher than expected from previous measurements outside GERDA. Thus an optimization of the offline data analysis was required. The data analysis is performed with GELATIO, a software framework based on ROOT. It was specially developed for GERDA, using a modular approach for the different tasks. This work mainly focused on the first module, the baseline restoration module. The parameters expected to have the biggest impact on the energy resolution were investigated.

It was found, that the exact value of the decay time of the preamplifier τ_{preamp}, used for pile-up correction as well as the moving window deconvolution of the Gaussian as well as trapezoidal shaping, has only a minor effect and a mean value of $\tau_{\mathrm{preamp}} = 145$ μs can be used instead.

The used window for the baseline reconstruction needs to be 40-50 μs, with a preference to longer windows. Since pile-up events just appear in case of calibration data, a cut based on the slope of the baseline was found to be more efficient than a correction. An overall improvement compared to the original analysis of 13.6 % in case of RG 1 as well as RG 2 and 14.8% in case of ANG 4 could be reached. Future projects could extend this work to other modules used in the analysis chain.

Technical Drawings A

For completeness all technical drawings relevant for the calibration system. The originator is marked in the caption.
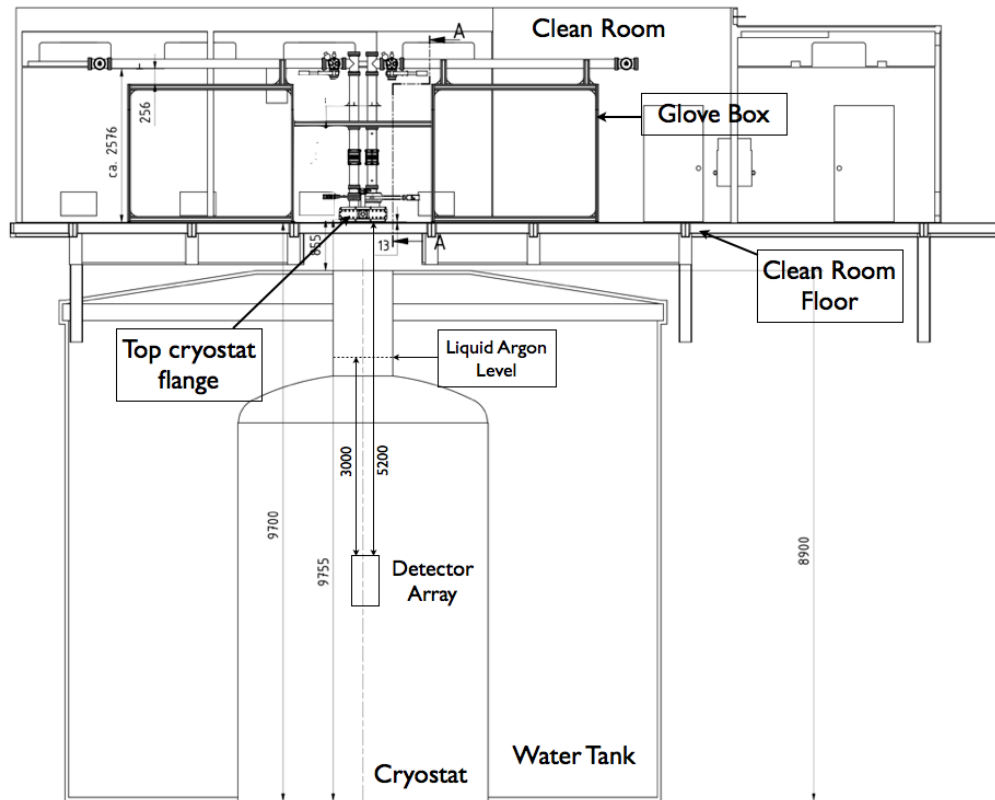
Figure A.1: Visualization of the GERDA experiment labeling the most important parts. Drawing provided by MPI Heidelberg and Alfredo D. Ferella.
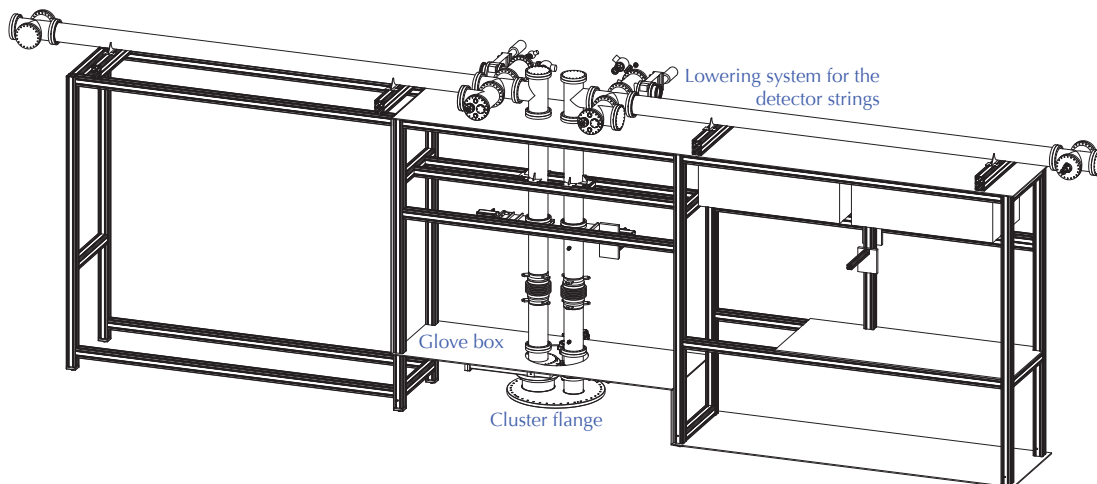
Figure A.2: Technical drawing of the lowering system for the detector array. The support structure for the lowering system also houses the glove box necessary for the detector handling. Drawing provided by MPI Heidelberg.
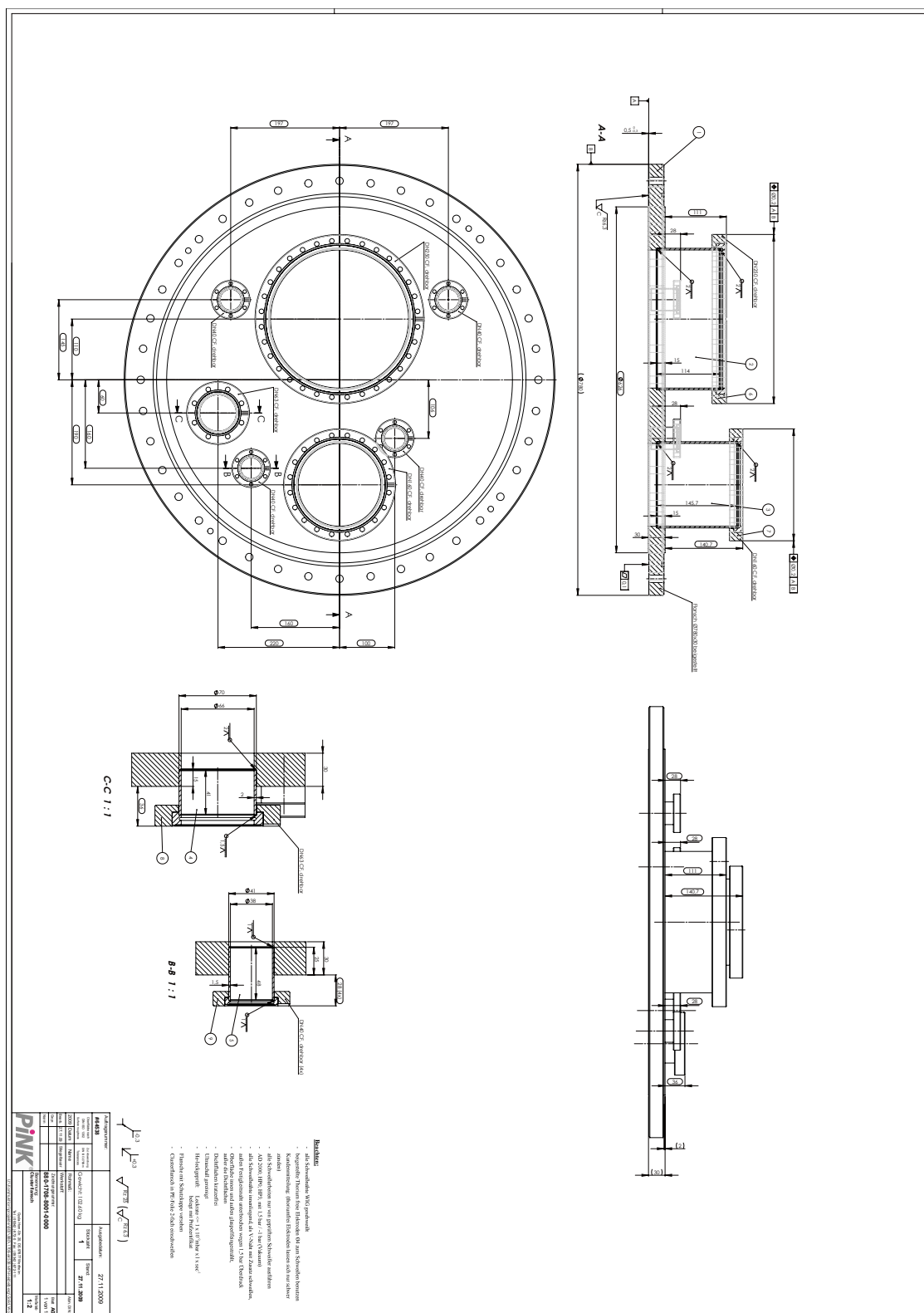
Figure A.3: Technical drawing of the cluster flange as provided by MPI Heidelberg.
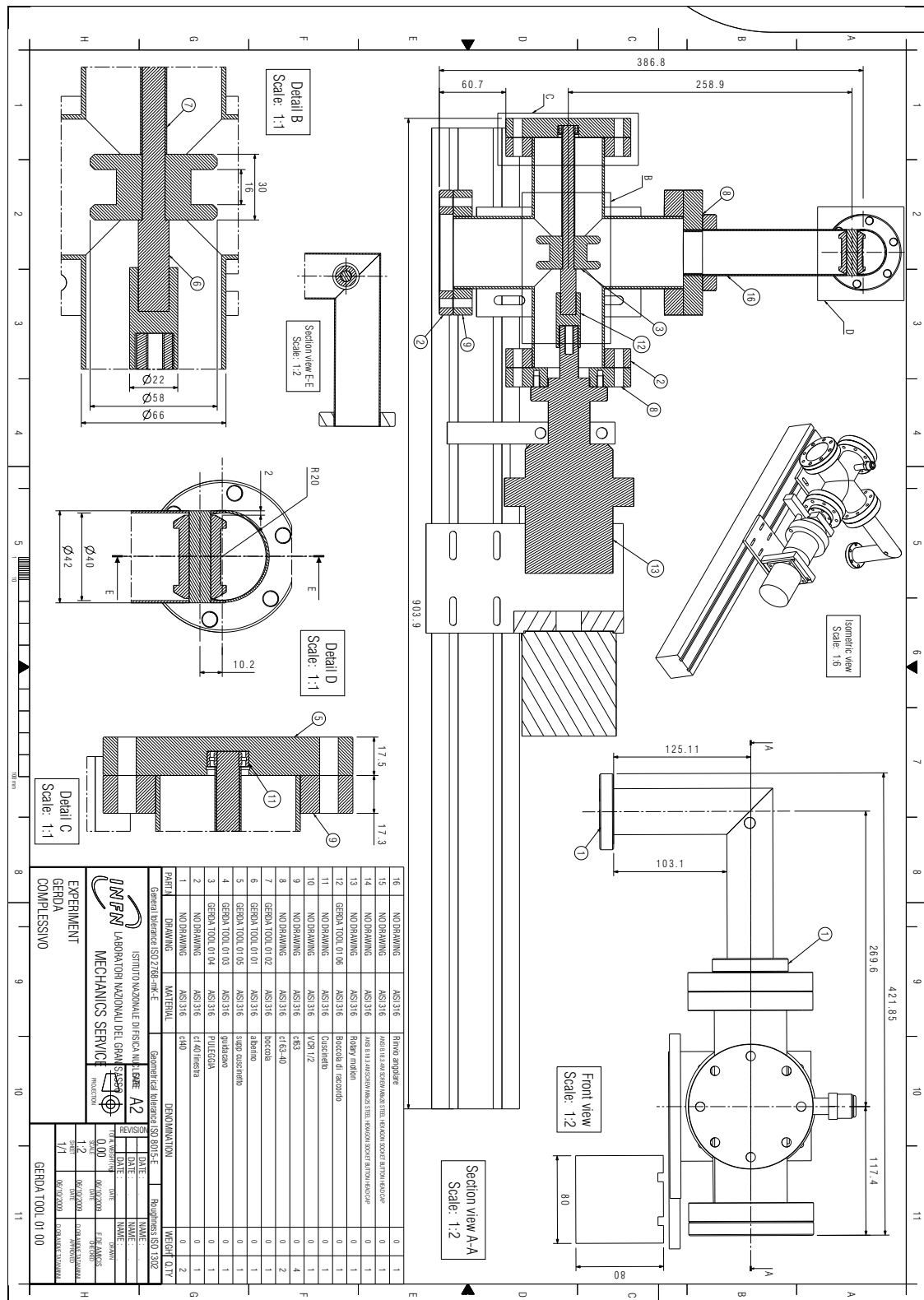
Figure A.4: Technical drawing of the prototype calibration system as provided by LNGS.

Vorderansicht
Maßstab: 1:2

30.1

52.13

52.13

60.2

120°

3x M4
10mm tief

Isometrische Ansicht
Maßstab: 1:2

Pos.

Menge

Ein-
heit

And.

Sachnummer

Benennung/Merkmale

Ohne sep.Stückliste
Sep.Stückliste

Physik Institut Universität Zürich
Winterthurerstrasse 190 8057 Zürich
Tel. 01 635 57 11 Fax 01 635 57 04

And.

Sach-Nr.

Benennung

Gezeichnet

K. Bösiger

E-Mail

boesiger@physik.uzh.ch

Tel. direkt / Fax

044 635 57 33 / 044 635 57 31

Datum

Auftrags-Nr.

Ursprung

Ersatz für

Massstab

Anzahl Blatt

Blatt-Nr.

Filename:

Figure A.5: Technical drawing for the holder of the tantalum rings mounted below the cluster flange to shield the calibration sources in their parking position. Drawing provided by Kurt Bösiger, UZH.
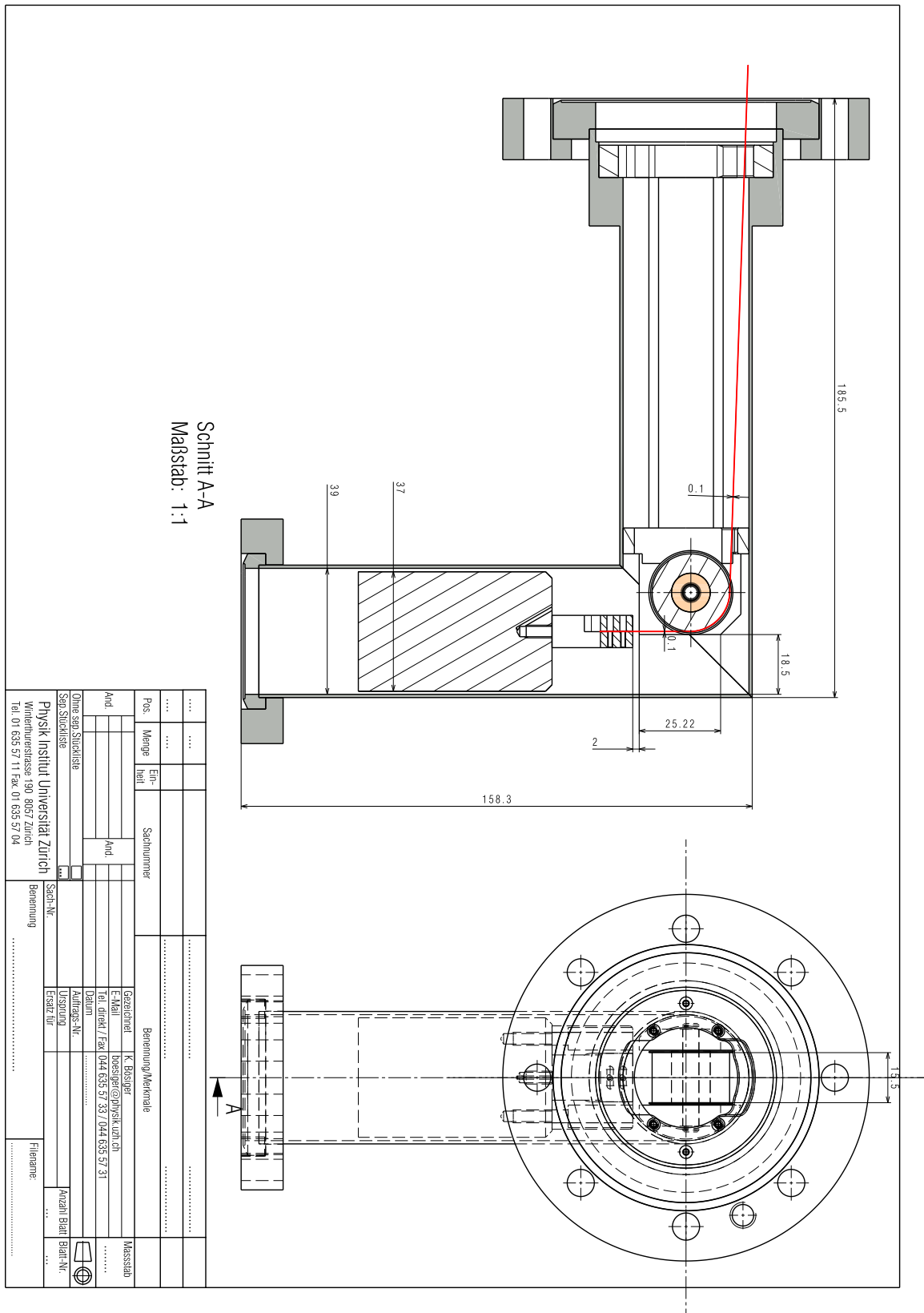
Figure A.6: Technical drawing of the slide-in module designed for the intermediate calibration system. Drawing provided by Kurt Bösiger, UZH.

Figure A.7: Technical Drawing of the holder for the final calibration system. Drawing provided by Kurt Bösiger, UZH.
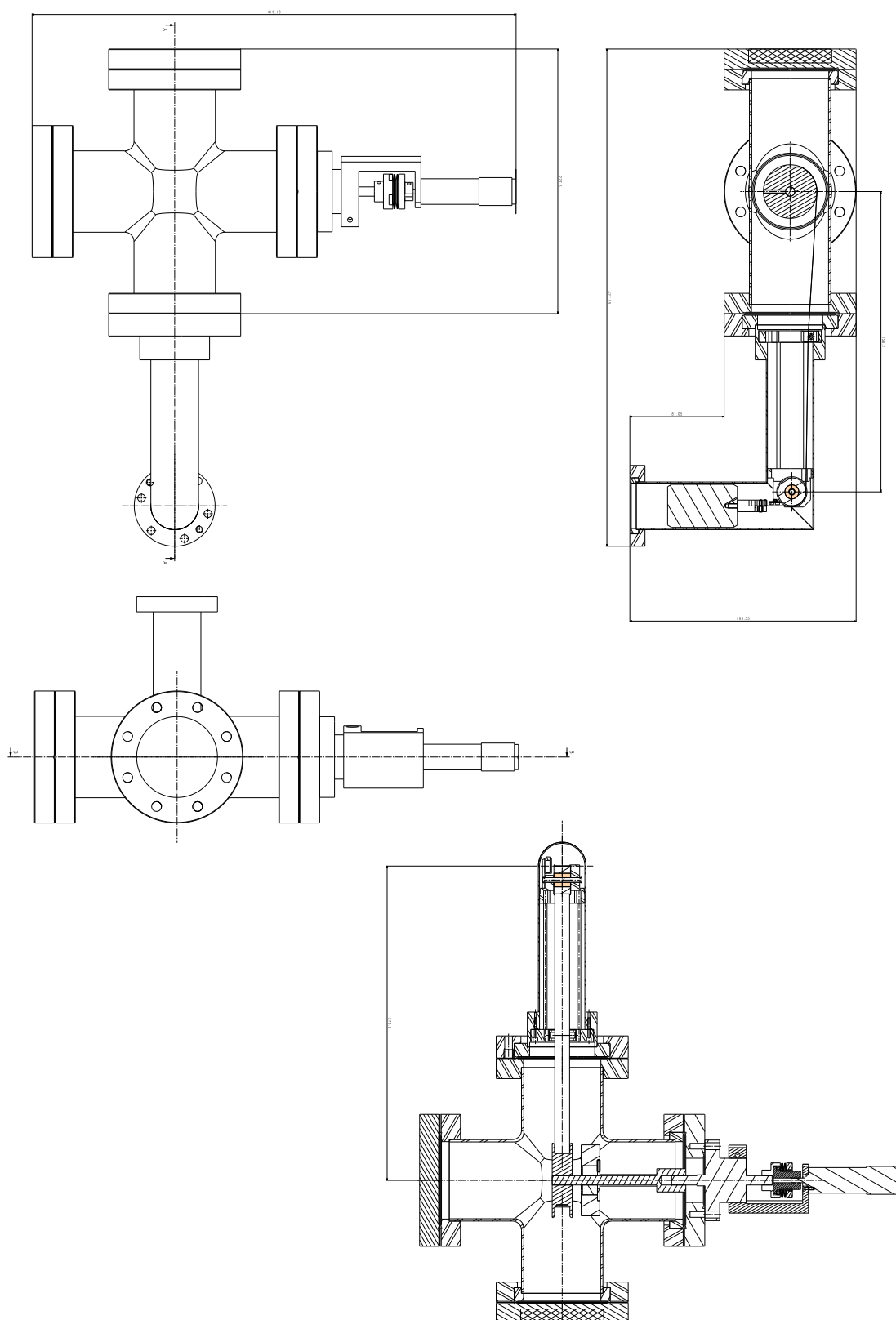
Figure A.8: Technical Drawing of the final calibration system. Drawing provided by Kurt Bösiger, UZH.
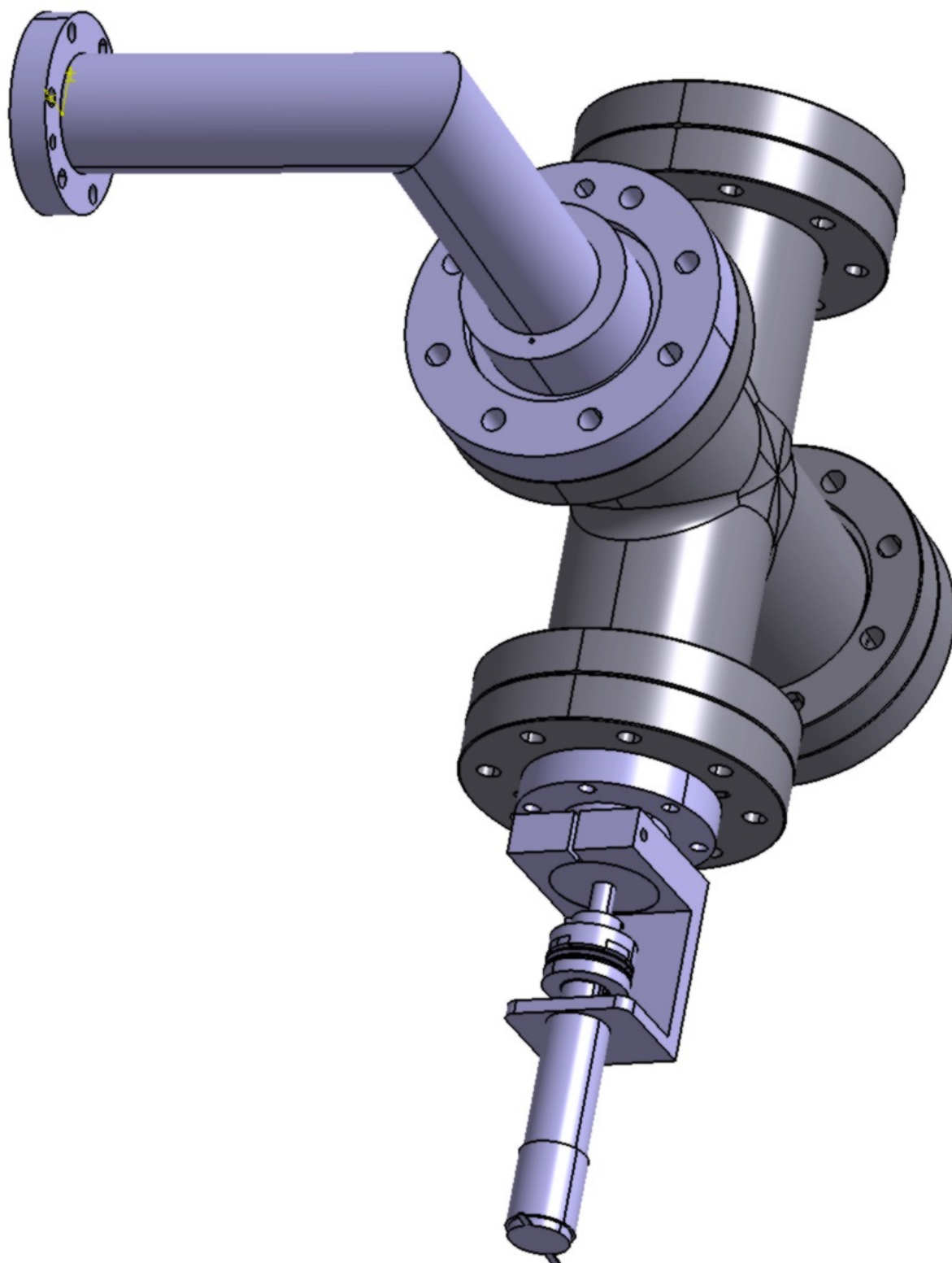
Figure A.9: 3D of the final calibration system. Drawing provided by Kurt Bösiger, UZH.

Data Sheets B

For completeness the data sheets of different parts of the calibration system as provided by the company. The reference number identifying the exact type is given in the caption.

Rotary Feedthroughs with Magnetofluid Sealing

SUPERSEAL Series

Simple rotary feedthrough with bulkhead fitting for wall fastening, with KF or CF flange.

- No internal o-ring seals
- Very low magnetic stray fields
- No magnets inside vacuum
- Rugged stainless steel shafts Ø 6 mm or Ø 8 mm
- Revolution 5000 RPM without load
- Pressure-resistant up to 2.5 bar differential pressure
- Insensitive to external magnetic fields (> 500 Gauss)
- Magnetofluid: synthetic oil or PFPE

Technical Data

- Transmittable torque
  - shaft Ø 6 mm — 5.65 Nm
  - shaft Ø 8 mm — 18 Nm
- Max. revolution (loadfree)
  - synthetic oil — 5000 RPM
  - PFPE — 2500 RPM
- Static friction resistance
  - synthetic oil — 7.8 Ncm
  - PFPE — 14.2 Ncm
- Rotary friction resistance (100 RPM)
  - synthetic oil — 4.3 Ncm
  - PFPE — 15.6 Ncm
- Vacuum area
  - synthetic oil — up to 10^{-8} mbar
  - PFPE — up to 10^{-9} mbar
- Max. operating temperature
  - synthetic oil — 60 °C
  - PFPE — 100 °C
- Vapour pressure magnetofluid
  - synthetic oil — 10^{-10} mbar
  - PFPE — 10^{-12} mbar
- Max. pressure difference — 2.5 bar
- Helium leakage rate — $< 5 \times 10^{-9}$ mbar l / s
- Material
  - housing/shaft — stainless steel 17-4 PH
  - bearing grease — Fomblin / Krytox blend
- Vapour pressure grease lubricant — 10^{-13} mbar
- Max. bearing load (static) — 138 kg
- Vacuum side — arbitrarily

Order code	Vacuum connection	Shaft diameter (mm)	Magnetfluid bearing oil
10C-26100900	DN40CF	8	synthetic oil
10C-26101100	DN25KF	8	synthetic oil
10C-26101400	DN40CF	6	synthetic oil
10C-26101300	DN25KF	6	synthetic oil
10C-26101000	M26	8	synthetic oil
10C-26101200	M26	6	synthetic oil
10C-26100902	DN40CF	8	PFPE
10C-26101102	DN25KF	8	PFPE
10C-26101402	DN40CF	6	PFPE
10C-26101302	DN25KF	6	PFPE
10C-26101002	M26	8	PFPE
10C-26101202	M26	6	PFPE

Figure B.1: Specifications for the rotary feedthrough, order number 10C-26100902

Rotary Feedthrougs with Magnetofluid Sealing

SUPERSEAL Series

10C-26100900 and 10C-26100902
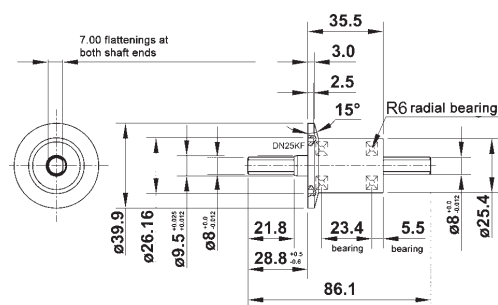
10C-26101100 and 10C-26101102
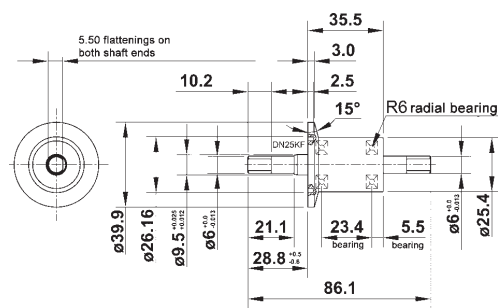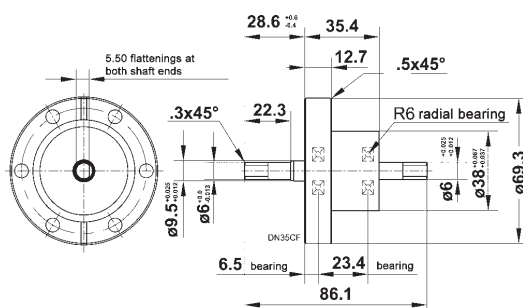
10C-26101400 and 10C-2601402
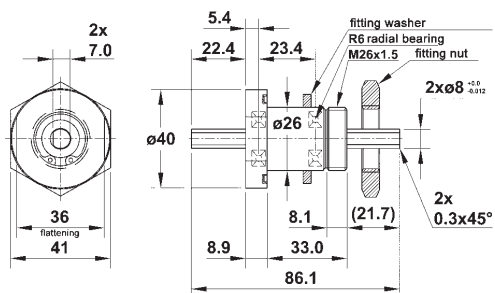
10C-26101300 and 10C-26101302

10C-26101000 and 10C-26101002

10C-26101200 and 10C-26101202

VACOM offers repair service for magnetofluid feedthroughs of all manufacturers.

RE-max 24 ∅24 mm, Graphite Brushes, 11 Watt

M 1:1

█ Stock program
☐ Standard program
▨ Special program (on request)

maxon *RE*-max

Order Number

		222036	222037	222038	222039	222040	222041	222042	222043	222044	222045	222046	222047			

Motor Data
Values at nominal voltage

			222036	222037	222038	222039	222040	222041	222042	222043	222044	222045	222046	222047
1	Nominal voltage	V	9.0	12.0	15.0	18.0	18.0	24.0	24.0	36.0	42.0	48.0	48.0	48.0
2	No load speed	rpm	8190	7540	8290	8870	8000	9310	7540	9120	8600	7410	5250	4730
3	No load current	mA	45.6	31.0	27.7	25.0	22.1	19.8	15.5	12.9	10.3	7.60	5.15	4.59
4	Nominal speed	rpm	6640	5870	6650	7240	6330	7670	5850	7450	6920	5690	3470	2960
5	Nominal torque (max. continuous torque)	mNm	10.8	12.4	12.4	12.3	12.3	12.1	12.2	12.1	12.0	12.0	12.0	12.1
6	Nominal current (max. continuous current)	A	1.08	0.853	0.752	0.666	0.598	0.516	0.421	0.335	0.270	0.204	0.144	0.131
7	Stall torque	mNm	57.7	56.9	63.6	67.7	59.5	69.3	55.3	66.6	62.0	52.4	35.7	32.8
8	Starting current	A	5.55	3.78	3.71	3.52	2.79	2.83	1.83	1.78	1.34	0.855	0.414	0.343
9	Max. efficiency	%	83	83	83	84	83	84	83	84	83	82	79	78

Characteristics

			222036	222037	222038	222039	222040	222041	222042	222043	222044	222045	222046	222047
10	Terminal resistance	Ω	1.62	3.18	4.05	5.11	6.44	8.47	13.1	20.2	31.3	56.2	116	140
11	Terminal inductance	mH	0.0735	0.154	0.200	0.251	0.309	0.406	0.618	0.952	1.45	2.56	5.06	6.22
12	Torque constant	mNm / A	10.4	15.1	17.2	19.2	21.3	24.4	30.1	37.4	46.3	61.3	86.3	95.6
13	Speed constant	rpm / V	919	634	557	497	448	391	317	255	206	156	111	99.8
14	Speed / torque gradient	rpm / mNm	143	134	131	132	135	135	138	138	140	143	149	146
15	Mechanical time constant	ms	5.96	5.90	5.88	5.89	5.91	5.92	5.92	5.93	5.96	5.97	6.03	6.00
16	Rotor inertia	gcm²	3.97	4.22	4.28	4.26	4.17	4.17	4.11	4.11	4.07	4.00	3.88	3.92

Specifications

Thermal data
17 Thermal resistance housing-ambient 24 K / W
18 Thermal resistance winding-housing 5.1 K / W
19 Thermal time constant winding 8.26 s
20 Thermal time constant motor 840 s
21 Ambient temperature -30 ... +85°C
22 Max. permissible winding temperature +125°C

Mechanical data (sleeve bearings)
23 Max. permissible speed 9800 rpm
24 Axial play 0.05 - 0.15 mm
25 Radial play 0.012 mm
26 Max. axial load (dynamic) 1 N
27 Max. force for press fits (static) 80 N
28 Max. radial loading, 5 mm from flange 2.8 N

Mechanical data (ball bearings)
23 Max. permissible speed 9800 rpm
24 Axial play 0.05 - 0.15 mm
25 Radial play 0.025 mm
26 Max. axial load (dynamic) 3.3 N
27 Max. force for press fits (static) 45 N
28 Max. radial loading, 5 mm from flange 12.3 N

Other specifications
29 Number of pole pairs 1
30 Number of commutator segments 9
31 Weight of motor 70 g

Values listed in the table are nominal.
Explanation of the figures on page 49.

Option
Ball bearings in place of sleeve bearings
Pigtails in place of terminals

Operating Range

Comments

█ **Continuous operation**
In observation of above listed thermal resistance (lines 17 and 18) the maximum permissible winding temperature will be reached during continuous operation at 25°C ambient.
= Thermal limit.

☐ **Short term operation**
The motor may be briefly overloaded (recurring).

— **Assigned power rating**

maxon Modular System
Overview on page 16 - 21

Planetary Gearhead
∅22 mm
0.5 - 2.0 Nm
Page 222
Spur Gearhead
∅38 mm
0.1 - 0.6 Nm
Page 236
Spindle Drive
∅22 mm
Page 247 / 248

Recommended Electronics:
LSC 30/2   Page 282
ADS 50/5   282
ADS_E 50/5   283
Notes   18

Figure B.2: Motor specifications, reference number 222043

Planetary Gearhead GP 22 C ∅22 mm, 0.5 - 2.0 Nm

A

+0.2
9.3 0
1.35 -0.45

∅10 +0.003/-0.010
∅4 -0.007/-0.010
3.5 -0.05 0

0 -0.1

∅22

M2.5x4 tief/deep

⊕ ∅0.2 A

14

3x 120°

0
14.85 -1.1

0
3.15 -0.5

L1 max.

M 1:2

Technical Data

Planetary Gearhead	straight teeth
Output shaft	stainless steel, hardened
Bearing at output	ball bearing
Radial play, 10 mm from flange	max. 0.2 mm
Axial play	max. 0.2 mm
Max. radial load, 10 mm from flange	70 N
Max. permissible axial load	100 N
Max. permissible force for press fits	100 N
Sense of rotation, drive to output	=
Recommended input speed	< 8000 rpm
Recommended temperature range	-40 ... +100°C

- ■ Stock program
- □ Standard program
- ▨ Special program (on request)

Order Number

			143971	**143974**	**143980**	143986	143990	**143996**	144002	144004	144011	144017	144023
Gearhead Data													
1	Reduction		3.8 :1	14 : 1	53 : 1	104 : 1	198 : 1	370 : 1	590 : 1	742 : 1	1386 : 1	1996 : 1	3189 : 1
2	Reduction absolute		$15/4$	$225/16$	$3375/64$	$87723/845$	$50625/256$	$10556001/28561$	$59049/100$	$759375/1024$	$158340015/114244$	$285012027/142805$	$1594323/500$
3	Max. motor shaft diameter	mm	4	4	4	3.2	4	3.2	4	4	3.2	3.2	4
	Order Number		**143972**	143975	143981	143987	**143991**	143997	**144003**	144006	144012	144018	144024
1	Reduction		4.4 :1	16 : 1	62 : 1	109 : 1	231 : 1	389 : 1	690 : 1	867 : 1	1460 : 1	2102 : 1	3728 : 1
2	Reduction absolute		$57/13$	$855/52$	$12825/208$	$2187/20$	$192375/832$	$263169/676$	$1121931/1625$	$2885625/3328$	$3947535/2704$	$7105563/3380$	$30292137/8125$
3	Max. motor shaft diameter	mm	3.2	3.2	3.2	3.2	3.2	3.2	3.2	3.2	3.2	3.2	3.2
	Order Number		143973	**143976**	143982	**143988**	143992	143998	144005	**144007**	144013	144019	144025
1	Reduction		5.4 :1	19 : 1	72 : 1	128 : 1	270 : 1	410 : 1	850 : 1	1014 : 1	1538 : 1	2214 : 1	4592 : 1
2	Reduction absolute		$27/5$	$3249/169$	$48735/676$	$41553/325$	$731025/2704$	$6561/16$	$531441/625$	$10965375/10816$	$98415/64$	$177147/80$	$14348907/3125$
3	Max. motor shaft diameter	mm	2.5	3.2	3.2	3.2	3.2	4	2.5	3.2	4	4	2.5
	Order Number			143977	143983	143989	143993	143999		144008	**144014**	144020	
1	Reduction			20 : 1	76 : 1	157 : 1	285 : 1	455 : 1		1068 : 1	1621 : 1	2458 : 1	
2	Reduction absolute			$81/4$	$1215/16$	$19683/125$	$18225/64$	$5000211/10985$		$273375/256$	$601692057/371293$	$135005697/54905$	
3	Max. motor shaft diameter	mm		4	4	2.5	4	3.2		4	3.2	3.2	
	Order Number			143978	**143984**		143994	144000		144009	144015	144021	
1	Reduction			24 : 1	84 : 1		316 : 1	479 : 1		1185 : 1	1707 : 1	2589 : 1	
2	Reduction absolute			$1539/65$	$185193/2197$		$2777895/8788$	$124659/260$		$41668425/35152$	$15000633/8788$	$3365793/1300$	
3	Max. motor shaft diameter	mm		3.2	3.2		3.2	3.2		3.2	3.2	3.2	
	Order Number			143979	143985		143995	144001		144010	144016	**144022**	
1	Reduction			29 : 1	89 : 1		333 : 1	561 : 1		1249 : 1	1798 : 1	3027 : 1	
2	Reduction absolute			$729/25$	$4617/52$		$69255/208$	$2368521/4225$		$1038825/832$	$373977/208$	$63950067/21125$	
3	Max. motor shaft diameter	mm		2.5	3.2		3.2	3.2		3.2	3.2	3.2	
4	Number of stages		1	2	3	3	4	4	4	5	5	5	5
5	Max. continuous torque	Nm	0.5	0.6	1.2	1.2	1.8	1.8	1.8	2.0	2.0	2.0	2.0
6	Intermittently permissible torque at gear output	Nm	0.8	0.9	1.9	1.9	2.7	2.7	2.7	3.0	3.0	3.0	3.0
7	Max. efficiency	%	84	70	59	59	49	49	49	42	42	42	42
8	Weight	g	42	55	68	68	81	81	81	94	94	94	94
9	Average backlash no load	°	1.0	1.2	1.6	1.6	2.0	2.0	2.0	2.0	2.0	2.0	2.0
10	Mass inertia	gcm²	0.5	0.4	0.4	0.4	0.4	0.4	0.4	0.4	0.4	0.4	0.4
11	Gearhead length L1*	mm	25.4	32.2	39.0	39.0	45.8	45.8	45.8	52.6	52.6	52.6	52.6

*L1 is - 2.8 mm for calculating the overall length

overall length   overall length

maxon Modular System

+ Motor	Page	+ Sensor/Brake	Page	Overall length [mm] = Motor length + gearhead length + (sensor / brake) + assembly parts										
A-max 19	93/94			51.6	58.4	65.2	65.2	72.0	72.0	72.0	78.8	78.8	78.8	78.8
A-max 19, 1.5 W	94	MR	258/260	56.7	63.5	70.3	70.3	77.1	77.1	77.1	83.9	83.9	83.9	83.9
A-max 19, 1.5 W	94	Enc 22	265	66.0	72.8	79.6	79.6	86.4	86.4	86.4	93.2	93.2	93.2	93.2
A-max 19, 1.5 W	94	MEnc 13	274	59.1	65.9	72.7	72.7	79.5	79.5	79.5	86.3	86.3	86.3	86.3
A-max 19, 2.5 W	95/96			54.2	61.0	67.8	67.8	74.6	74.6	74.6	81.4	81.4	81.4	81.4
A-max 19, 2.5 W	96	MR	258/260	58.5	65.3	72.1	72.1	78.9	78.9	78.9	85.7	85.7	85.7	85.7
A-max 19, 2.5 W	96	Enc 22	265	68.6	75.4	82.2	82.2	89.0	89.0	89.0	95.8	95.8	95.8	95.8
A-max 19, 2.5 W	96	MEnc 13	274	61.7	68.5	75.3	75.3	82.1	82.1	82.1	88.9	88.9	88.9	88.9
A-max 22	97-100			54.6	61.4	68.2	68.2	75.0	75.0	75.0	81.8	81.8	81.8	81.8
A-max 22	98/100	MR	258/260	59.6	66.4	73.2	73.2	80.0	80.0	80.0	86.8	86.8	86.8	86.8
A-max 22	98/100	Enc 22	265	69.0	75.8	82.6	82.6	89.4	89.4	89.4	96.2	96.2	96.2	96.2
A-max 22	98/100	MEnc 13	274	61.7	68.5	75.3	75.3	82.1	82.1	82.1	88.9	88.9	88.9	88.9
RE-max 21	123/124			51.6	58.4	65.2	65.2	72.0	72.0	72.0	78.8	78.8	78.8	78.8
RE-max 21, 3.5 W	124	MR	258/261	56.7	63.5	70.3	70.3	77.1	77.1	77.1	83.9	83.9	83.9	83.9
RE-max 21	125/126			54.2	61.0	67.8	67.8	74.6	74.6	74.6	81.4	81.4	81.4	81.4
RE-max 21, 6 W	126	MR	258/261	58.5	65.3	72.1	72.1	78.9	78.9	78.9	85.7	85.7	85.7	85.7
RE-max 24	127-130			54.6	61.4	68.2	68.2	75.0	75.0	75.0	81.8	81.8	81.8	81.8
RE-max 24	128/130	MR	259/261	59.6	66.4	73.2	73.2	80.0	80.0	80.0	86.8	86.8	86.8	86.8

Figure B.3: Gear head specifications, reference number 144014

Bibliography

[1]   S. Bilenky, "Neutrinoless double beta-decay," *Phys.Part.Nucl.*, vol. 41, pp. 690–715, 2010.

[2]   S. King, "Neutrino mass," *Contemp.Phys.*, 2007.

[3]   C. Aalseth, H. Back, L. J. Dauwe, D. Dean, G. Drexlin, *et al.*, "Neutrinoless double beta decay and direct searches for neutrino mass," 2004. Part of the APS Neutrino Study.

[4]   F. T. Avignone III, S. R. Elliott, and J. Engel, "Double Beta Decay, Majorana Neutrinos, and Neutrino Mass," *Rev.Mod.Phys.*, vol. 80, pp. 481–516, 2008.

[5]   O. Cremonesi, "Neutrino masses and Neutrinoless Double Beta Decay: Status and expectations," *ArXiv e-prints*, Feb. 2010.

[6]   W. Heisenberg and W. Pauli, "ON QUANTUM FIELD THEORY. 2. (IN GERMAN)," *Z.Phys.*, vol. 59, pp. 168–190, 1930.

[7]   C. Cowan, F. Reines, F. Harrison, H. Kruse, and A. McGuire, "Detection of the free neutrino: A Confirmation," *Science*, vol. 124, pp. 103–104, 1956.

[8]   "Precision electroweak measurements on the Z resonance," *Phys. Rept.*, vol. 427, pp. 257–454, 2006.

[9]   M. Goldhaber, L. Grodzins, and A. W. Sunyar, "Helicity of neutrinos," *Phys. Rev.*, vol. 109, pp. 1015–1017, Feb 1958.

[10] B. Pontecorvo, "Mesonium and anti-mesonium," *Sov.Phys.JETP*, vol. 6, p. 429, 1957.

[11] B. Pontecorvo, "Neutrino Experiments and the Problem of Conservation of Leptonic Charge," *Sov.Phys.JETP*, vol. 26, pp. 984–988, 1968.

[12] Z. Maki, M. Nakagawa, and S. Sakata, "Remarks on the unified model of elementary particles," *Prog.Theor.Phys.*, vol. 28, pp. 870–880, 1962.

[13] S. Abe *et al.*, "Precision Measurement of Neutrino Oscillation Parameters with KamLAND," *Phys.Rev.Lett.*, vol. 100, p. 221803, 2008.

[14] Y. Ashie *et al.*, "A Measurement of atmospheric neutrino oscillation parameters by SUPER-KAMIOKANDE I," *Phys.Rev.*, vol. D71, p. 112005, 2005.

[15] M. Ahn *et al.*, "Measurement of Neutrino Oscillation by the K2K Experiment," *Phys.Rev.*, vol. D74, p. 072003, 2006.

[16] P. Adamson *et al.*, "Measurement of Neutrino Oscillations with the MINOS Detectors in the NuMI Beam," *Phys.Rev.Lett.*, vol. 101, p. 131802, 2008.

[17] K. Abe *et al.*, "Indication of Electron Neutrino Appearance from an Accelerator-produced Off-axis Muon Neutrino Beam," *Phys.Rev.Lett.*, vol. 107, p. 041801, 2011.

[18] P. Adamson *et al.*, "Improved search for muon-neutrino to electron-neutrino oscillations in MINOS," *Phys.Rev.Lett.*, vol. 107, p. 181802, 2011.

[19] Y. Abe *et al.*, "Indication for the disappearance of reactor electron antineutrinos in the Double Chooz experiment," 2011.

[20] P. Machado, H. Minakata, H. Nunokawa, and R. Funchal, "Combining Accelerator and Reactor Measurements of θ_{13}: The First Result," 2011.

[21] U. Seljak, A. Slosar, and P. McDonald, "Cosmological parameters from combining the Lyman-alpha forest with CMB, galaxy clustering and SN constraints," *JCAP*, vol. 0610, p. 014, 2006.

[22] E. Majorana, "Theory of the Symmetry of Electrons and Positrons," *Nuovo Cim.*, vol. 14, pp. 171–184, 1937.

[23] P. Minkowski, "mu -> e gamma at a Rate of One Out of 1-Billion Muon Decays?," *Phys.Lett.*, vol. B67, p. 421, 1977.

[24] T. Yanagida, "HORIZONTAL SYMMETRY AND MASSES OF NEUTRINOS," *Conf.Proc.*, vol. C7902131, p. 95, 1979.

[25] M. Gell-Mann, P. Ramond, and R. Slansky, "Complex Spinors and Unified Theories," in *Supergravity* (P. van Nieuwenhuizen and D. Freedman, eds.), (North Holland, Amsterdam), 1979.

[26] S. L. Glashow, "The future of elementary particle physics," in *Cargese Summer Institute on Quarks and Leptons in 1979* (M. Levy, ed.), (New York), 1980.

[27] R. N. Mohapatra and G. Senjanovic, "Neutrino Mass and Spontaneous Parity Violation," *Phys.Rev.Lett.*, vol. 44, p. 912, 1980.

[28] R. N. Mohapatra *et al.*, "Theory of neutrinos: a white paper," *Pep. Prog. Phys.*, vol. 70, pp. 1757–1867, 2007.

[29] W.-M. Yao *et al.*, "Review of Particle Physics," *Journal of Physics G*, vol. 33, pp. 1+, 2006.

[30] E. Otten and C. Weinheimer, "Neutrino mass limit from tritium beta decay," *Rept.Prog.Phys.*, vol. 71, p. 086201, 2008.

[31] C. Kraus, B. Bornschein, L. Bornschein, J. Bonn, B. Flatt, *et al.*, "Final results from phase II of the Mainz neutrino mass search in tritium beta decay," *Eur.Phys.J.*, vol. C40, pp. 447–468, 2005.

[32] V. Lobashev, V. Aseev, A. Belesev, A. Berlev, E. Geraskin, *et al.*, "Direct search for mass of neutrino and anomaly in the tritium beta spectrum," *Phys.Lett.*, vol. B460, pp. 227–235, 1999.

[33] J. Angrik *et al.*, "KATRIN design report 2004," 2005.

[34] T. Thummler, "Direct neutrino mass measurements," *Phys.Part.Nucl.*, vol. 42, pp. 590–597, 2011.

[35] M. Goeppert-Mayer, "Double beta-disintegration," *Phys.Rev.*, vol. 48, pp. 512–516, 1935.

[36] W. Furry, "On transition probabilities in double beta-disintegration," *Phys.Rev.*, vol. 56, pp. 1184–1193, 1939.

[37] J. Schechter and J. Valle, "Neutrinoless Double beta Decay in SU(2) x U(1) Theories," *Phys.Rev.*, vol. D25, p. 2951, 1982.

[38] M. Doi, T. Kotani, and E. Takasugi, "Double beta Decay and Majorana Neutrino," *Prog.Theor.Phys.Suppl.*, vol. 83, p. 1, 1985.

[39] P. Vogel, "Nuclear physics aspects of double beta decay," 2008.

[40] J. A. Halbleib and R. A. Sorensen, "Gamow-Teller beta decay in heavy spherical nuclei and the unlike particle-hole RPA," *Nuclear Physics A*, vol. 98, pp. 542–568, June 1967.

[41] E. Caurier, G. Martinez-Pinedo, F. Nowacki, A. Poves, and A. Zuker, "The Shell model as unified view of nuclear structure," *Rev.Mod.Phys.*, vol. 77, pp. 427–488, 2005.

[42] J. Menendez, A. Poves, E. Caurier, and F. Nowacki, "Disassembling the Nuclear Matrix Elements of the Neutrinoless beta beta Decay," *Nucl.Phys.*, vol. A818, pp. 139–151, 2009.

[43] J. Barea and F. Iachello, "Neutrinoless double-beta decay in the microscopic interacting boson model," *Phys.Rev.*, vol. C79, p. 044301, 2009.

[44] T. R. Rodriguez and G. Martinez-Pinedo, "Energy density functional study of nuclear matrix elements for neutrinoless $\beta\beta$ decay," *Phys.Rev.Lett.*, vol. 105, p. 252503, 2010.

[45] T. R. Rodriguez and G. Martinez-Pinedo, "Neutrinoless double beta decay studied with configuration mixing methods," *Prog.Part.Nucl.Phys.*, vol. 66, pp. 436–440, 2011.

[46] J. Gomez-Cadenas, J. Martin-Albo, M. Mezzetto, F. Monrabal, and M. Sorel, "The Search for neutrinoless double beta decay," *Riv.Nuovo Cim.*, 2011.

[47] J. Menendez, A. Poves, E. Caurier, and F. Nowacki, "The Occupancies of individual orbits and the nuclear matrix element of the Ge-76 neutrinoless beta beta decay," *Phys.Rev.*, vol. C80, p. 048501, 2009.

[48] J. Suhonen and O. Civitarese, "Effects of orbital occupancies and spin-orbit partners on 0 nu beta beta-decay rates," *Nucl.Phys.*, vol. A847, pp. 207–232, 2010.

[49] F. Simkovic, A. Faessler, H. Muther, V. Rodin, and M. Stauf, "The 0 nu bb-decay nuclear matrix elements with self-consistent short-range correlations," *Phys.Rev.*, vol. C79, p. 055501, 2009.

[50] F. Simkovic, A. Faessler, and P. Vogel, "0 nu beta beta nuclear matrix elements and the occupancy of individual orbits," *Phys.Rev.*, vol. C79, p. 015502, 2009.

[51] D.-L. Fang, A. Faessler, V. Rodin, and F. Simkovic, "Neutrinoless double-beta decay of ^{150}Nd accounting for deformation," *Phys.Rev.*, vol. C82, p. 051301, 2010.

[52] Oleg Chkvorets, *Search for Double Beta Decay with HPGe Detectors at the Gran Sasso Underground Laboratory*. PhD thesis, Ruperto-Carola University of Heidelberg, 2008.

[53] F. Avignone, G. King, and Y. Zdesenko, "Next generation double-beta decay experiments: Metrics for their evaluation," *New J.Phys.*, vol. 7, p. 6, 2005.

[54] H. V. Klapdor-Kleingrothaus, I. V. Krivosheina, A. Dietz, and O. Chkvorets, "Search for neutrinoless double beta decay with enriched Ge-76 in Gran Sasso 1990-2003," *Phys. Lett.*, vol. B586, pp. 198–212, 2004.

[55] A. Caldwell and K. Kröninger, "Signal discovery in sparse spectra: A bayesian analysis," *Phys. Rev. D*, vol. 74, p. 092003, Nov 2006.

[56] M. Inghram and J. Reynolds, "Double beta-decay of Te-130," *Phys.Rev.*, vol. 78, pp. 822–823, 1950.

[57] H. Klapdor-Kleingrothaus, A. Dietz, H. Harney, and I. Krivosheina, "Evidence for neutrinoless double beta decay," *Mod.Phys.Lett.*, vol. A16, pp. 2409–2420, 2001.

[58] H. Klapdor-Kleingrothaus and I. Krivosheina, "The evidence for the observation of 0nu beta beta decay: The identification of 0nu beta beta events from the full spectra," *Mod.Phys.Lett.*, vol. A21, pp. 1547–1566, 2006.

[59] G. Douysset, T. Fritioff, C. Carlberg, I. Bergström, and M. Björkhage, "Determination of the ^{76}Ge Double Beta Decay Q Value," *Physical Review Letters*, vol. 86, pp. 4259–4262, May 2001.

[60] C. Aalseth, I. Avignone, F.T., A. Barabash, F. Boehm, R. Brodzinski, *et al.*, "Comment on 'Evidence for neutrinoless double beta decay'," *Mod.Phys.Lett.*, vol. A17, pp. 1475–1478, 2002.

[61] S. Umehara, T. Kishimoto, I. Ogawa, R. Hazama, H. Miyawaki, *et al.*, "Neutrinoless double-beta decay of Ca-48 studied by Ca F(2)(Eu) scintillators," *Phys.Rev.*, vol. C78, p. 058501, 2008.

[62] H. Klapdor-Kleingrothaus, A. Dietz, L. Baudis, G. Heusser, I. Krivosheina, *et al.*, "Latest results from the Heidelberg-Moscow double beta decay experiment," *Eur.Phys.J.*, vol. A12, pp. 147–154, 2001.

[63] Mathieu Bongrand for the NEMO-3 Collaboration, "Results of the NEMO-3 Double Beta Decay Experiment," 2011.

[64] E. Andreotti, C. Arnaboldi, F. Avignone, M. Balata, I. Bandac, *et al.*, "130Te Neutrinoless Double-Beta Decay with CUORICINO," *Astropart.Phys.*, vol. 34, pp. 822–831, 2011.

[65] J. Gavriljuk, V. Kuzminov, N. Osetrova, and S. Ratkevich, "Results of a search for the two neutrino double beta decay of Xe-136 with proportional counters," *Phys.Rev.*, vol. C61, p. 035501, 2000.

[66] R. Bernabei, P. Belli, F. Cappella, R. Cerulli, F. Montecchia, *et al.*, "Investigation of beta beta decay modes in Xe-134 and Xe-136," *Phys.Lett.*, vol. B546, pp. 23–28, 2002.

[67] J. Argyriades *et al.*, "Measurement of the Double Beta Decay Half-life of Nd-150 and Search for Neutrinoless Decay Modes with the NEMO-3 Detector," *Phys.Rev.*, vol. C80, p. 032501, 2009.

[68] A. Barabash, "Double Beta Decay: Historical Review of 75 Years of Research," *Phys.Atom.Nucl.*, vol. 74, pp. 603–613, 2011.

[69] G. F. Knoll, *Radiation Detection and Measurement*. Wiley, 3rd ed., 2000.

[70] W. R. Leo, *Techniques for Nuclear and Particle Physics Experiments*. Springer Verlag, 2007.

[71] H. Bethe, "Zur Theorie des Durchgangs schneller Korpuskularstrahlen durch Materie," *Annalen der Physik*, vol. 397, no. 3, pp. 325–400, 1930.

[72] R. D. Evans, *The Atomic Nucleus*. New York: Krieger, 1982.

[73] O. Klein and T. Nishina, "Über die Streuung von Strahlung durch freie Elektronen nach der neuen relativistischen Quantendynamik von Dirac," *Zeitschrift fur Physik*, vol. 52, pp. 853–868, Nov. 1929.

[74] M. J. Berger *et al.*, "XCOM: Photon Cross Sections Database," *NIST Standard Reference Database 8 (XGAM)*, Nov. 2010.

[75] G. Ottaviani, C. Canali, and A. A. Quaranta, "Charge carrier transport properties of semiconductor materials suitable for nuclear radiation detectors," *Nuclear Science, IEEE Transactions on*, vol. 22, pp. 192 –204, feb. 1975.

[76] BEGe detectors by Canberra, "http://www.canberra.com/products/485.asp."

[77] D. Budjas, M. Barnabe Heider, O. Chkvorets, N. Khanbekov, and S. Schonert, "Pulse shape discrimination studies with a Broad-Energy Germanium detector for signal identification and background suppression in the GERDA double beta decay experiment," *JINST*, vol. 4, p. P10007, 2009.

[78] Matteo Agostini, "Characterization of a Broad Energy Germanium detector through advanced pulse shape analysis techniques for the GERDA double-beta decay experiment," 2009.

[79] W. Shockley, "Currents to conductors induced by a moving point charge," *Journal of Applied Physics*, vol. 9, no. 10, pp. 635–636, 1938.

[80] S. Ramo, "Currents Induced by Electron Motion ," *Proceedings of the IRE*, vol. 27, pp. 584 − 585, Sept. 1939.

[81] Z. He, "Review of the shockleyâĂŞramo theorem and its application in semiconductor gamma-ray detectors," *Nuclear Instruments and Methods in Physics Research Section A AcceleratorsSpectrometersDetectors and Associated Equipment*, vol. 463, no. 1-2, pp. 250–267, 2001.

[82] L. Gadeken and B. Robertson, "The influence of ge(li) detector pulse shape variations on constant fraction and snap-off timing discriminators," *Nuclear Instruments and Methods*, vol. 136, no. 2, pp. 255 − 259, 1976.

[83] I. Abt and others (GERDA Collaboration), "A New Ge-76 double beta decay experiment at LNGS: Letter of intent," 2004.

[84] A. Bettini, "The World underground scientific facilities: A Compendium," 2007.

[85] M. di Marco, P. Peiffer, and S. Schönert, "LArGe: Background suppression using liquid argon (LAr) scintillation for $0\nu\beta\beta$ decay search with enriched germanium (Ge) detectors," *Nuclear Physics B Proceedings Supplements*, vol. 172, pp. 45–48, Oct. 2007.

[86] I. G. Irastorza and others (IGEX Collaboration), "IGEX 76Ge neutrinoless double-beta decay experiment: Prospects for next generation experiments," *Phys.Rev. D*, vol. 65, pp. 092007–+, May 2002.

[87] H. V. Klapdor-Kleingrothaus, L. Baudis, A. Dietz, G. Heusser, I. Krivosheina, B. Majorovits, and H. Strecker, "GENIUS-TF: a test facility for the GENIUS project," *Nuclear Instruments and Methods in Physics Research A*, vol. 481, pp. 149–159, Apr. 2002.

[88] A. Smolnikov and P. Grabmayr, "Conversion of experimental half-life to effective electron neutrino mass in $0\nu\beta\beta$ decay," *Physical Review C*, vol. 81, p. 028502, Feb. 2010.

[89] M. Barnabé Heider, D. Budjáš, K. Gusev, and S. Schönert, "Operation and performance of a bare broad-energy germanium detector in liquid argon," *Journal of Instrumentation*, vol. 5, p. 10007, Oct. 2010.

[90] F. Froborg on behalf of the GERDA Collaboration, "The GERDA Experiment - A Search for Neutrinoless Double Beta Decay," *Talk at TeV PA*, 2011.

[91] Y.-D. Chan, J. A. Detwiler, R. Henning, V. M. Gehman, R. A. Johnson, D. V. Jordan, K. Kazkaz, M. Knapp, K. Kroninger, D. Lenz, J. Liu, X. Liu, M. G. Marino, A. Mokhtarani, L. Pandola, A. G. Schubert, and C. Tomei, "MaGe - a Geant4-based Monte Carlo framework for low-background experiments," *ArXiv e-prints*, vol. 802, Feb. 2008.

[92] Geant4 Collaboration, "Geant4 - a simulation toolkit," *Nuclear Instruments and Methods in Physics Research*, vol. 506, pp. 250–303, July 2003.

[93] Marik Barnabé Heider, *Performance and stability tests of bare high purity germanium detectors in liquid argon for the GERDA experiment*. PhD thesis, Ruperto-Carola University of Heidelberg, 2009.

[94] MPI für Kernphysik Heidelberg, "Data taken during commissioning phase." Private Communication, 2009.

[95] W. B. Wilson *et al.*, "Sources4A. Technical Report, LA-13639-MS," 1999.

[96] Michal Tarka, *Studies of Neutron Flux Suppression from a γ-ray Source and the GERDA Calibration System*. PhD thesis, University of Zurich, 2012.

[97] L. Baudis *et al.*, "A Low Neutron Emission ^{228}Th Source for the Calibration of the GERDA Experiment," in preparation.

[98] W. S. Lyon and J. S. Eldridge, "Radioactive ge^{77} and ge^{77m}," *Physical Review*, vol. 107, pp. 1056–1057, Aug. 1957.

[99] E. der Mateosian and M. Goldhaber, "Thermal-neutron activation cross sections of ge and the isomeric ratio rule," *Phys. Rev.*, vol. 108, pp. 766–768, Nov 1957.

[100] G. Meierhofer, P. Kudejova, L. Canella, P. Grabmayr, J. Jochum, and J. Jolie, "Thermal neutron capture cross-section of ^{76}Ge," *European Physical Journal A*, vol. 40, pp. 61–64, Apr. 2009.

[101] Plansee Composite Materials GmbH, "http://www.plansee.com/tungsten-densimet.htm."

[102] L. Baudis, A. D. Ferella, A. Askin, J. Angle, E. Aprile, *et al.*, "Gator: a low-background counting facility at the Gran Sasso Underground Laboratory," *ArXiv e-prints*, Mar. 2011.

[103] Meterdrive by Vectral SARL, "http://www.vectral.fr/meterdrive/index-en.html."

[104] E. Marquardt, J. Le, and R. Radebaugh, "Cryogenic Material Properties Database," *11th International Cryocooler Conference*, 2000.

[105] National Institute for Standards and Technology, Cryogenic Technology Group, "http://cryogenics.nist.gov/MPropsMAY/material%20properties.htm."

[106] V. T. Jordanov and G. F. Knoll, "Digital synthesis of pulse shapes in real time for high resolution radiation spectroscopy," *Nuclear Instruments and Methods in Physics Research A*, vol. 345, pp. 337–345, June 1994.

[107] F. Goulding, D. Landis, N. Madden, M. Maier, and H. Yaver, "Gammasphere-elimination of ballistic deficit by using a quasi-trapezoidal pulse shaper," *Nuclear Science, IEEE Transactions on*, vol. 41, pp. 1140 –1144, aug 1994.

[108] M. Agostini, L. Pandola, P. Zavarise, and O. Volynets, "Gelatio: a general framework for modular digital analysis of high-purity ge detector signals," *Journal of Instrumentation*, vol. 6, no. 08, p. P08013, 2011.

[109] R. Brun and F. Rademakers, "ROOT: An object oriented data analysis framework," *Nucl.Instrum.Meth.*, vol. A389, pp. 81–86, 1997.

[110] J. Stein, F. Scheuer, W. Gast, and A. Georgiev, "X-ray detectors with digitized preamplifiers," *Nuclear Instruments and Methods in Physics Research Section B*, vol. 113, no. 1 - 4, pp. 141 – 145, 1996.

[111] M. Agostini, D. Budjas, L. Pandola, and P. Zavarise, "GERDA off-line analysis of HPGe detector signals," *GERDA internal note*, vol. 012, 2011.